Progress in engineering interlayer space modulated MXenes to architect next-generation airborne pollutant sensors

Vishal Chaudhary [a,b,*], Hafiz Taimoor Ahmed Awan [c], Mohammad Khalid [c,d,**], Pradeep Bhadola [e,***], Rampal Tandon [f], Ajit Khosla [g,***]

[a] *Research Cell and Department of Physics, Bhagini Nivedita College, University of Delhi, New Delhi 110043, India*
[b] *SUMAN Laboratory (SUstainable Materials and Advanced Nanotechnology Lab), University of Delhi, New Delhi 110072, India*
[c] *Graphene and Advanced 2D Materials Research Group (GAMRG), School of Engineering and Technology, Sunway University, No. 5, Jalan University, Bandar Sunway, Petaling Jaya, Selangor 47500, Malaysia*
[d] *Sunway Materials Smart Science and Engineering (SMS2E) Research Cluster, Sunway University, No. 5, Jalan Universiti, Bandar Sunway, Petaling Jaya, Selangor 47500, Malaysia*
[e] *Centre for Theoretical Physics and Natural Philosophy, Nakhonsawan Studiorum for Advanced Studies, Mahidol University, Nakhonsawan 60130, Thailand*
[f] *Department of Physics and Astrophysics, University of Delhi, Delhi 110007, India*
[g] *Department of Applied Chemistry, School of Advanced Materials and Nanotechnology, Xidian University, Xi'an 710126, PR China*

ABSTRACT

The globally expanding requirements of a growing population have led to extensive urbanization and industrialization, continually leading to air eminence degradation. It has raised the urgent demand to architect efficient airborne pollutant sensors. The state-of-the-art gas/vapour sensor is concerned with exploring advanced nanomaterials to attain commercial viabilities. Owing to the high specific surface area, optimum porosity, tunable physicochemical attributes, abundant surface functionalities and solution processability, 2D metal carbides/nitrides/carbonitrides (MXenes) are the most intriguing class of nanomaterials for devising high-performance airborne pollutant sensors. However, its commercial prospects are limited due to layer restacking, and oxidation in a humid and oxygen-rich environment. These issues have been catered to by modulating the interlayer spacing in MXenes through intercalation, delamination, surface engineering, heteroatom doping and hybridization. It also optimizes the physicochemical attributes of MXenes for targeted airborne analyte detection due to induced synergistic effects. This review comprehensively summarizes the current strategies to regulate the interlayer spacing in MXenes to design selective and high-performance gas/vapor chemiresistive-type sensors. Additionally, it highlights the challenges, possible solutions and cutting-edge prospects to architect intelligent and sustainable airborne pollutant sensors with the integration of modern-day technologies, including internet-of-things, 5 G communication, cloud computing and artificial intelligence.

1. Emergence of MXenes to architect gas and vapor sensors

The rapid deterioration in air eminence due to extensive urbanization, industrialization and technological advancements is the primary global concern requiring urgent solutions. The uncontrolled release of airborne contaminants into the environment due to numerous anthropogenic activities comprising industrial, vehicular, agricultural, constructional and household emissions has led to serious ecological threats, including global warming, air pollution, ozone depletion, acid rain, eutrophication, climate shift and low visibility. These airborne contaminants are emitted in solid phase (particulate matter: PM), vapor phase (volatile organic compounds: VOCs), and gaseous phase (oxides of carbon, sulphur, nitrogen, and ammonia), causing hazards to environment as well as to humans [1–5]. The inhalation of these contaminants
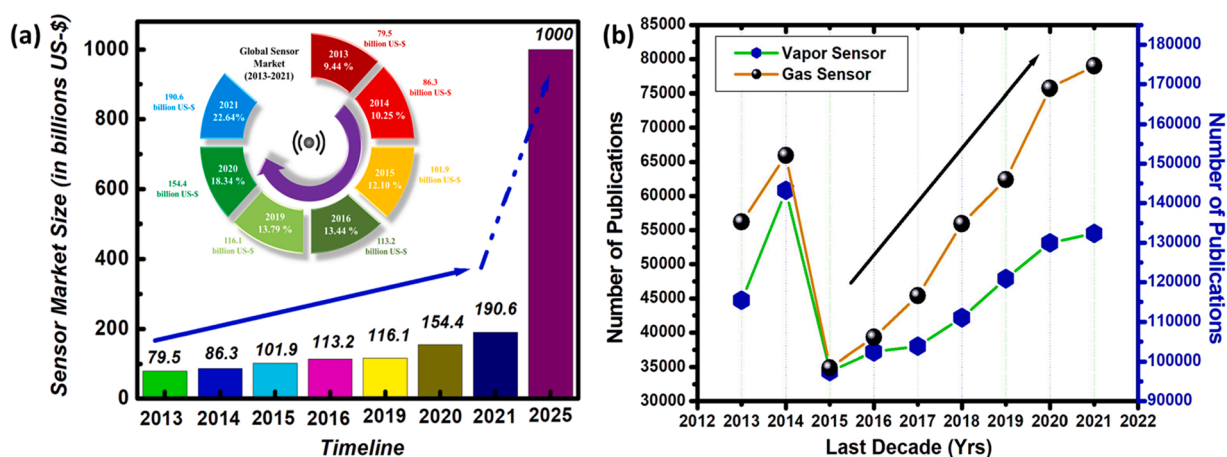

Fig. 1. (a) Global Sensor Market in the last decade with expected projection till 2025 [4], and (b) Research and development dedicated to gas/vapor sensors in last decade (Searched on Dimension app with key words: gas sensor and vapor sensor).
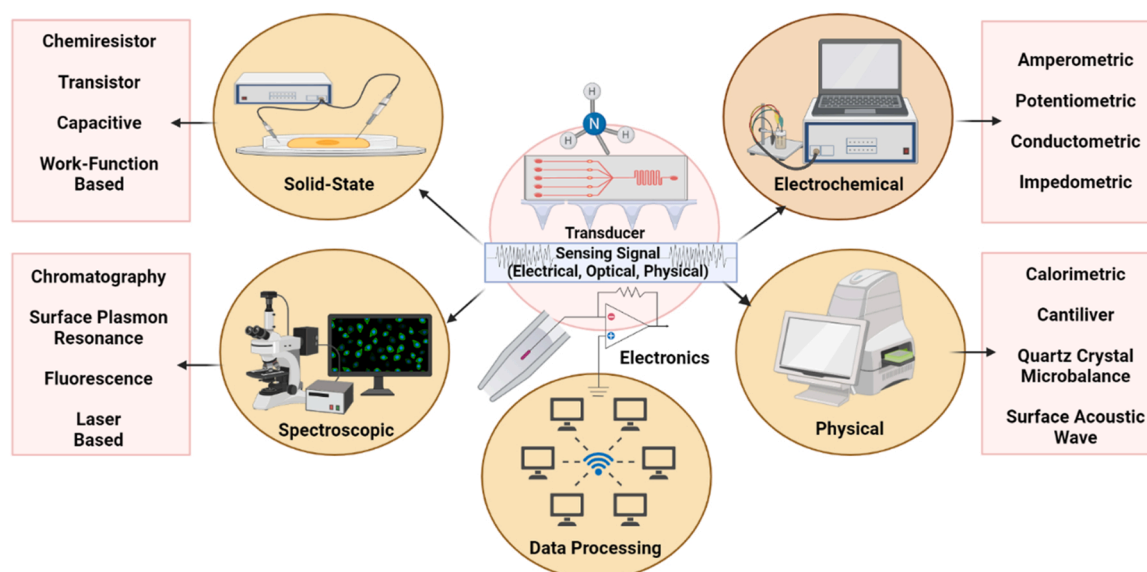

Fig. 2. State-of-the-art gas/vapor sensors with different modules depending upon transducing signals and various low-dimensional materials as sensing layer.

by humans beyond the lowest exposure limits defined for every air contaminant affects their respiratory, nervous, immune and cardiovascular systems, making humans more vulnerable to critical-risk infectious diseases such as coronavirus disease (COVID-19) [2,3,6–8]. According to World Health Organization (WHO), 20% of stroke-related and cardiovascular mortalities are due to air contamination, along with the estimation of 3.8 million people suffering annually from airborne fatal diseases [9]. Recently, Chaudhary et al. [3] reported that PM, NH_3 and sulphur dioxide (SO_2) acts as secondary carrier in the spread of COVID-19 and surges associated mortalities by weakening human immune system. Consequently, it has increased the universal demand for airborne contaminant monitoring strategies, especially gas/vapor sensors.

The demand for sensors and gas is not restricted to air quality and control monitoring, but it also extends to smart agricultural practices, workplace safety, military, food and public safety, and breath-analysis based therapeutic diagnosis [10–19]. For instance, a sensor with the lowest detection limit (LDL) range of 300–1800 parts per billions (ppb) can be implemented for non-invasive diabetes detection and potentially revolutionise the current time-consuming and invasive global diagnostic market [20,21]. This broadened demand for gas/vapor sensors has

increased the size of the global sensor market, which was valued at 190 billion US dollars globally in 2021 and is predicted to reach 1 trillion US dollars by 2025 [22](Fig. 1(a)). Therefore, to meet the enormous market needs, there has been significant research and development done on gas/vapor sensors during the past ten years (Fig. 1(b)).

It has been observed since 2015, the number of research publications dedicated to gas/vapor sensors has increased at an inordinate pace and still growing to fill the market gap and demands. The state-of-the-art gas/vapor sensors are concerned with the integration of modern-age technologies, including nanotechnology, 3D/4D printing, flexible and transparent architecture, self-operating and biocompatible modules, internet-of-things (IOTs), artificial intelligence (AI) and wireless technologies [12,22–24]. The incorporation of nanotechnology enhances the sensing performance (in terms of rapid detection and low trace monitoring), whereas the integration of advanced smart technologies results in their intelligent, remote and portable operation [15,16,25–34]. Moreover, the improvements in sensor architect and transducing sensing signal processing are the focused research areas in development of gas/vapor sensors.

Based on the underlying detecting mechanism and integrated technology, the gas/vapor sensor can be classified into different modules,

including electrochemical, calorimetric, optical, electronic, electrical, gravimetric, chromatographic, acoustic and thermoelectric modules [4, 22,35,36] (Fig. 2). Amongst all, chemiresistive module-based gas/vapor sensors are popular and commercial due to their compact size, cost-effectiveness, portable and flexible features, energy-efficient, and friendly operation with line-of-sight real time and remotely accessible monitoring. The fundamental architect of chemiresistors is simple, consisting of an optimized sensing nanomaterial layer deposited on a substrate with sensing/working electrodes [4,35]. It is further coupled to suitable detecting electronics and integrated circuits designed in accordance with the transduction signal. The sensing performance of gas/vapor sensor is assessed in terms of 3-essential S's (stability, sensitivity and selectivity) and 5-R's (response time, repeatability, room temperature operation, recovery time and range of detection). Moreover, advanced features such as intelligent operation, biocompatibility, flexibility, portability, self-operation, and automation are highly mandatory to achieve future-generation smart modules.

The state-of-the-art gas/vapor chemiresistive-sensors are concerned with engineering high-performance functional nanomaterials, optimizing their physicochemical properties and thickness of sensing layer, architecting electrode designs and substrates, and improvising detecting circuitry for prompt and amplified sensing performance. For instance, various electrode designs, such as interdigitated electrodes, have been proven better for gaseous/vapor detection compared to parallel surface electrodes [37,38].

Despite that, the most energetic research is devoted to engineering low-dimensional functional nanomaterials and tuning their physicochemical attributes for designing high-performance gas/vapor sensors with enhanced fundamental and advanced features [39,40]. It is attributed to sensing being a surface phenomenon in which low-dimensional materials with superior surface-to-volume ratio contribute to larger interaction between sensing material and detecting analyte. Amongst all, metal oxide-based chemiresistive-sensors is the most commercialized class of nanomaterials used to detect and monitor diversified gaseous/vapor analytes [22,41]. Though, certain drawback associated with metal oxide-based sensors, such as requirement of high temperature operation to produce appropriate oxygen adsorbents (O^{2-} and O^-) on to the sensor surface, surges complexity, cost, energy requirement, toxicity and diminishes their lifetime due to merging of grain boundaries in sensing material. Other classes of nanomaterials, including carbon nanomaterials and organic nanomaterials, are capable of room temperature detection of gas/vapor analytes [13,22]. However, they suffer from low selectivity and delayed response/recovery time due to their specific affinity towards various analytes. Therefore, it has raised the quest to explore advanced functional nanomaterials which can cater to these issues and exhibit high-performance sensing and monitoring performances.

In the past few decades, two-dimensional (2D) nanomaterials have emerged as attractive flatlands for a variety of gaseous/vapor detection and monitoring [40,42,43]. These materials include graphene as well as its derivatives, 2D organic frameworks, metal dichalcogenides, borophene, molybdenum disulfide (MoS_2), phosphorene, black phosphorus (BP) and metal carbides/nitrides (MXenes), respectively [4,12,43–45]. At the same time, their superior sensing performances are credited to their higher specific surface area, optimum porosity, tunable surface chemistries, and interlayer distances. Recently, 2D MXenes are one of the novel emergent sensing 2D-nanomaterials exhibiting promising sensing performances in terms of 3-essential S's and 5-R aspects. In addition, various unique physicochemical attributes of MXenes stand them out from other 2D materials, including excellent conductivity, significant biocompatibility, abundant surface functionalities, low toxicity, excellent hydrophilicity, enlarged effective surface area, and significant tribological characteristics for devising gas/vapor chemiresistive-type sensors.

MXene is the newest 2D inorganic material family, which is signified by formula $M_{n+1}X_nT_x$, where '(n + 1)' is the no. of layers encompassing 'M' combined with 'n' no. of layers, including 'X' (with "M" is an early transition material, and "X" mentioning the (carbon, nitrogen or combination of both) and, 'T' signifying several surface functionalities like, (-OH, -F, -O, and -Cl) [4,13,46,47]. They are fabricated by selective elimination method from its precursors, including 'MAX' phases ($M_{n+1}AX_n$; A: 13 or 14 group element), 'non-MAX' phases ($(MC)_n[Al (A)]_mC_{(m-1)}$; m is 3,4, and A is Si or Ge) and 'i-MAX' phases ($(M_1^{2/3}M_2^{1/3})_2AX$) [17,48]. Numerous MXenes with different stoichiometry (Ti_2CT_x, $Ti_3C_2T_x$, Ti_3CNT_x, $Ta_4C_3T_x$, Nb_2CT_x, $(V_{0.5}Cr_{0.5})_3C_2T_x$), V_2CT_x, $(Ti_{0.5}Nb_{0.5})_2CT_x$) have been evaluated for gas/vapor detection and monitoring [4,12]. It has been exhibited that by varying surface functionalities and stoichiometry of MXenes, diversified gaseous/vapor analytes can be detected. Whereas the experimental observation of pure MXene-based gas/vapor detecting chemiresistors, however, divulged that they shared a number of common issues, including low flexibility, layer restacking, low stability in oxygen and humid environments, and slower recovery due to a higher affinity for polar contaminants [4,12, 13]. These challenges can be addressed by engineering the interlayer spacing of MXene layers using different strategies, including intercalation, delamination, surface engineering, heteroatom doping and integration of additive materials in the form of hybrids and composites [4, 13,49–52]. For instance, surface engineering can cater to oxidation issues, intercalation can cater to restacking, and doping can be used to achieve selectivity. Additionally, this interlayer modulation is also utilized to optimize the physicochemical characteristics like electrical and optical band gap, effective surface area, porosity, and tribological attributes of MXenes for devising targeted airborne analyte monitoring and detection systems. Moreover, several studies have reported that despite low toxicity and good biocompatibility, pristine MXenes are toxic to specific cells and embryos [53]. However, surface engineering of MXenes caters to toxicity aspects of pristine MXenes and diminishes it to a minimal level. Besides, the ecological toxicity and contamination of pristine MXenes can be altered using interfacial space engineering strategies such as hybridization and surface modifications resulting in repurpose, reuse and recyclable MXenes [54].

Although MXenes have demonstrated excellent performance in airborne contaminant monitoring, a comprehensive review has not articulated the effect of tuning interlayer distance using different strategies. To the best of our knowledge, the literature does not contain a specific review examining the difficulties in using pristine MXene-based chemiresistors to identify air pollutants. The development of interlayer space-modulated MXenes to create next-generation airborne pollutant sensors has not been fully described, which is most crucial. This paper examines the cutting-edge interlayer space engineering of MXenes for architecting gas/vapor sensors of chemiresistive modules to guide future research in air pollutant detection and monitoring to fill this knowledge gap. Moreover, it highlights the associated challenges, alternate solutions, and cutting-edge prospects of interlayer-engineered MXenes (ILe-MXenes) for air contaminant monitoring. Additionally, it discusses the on-site, remote, field-deployable and intelligent detection/monitoring of airborne contaminants using ILe-MXenes with the integration of modern-age technologies, including AI, cloud computing, IoT, 5 G communications, and 3D/4D printing.

2. Architecting MXenes for engineering interlayer engineered MXenes: limitations of pristine MXenes in air contaminant monitoring

The engineering of interlayer space modulated MXenes (ILe-MXenes) is a multi-step process including numerous strategies [55]. The first stage is comprised of fabricating pristine MXenes through selective etching strategies. In this stage, multilayer stacked MXenes are etched from relevant precursor's phase (MAX, non-MAX, i-MAX, o-MAX) by detaching 'A/A-C′' layers through different harnessing, including top-down or bottom-up routes [12,47,50]. The possibility of removing central layer of 'A/A-C′' was first theoretically prophesied using modern

Table 1

A detailed summary of diversified MXene's harnessing strategies resulting in various surface terminations using a top-down strategy based on selective etching from various precursors [17,46,47,50,58,66,67].
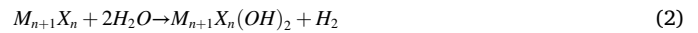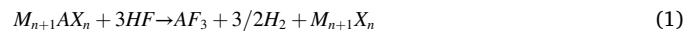
Phases	Precursors	Etched MXene	Ethant Used	Processing Method	Surface Elimination Group
MAX Phases	Ti_2AlC, Ti_3AlC_2, Ti_3AlCN (Nb,Zr)$_4AlC_3$, V_2AlC,	Ti_2CT_x, $Ti_3C_2T_x$, Ti_3CNT_x (Nb,Zr)$_4C_3T_x$, V_2CTx,	$LiF/KF/NaF/$ $FeF_3/$ $NH_4F + HCl$, $NaHF_2$ $/KHF_2$ $/NH_4HF_2$; $LiF/KF/NaF/$ $FeF_3/$ $NH_4F + HCl$; $LiF + HCl$, $NaF + HCl$, $LiF + HCl$ $NH_4F + C_5H_{14}Cl$ $H_2C_2O_4$; Ionic liquid (EMIMBF$_4$/ BMIMPF$_6$),	In situ HF formation etching	-O, -F, -OH -O, -F (ionic liquid)
	Ti_3AlC_2, V_2AlC, Nb_2AlC, Nb_4AlC_3, Ta_4AlC_3, (Ti,Nb)$_2AlC$, Mo_2Ti_2AlC, $Mo_2Ga_2C_2T_x$, $Hf_3(AlSi)_4C_6$, $Zr_3Al_3C_5$ $(Mo_{2/3}Sc_{1/3})_2AlC$	$Ti_3C_2T_x$, V_2CT_x, Nb_2CT_x, $Nb_4C_3T_x$, $Ta_4C_3T_x$, (Ti,Nb)$_2CT_x$, $Mo_2Ti_2C_3T_x$, Mo_2C, $Hf_3C_2T_x$, $Zr_3C_2T_x$ $Mo_{1.33}CT_x$	HF	HF etching	-F,-OH, -O,
	Ti_3SiC_2,Ti_3ZnC_2 Ti_4AlN_3	$Ti_3C_2T_x$ $Ti_4N_3T_x$	$CuCl_2$, $FeCl_2$ /$CoCl_2$ /$NiCl_2$ /$AgCl_2$ /$CdCl_2$ $KF/LiF/NaF$	Molten salt etching	-O, -Cl -O, -F
	Cr_2AlC, Ti_3AlC_2, V_2AlC	Cr_2CT_x, $Ti_3C_2T_x$, V_2CT_x,	NH_4Cl +TMAOH/HCl, HCl, HCl	Electrochemical Etching	-Cl, -OH, -O,
Non MAX Phase	Mo_2Ga_2C	Mo_2C	Ultraviolet light (100 W)	UV	-O
	Zirconium Based (Al contained) $Zr_2Al_3C_4$,$Zr_3Al_3C_5$, $ZrAl_8C_7$, $ZrAl_4C_4$, $Zr_2Al_4C_5$,Zr_3Al_4C	Zr_2C_4, Zr_3C_5, ZrC_7, $ZrC4$. Zr_2C_5, Zr_3C_6	HCl/LiF, HCl/NH$_4$F	HF etching	-O, -F, -OH
	Al (A) contained $Zr2[Al(Si)]4C5$ $Zr3[Al(Si)]4C6$ [ZrY)]2Al4C5 $Zr2[Al(Ge)]4C5$ $Zr3[Al(Ge)]4C6$ $Zr[Al(Si)]8C7$ $Zr[Al(Si)]4C4$	Zr2C5, Zr3C6 [ZrY)]2C5, Zr2C5, Zr3C6 ZrC7, ZrC	HCl/LiF, HCl/NH$_4$F	In-situ HF etching	-F, -O,-OH
	Hafnium Based (Al Contained) $Hf_2Al_4C_5$ Hf_3Al_4C6 $HfAl_4$ Hf_2Al_3C	Hf_2C_5 Hf_3C_6 HfC_4 Hf_2C_4	HCl/LiF, HCl/NH$_4$F	Etching	-OH, -F,-O
i-MAX Phase	$W_{1/3}Mo_{1/3}Gd_{1/3})_2AlC$	$W_{2/3}Mo_{2/3}(Gd)CT_x$	HCl/LiF	Etching	O-/N-

computing techniques based on phonon and electronic structural arrangement estimations. For instance, Khazaei et al. [56] computed exfoliation energies along with force constants required to etch the central layer from 82 MAX precursors. The outcomes of estimations exhibited the possibility of removing central 'A' layers from MAX precursors through exfoliation to fabricate MXene. Experimentally, ILe-MXenes can be fabricated in two stages: exfoliation and interlayer space modulation (delamination, intercalation, doping, surface functionalization and hybridization).

2.1. Preliminary Stage of MXene fabrication from its respective precursors

The initial stage of fabricating ILe-MXenes can be divided into various routes, including physical and chemical methods via top-bottom and bottom-up approaches. The most developed and scalable techniques to fabricate MXenes include chemical based etching in which surface functionalities and stoichiometry can be regulated as per desired physicochemical properties. MXenes are produced due to several etching techniques that remove the centre "A/A-C/Al-A-C" layers from the corresponding precursor [47,50]. These etching methods include electrochemically based non-fluorine etchants, alkaline-based hydrothermal routes, and non-aqueous molten-salt etching methods assisted by Lewis acidic salts. Fluorine-based etchants include HF, in-situ HF: LiF + HCl, bifluoride salts, and fluorine-containing molten salt [50]. For the first time, Naguib et al. [57] demonstrated the synthesis of $Ti_3C_2T_x$-MXene using HF-based selective etching of 'Al' from Ti_3AlC_2 (MAX precursor). During typical synthesis, the precursor powder is soaked in HF solution

for 120 min. It is followed by stirring, centrifugation, filtration, and washing to attain a pH value of 4–6 for synthesizing solution. Moreover, through utilizing molecular dynamics (MD) based ab-initio calculations, they demonstrated the generation of surface functionalities over MAX phase due to interaction with HF, which eventually weakens the Ti-Al bonds leading to the formation of $Ti_3C_2T_X$ MXenes. The chemical reactions involved in the etching of MXene from its MAX precursor using HF are described in Eqs. (1–3) [58]:

$$M_{n+1}AX_n + 3HF \rightarrow AF_3 + 3/2H_2 + M_{n+1}X_n \tag{1}$$

$$M_{n+1}X_n + 2H_2O \rightarrow M_{n+1}X_n(OH)_2 + H_2 \tag{2}$$

$$M_{n+1}X_n + 2HF \rightarrow M_{n+1}X_nF_2 + H_2 \tag{3}$$

It is clear that HF treatment weakens the M-A link, causing the exfoliation of MXenes and the formation of surface terminals as well as the production of AF and H_2 gas. When surface terminals are produced over MXene layers, the entire surface becomes negatively charged, making it thermodynamically more stable than virgin MXenes. Due to its high yield and production of several surface functions, the HF method has been widely used to create various MXenes. However, HF is extremely poisonous, corrosive, and dangerous for both humans and the environment. Therefore, in order to construct different MXenes, multiple alternative etching techniques have been created employing a variety of etchants, such as a combination of salts of lithium fluoride (LiF) and hydrochloric acid (HCl), ammonium bifluoride, and in-situ HF approaches. As an illustration, Wang et al. [59] utilized the hydrothermal -soaking strategy to fabricate the Ti_3C_2 MXene from Ti_3AlC_2 MAX phase
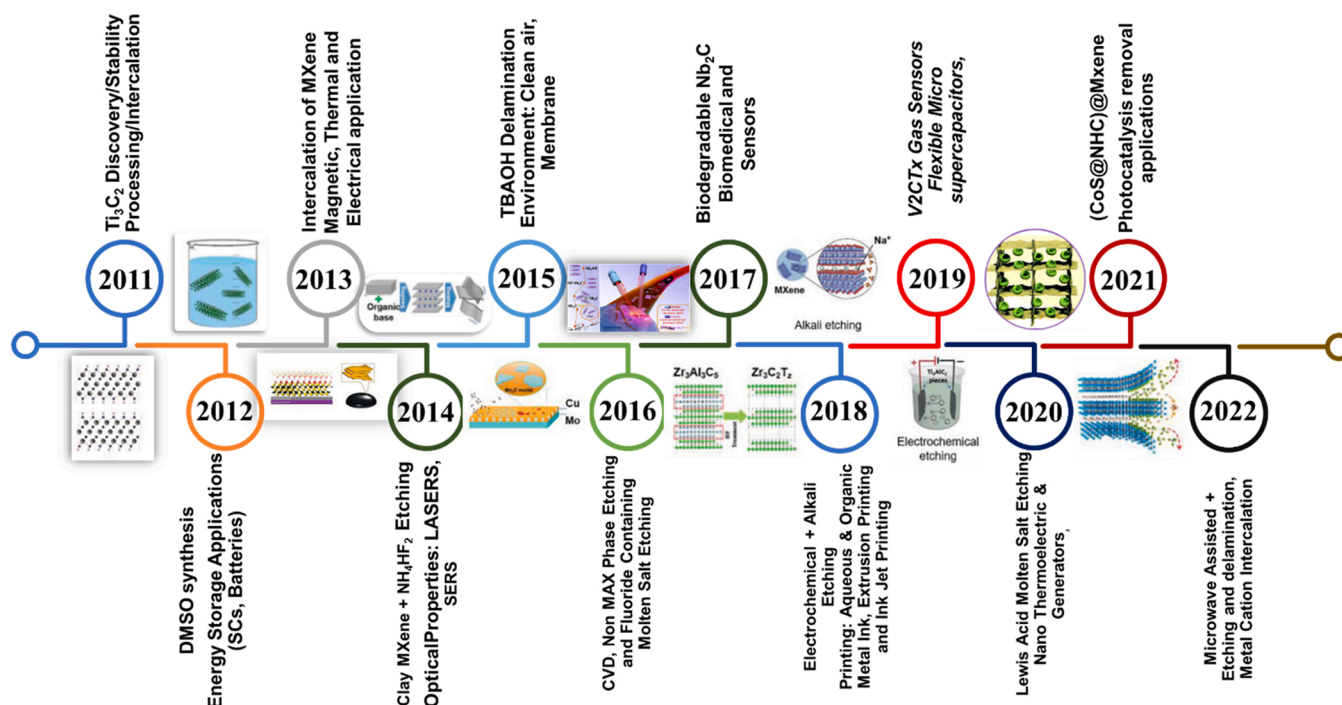
Fig. 3. Timeline for development in interlayer MXene synthesis strategies: From discovery to till date. Reproduced with permission from [57,61,73–77,80].

using NH_4F solution and HCl/LiF etchant solution. The etching of layers can be credited to in-situ HF formation, and the reaction trajectory can be understood by the following equations:

$$LiF + HCl \rightarrow HF + LiCl \tag{4}$$

$$NH_4F + H_2O \rightarrow NH_3 \cdot H_2O + HF \tag{5}$$

However, due to slow pace of etching through mild etchants, fewer crystal defects and intercalation of water molecule cations between the MXene layers arise. Similar to MAX-phase synthesized MXenes, they can also be fabricated from non-max and i-max phases [47]. For instance, Meshkian et al. [60] were the first to fabricate the Mo-based (Mo_2C) MXene from the Mo_2Ga_2C (non-MAX phase) through the selective etching of the gallium (Ga) layer utilizing 50%wt HF concentration. It is evident that the 'A-C′ etching from (non-MAX phase) fallouts in a more conducive MXene compared to the aforementioned etching of 'A′ element from the MAX-phase. Moreover, Zhou et al. [61] fabricated Zr_3C_2 MXene by selectively etching the Al_3C_3 layers from the $Zr_3Al_3C_5$ (non-MAX phase). The reaction mechanism can be summarized in the form of reactions:

$$Zr_3Al_3C_5 + HF \rightarrow AlF_3 + CH_4 + Zr_3C_2 \tag{6}$$
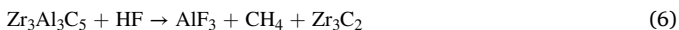
Moreover, several modified-MAX phases have been employed to fabricate MXenes for high-performance applications. For instance, since 2015, o-MAX phases (layer-by-layer out-of-plane-ordering), including Mo_2TiAlC_2, $Mo_2Ti_2AlC_3$, and Cr_2TiAlC_2, were discovered for synthesis of various o-MXenes like $Mo_2TiC_2T_x$ and $Mo_2Ti_2C_3T_x$ [62]. Further, in 2017, a novel type of ordered quaternary $(Mo_{2/3}Sc_{1/3})_2AlC$ MAX phase was reported for the first time, with the Mo atoms forming a honeycomb lattice and Sc atoms occupying the hexagon centers [63]. Due to their unique in-plane symmetry, these phases called as i-MAX phase with general formula $(M'_{2/3}M''_{1/3})_2AlC$ with M′ atoms occupying the hexagonal corner sites and M″ atoms resting at the central sites. For instance, Chen et al. [64] prepared an i-MAX phase in from of solid-solution $(W_{1/3}Mo_{1/3}R_{1/3})_2AlC$ with R representing Gd, Tb, Dy, Ho, Er and Y elements to fabricate $W_{2/3}Mo_{2/3}(R)CT_x$ MXene. Subsequently, numerous kinds of precursor phases and MXenes were theoretically predicted and

experimentally synthesized and exhibited high-performance in diversified environmental applications, including gas/vapor sensing, monitoring and remediation.

Furthermore, the selective etching process is a kinetically controlled method in which the specific etchants and controlled reaction parameters govern the generation of desired surface functionalities over the surface of 2D MXene [65]. For instance, the utilization of fluorine-based etchants during exfoliation generates -OH, F, and -O surface terminations, while fluorine-free etchants eradicate –F functionalities from MXene's surface. Thus, during the exfoliation process, the stoichiometry and surface chemistries of MXenes can be controlled by modulating reaction parameters in accordance with the targeted application, especially the targeted analyte in the case of devising gas/vapor sensor. A comprehensive picture of different MXenes fabricated with respective precursors using various etchants leading to specific surface functionalities has been summarized in Table 1.

However, these mechanical vibration techniques lead to a significant number of flaws in MXenes, which disrupt their physicochemical properties and impair their sensing capabilities [58,68]. Additionally, using poisonous, dangerous, and volatile etchants used in physical techniques pollutes the environment and endangers the safety and health of both users and manufacturers. These risks can be minimized by adopting less corrosive precursors, green precursors and alternative bottom-up strategies.

As a result, several bottom-up processes, including atomic layer deposition (ALD), chemical vapour deposition (CVD), and plasma-enhanced pulsed laser deposition (PEPLD), have been employed for the production of MXene [50,58]. For instance, Gogotsi et al. [69] were able to manufacture an ultrathin molybdenum carbide MXene by reducing a two-layer substrate of copper placed over molybdenum foil (size 100 m) in low methane concentrations at T~1085 °C. Additionally, using a single layer of $Ti_3C_2T_x$ MXene, Sang et al. [70] achitected several 2D titanium carbide MXenes, including TiC, Ti_4C_3, and Ti_5C_4, using the homoepitaxial Frank-van der Merwe atomic layer growth (HFALG) method. Although these techniques avoid user-related risks and secondary contamination, they are challenging, costly, and time-consuming to implement. It limits their economic opportunities,
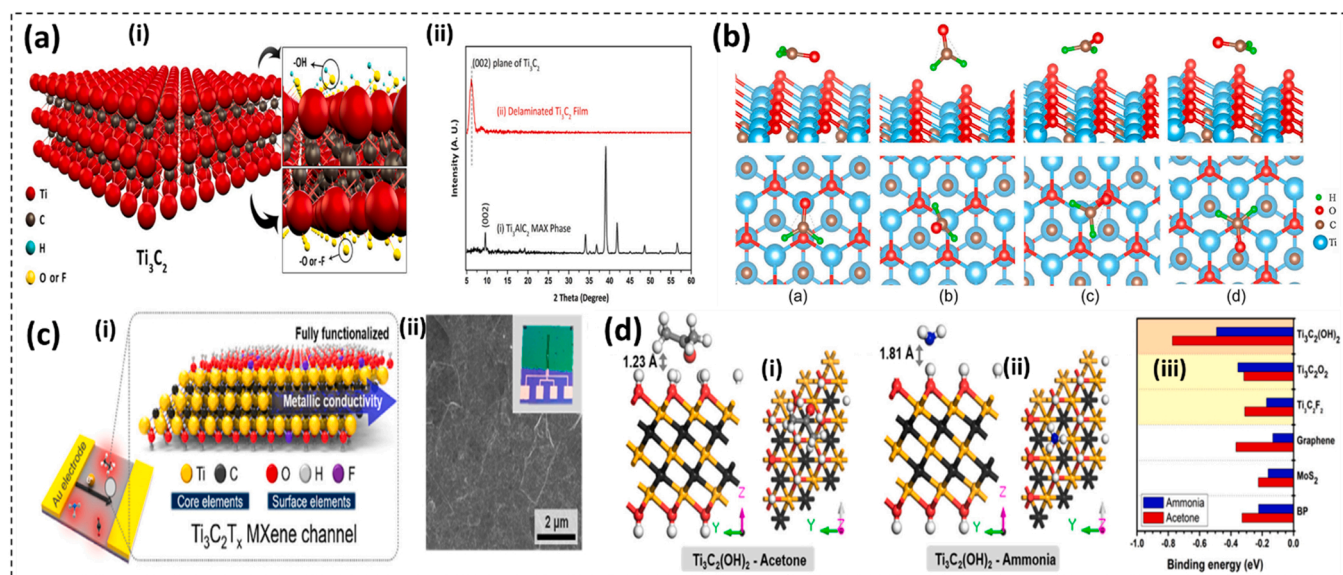
Fig. 4. (a) Schematic illustration of MXene structure with various functional groups on the MXene surface and XRD spectra of fabricated MXene before and after etching [83]. (b) Different adsorption configurations HCHO on $Ti_3C_2O_2$ nanosheets. The upper panel shows the side view, while the lower panel shows the top view [84]. (c) Schematic representation of the $Ti_3C_2T_x$ films with their atomic structure and SEM image of the film surface, along with the inset photographic image of a film sensor [85]. (d) DFT simulation outcomes for gas molecules adsorbed on different 2D materials [85].

which leads to the adoption of top-bottom etchant-based techniques for the scalable manufacture of MXenes. Therefore, for the scalable production of MXenes, exfoliation approaches are favored over these techniques.

Besides, various physical approaches for top-down MXene synthesis have been reported in the literature, including pulsed laser ablation, ball milling, plasma synthesis, and pulsed wire discharge technique [48,58]. Mostly, these physical strategies are integrated with chemical exfoliating methods to architect desired MXenes. For instance, Su et al. [71] fabricated Ti_3C_2 MXene using a combination of ball milling and etching strategies for electrochemical sensors. Moreover, a combined selective chemical etching with the mechanical wheel technique to synthesize the $Ti_3C_2T_X$ MXenes [50,58]. However, the yield of MXenes through these routes is significantly less, and these routes are preferred for fabricating MXene hybrids. For example, Shang et al. [72] used the combination of ball milling and vacuum filtration techniques to architect sandwich-structured $Ti_3C_2T_X$/cellulose nanofibres/boron nitride hybrids for high-performance thermal and sensing devices. A timeline for development in fabrication strategies to architect MXene has been comprehensively summarized in Fig. 3.

2.2. Pristine MXenes for air contaminant sensing and monitoring applications: Theoretical predictions and experimental evaluations

Pristine MXenes have emerged as advanced air contamination monitoring platforms due to their extraordinary physicochemical properties, including highly dispersible and hydrophilic nature for easy machine processability, metallic conductivity for faster charge transport, large surface-to-volume ratio supporting the high probability of interaction with analytes, and abundant surface functionalities for selective interaction [78-82]. $M_3X_2T_x$-type MXenes, majorly $Ti_3C_2T_x$, are employed for air contaminant sensing owing to their ease of machine processability and higher stability due to strong Ti- bonds [13]. Fig. 4 a (i) and (ii) [83] illustrate the schematic illustration of the MXene structure with the different functional groups and the XRD pattern of the $Ti_3C_2T_X$. From the pattern, it is observed that all peaks linked to MAX phase vanished after the etching due to the elimination of Al and complete delamination of MXene, except that peak which correlated with the plane (002). The peak appeared at (002) further shift toward the

lower angle, illustrating the enhancement in D-spacing and c-lattice parameters of fabricated MXene compared to the MAX phase. Furthermore, the sensor was created by drop casting $Ti_3C_2T_x$ MXene on a PI substrate with pre-deposited Pt-based interdigitated electrodes in a natural environment. The surface resistance of $Ti_3C_2T_x$ MXene was observed to increase on interaction with CH_3OH NH_3, C_2H_5OH, and C_3H_6O, which illustrates its typical p-type semiconducting behavior. It was attributed to the transfer of charges to MXene surface from analyte molecules resulting in reduction of its majority charge carrier (holes) and increased resistance. The fabricated chemiresistor exhibited the highest sensing response towards NH_3 and estimated the lowest detection limit (LDL) of 9.27 ppm towards C_3H_6O. It was ascribed to the domination of –O and –OH surface terminals of MXene during sensing phenomena.

Subsequently, Zhang et al. [84] utilized density functional theory (DFT) and molecular dynamics (MD) and estimated a significant recyclable capture of indoor formaldehyde (HCHO) by Ti3C2Tx MXene. Fig. 4 (b) represents the top and side view of some adsorption configurations of HCHO on MXene nanosheets [84]. The HCHO's adsorption energy for single-molecule adsorption was estimated to be 0.3 eV and 0.45 eV for monolayer coverage in MXenes. Following these fundamentals, Kim et al. [85] designed a $Ti_3C_2T_x$ MXene –based metallic sensor with a high signal-to-noise ratio for sensing several contaminants, including NH_3, SO_2, C_2H_5OH, C_3H_6O, nitrogen dioxide (NO_2), and CO_2 at standard pressure and room temperature conditions. The observed remarkable signal-to-noise ratio was ascribed to the metallic conductivity and full surface termination of $Ti_3C_2T_x$ MXene as illustrated in Fig. 4(c). The SEM image in Fig. 4(c) also illustrates the fabricated flakes were completely gathered into a uniform film, mentioning the flat surface without any visible defects. Moreover, the chemiresistor exhibited higher LDL towards several VOCs (in the range of 50–100 ppb) compared to conventional semiconducting sensors. The experimental results were predicted by theoretical estimations depending on DFT, as shown in Fig. 4 (d) and MD, where Kim et al. [85] explored the role of surface functional groups over air contaminant sensing performance of $Ti_3C_2T_x$-MXene. Their experimental results were supported by estimated larger binding energies of C_3H_6O and NH_3 than other 2D materials.

Further, Shuck et al. [86] investigated the effect of precursor nature on the gas/vapor detection performance of a chemiresistor made of
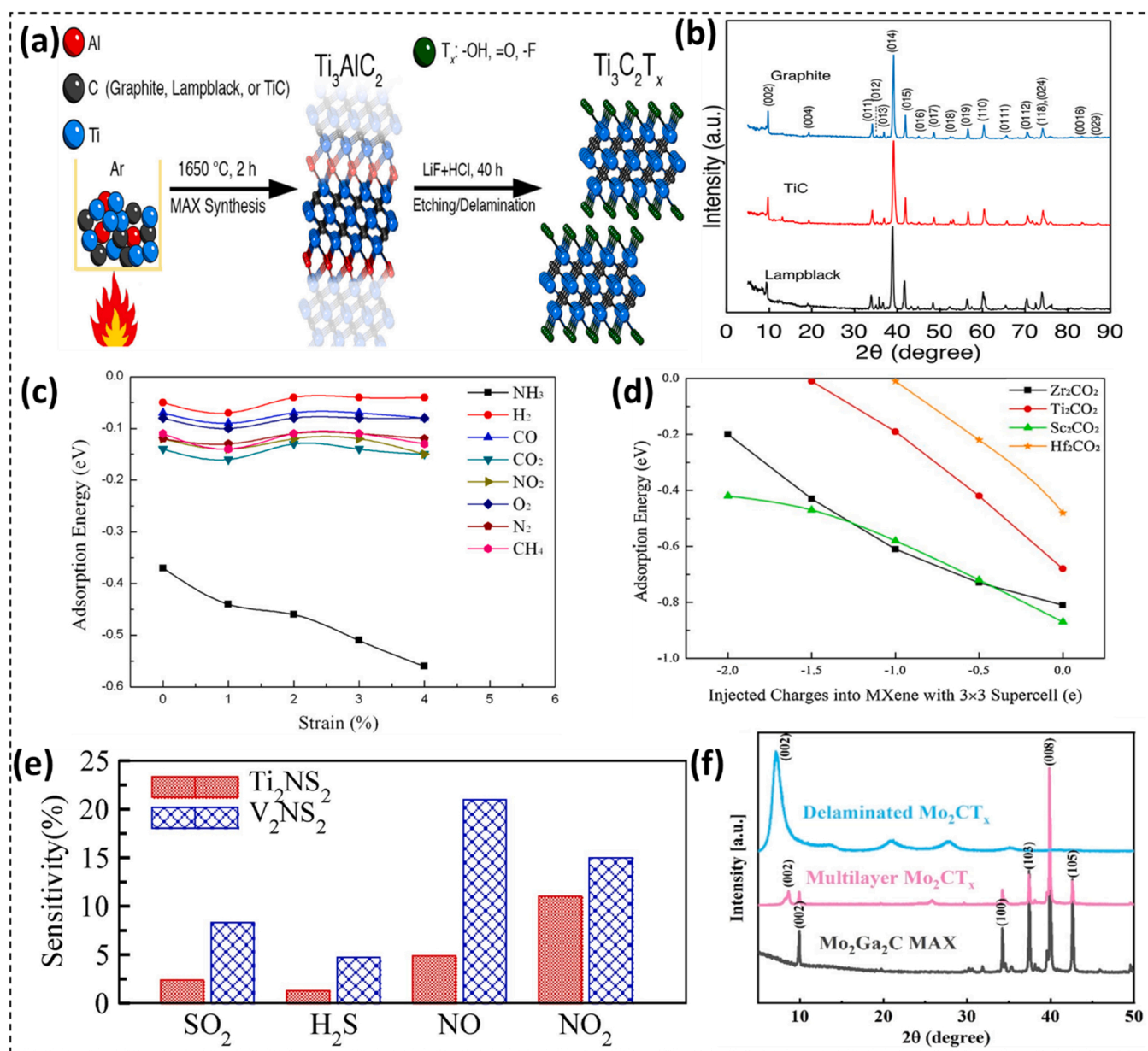
Fig. 5. (a) Schematic diagram of the preparation method of various carbon sources followed by the MXene fabrication [86]. (b) XRD spectra of the powder fabricated from TiC, graphite and carbon lampblack at the temperature of 1650 °C for 2 h [86]. (c) Adsorption energies of gas molecules (comprising NH_3, H_2, CO, CO_2, NO_2, O_2, N_2, and CH_4) on monolayer Ti_2CO_2 as a function of applied biaxial strains [87]. (d) Adsorption energies graphical representation of the $ZrCO_2$, Ti_2CO_2, Sc_2CO_2 and Hf_2CO_2 [88]. (e) Sensitivity graphs for various gaseous molecules on the Ti_2NS_2 and V_2NS_2 surfaces [90]. (f) XRD spectra of the Mo_2Ga_2C phase, HF-etched Mo_2Ga_2C phase, and delaminated Mo_2CT_x phase [92].

$Ti_3C_2T_x$ MXene. The results showed that the $Ti_3C_2T_x$-MXene derived from the MAX precursor had a higher sensing response than those made with carbon black/graphite, as shown in Fig. 5 (a). The fabricated $Ti_3C_2T_x$ MXene exhibited the utmost sensing response towards NH3 compared to other analytes, which can be attributed to higher interaction between reducing NH3 molecules and metallic conducting $Ti_3C_2T_x$ MXene layers. These outcomes suggested the utilization of $Ti_3C_2T_x$ MXene derived from MAX precursor for air contaminant monitoring compared to other MXenes owing to its higher conductivity and proper etching. This has been followed in further studies dedicated to pristine $Ti_3C_2T_x$ MXene based gas sensing evaluations. In addition, the XRD pattern in Fig. 5 (b) illustrates the 95% purity of MAX phase (Ti_3AlC_2) along with the 1% purity of Ti_2AlC for the prepared graphite sample, similarly 93% and 72% purity for the carbon lampblack and with TiC respectively. This wide difference in the final composition indicates that

the reaction mechanism is unstable; possibly adjusting the reactant and synthesis time would be required to achieve maximum equilibrium.

Furthermore, it was discovered that $M_2X_2T_x$-type MXenes, particularly vanadium carbide (V_2CT_x) and niobium carbide (Nb_2CT_x), have a larger effective surface area due to fewer atomic layers than $M_3X_2T_x$-type MXenes, which is critical for designing chemiresistive mode air contaminant monitoring strategies [4,13]. It's interesting to note that M_2XT_x-type MXenes were theoretically evaluated for air contaminant detection before $M_3X_2T_x$-type MXenes. Yu et al.'s [87] first theoretical report investigated the interaction of several air contaminants with the Ti_2CO_2-MXene surface. The results demonstrated the efficient adsorption of NH3 molecules over the Ti_2CO_2-MXene surface due to forming N-Ti bonds by transferring a larger amount of charge with a magnitude of 0.174e. Other contaminant molecules, on the other hand, were not adsorbed on the Ti_2CO_2-MXene surface. It is attributed to the high

adsorption energy of NH₃ (−0.37 eV) over the surface of Ti_2CO_2-MXene (Fig. 5 (c)). The adsorption of NH_3 molecules was reversible by turning off the applied biaxial strain. Moreover, due to its high conductivity, the Ti_2CO_2-MXene exhibited a higher sensing response towards NH_3 than other 2D materials like MoS_2 and phosphorene. Similarly, Xiao et al. [88] investigated the adsorption of several contaminants (N_2, NO, NH_3, CO, CO_2, O_2, H_2, and CH_4) on the surface of M_2CO_2-MXene (M = Zr, Ti, Sc, and Hf). Except for NH_3, all other tested contaminants were physisorbed on the M_2CO_2-MXene surface. As shown in Fig. 5 (d), Zr_2CO_2-MXene exhibited chemisorption of NH_3 by transferring two electrons to its surface, which was attributed to higher adsorption energy (−0.81 eV) and charge transfer (0.188e) of NH_3 towards MXene. Furthermore, Ma et al. [89] used DFT and MD studies to explore the enormous potential of M_2CO_2-MXene for selective SO_2 detection. In comparison to other analytes, the results revealed an intriguing fact that only SO_2 molecules were physisorbed on the Sc_2CO_2 surface. It was attributed to the orbital hybridization of SO_2 molecules and MXene in the predicted density of states, resulting in metallic conductivity and improved charge transfer in the interaction environment. Besides, Naqvi et al. [90] described the air contaminant (H_2S, NH_3, CO, SO_2, NO_2, CH_4, CO_2, and NO) monitoring performance of nitrides MXenes M_2NS_2 (M = Ti, V). The outcomes showed a reversible adsorption-desorption behavior towards NO on Ti_2NS_2 and V_2NS_2 MXenes, which has the potential to be developed as high-performance air contaminant monitoring platforms. Moreover, the sensitivity of these devices having various gaseous molecules in Fig. 5 (e) indicates that the devices towards NO and NO_2 appeared highly sensitive while showing less sensitivity for the H_2S and SO_2 gas molecules, respectively.

Lee et al. [91] utilized V_2CT_x-MXene based chemiresistor to detect polar and non-polar air pollutants. The fabricated chemiresistor exhibited larger selectivity for detecting hydrogen (H_2) amongst all observed analytes due to the appearance of 'V'. It shows that the selection of transition metal in MXene results in detecting the desired analyte with high-order selectivity. Nevertheless, the practical viability of the fabricated chemiresistor was limited due to a larger recovery time of around 7 min and 5.5 min for H_2 and methane (CH_4), respectively. Besides, Guo et al. [92] investigated a chemiresistor based on Molybdenum carbide (Mo_2CT_x)-MXene for detecting various VOCs. The primary goal of this research is to optimise MXene concentration and sonication time in order to improve air contaminant detection performance. The XRD patterns (Fig. 5 (f)) reveal the Mo_2Ga_2C phase, HF-etched Mo_2Ga_2C phase, and delaminated Mo_2CT_x phase. The figure clearly shows that the strong peaks are formed at (002) plane in the D-Mo_2CT_x pattern, which indicates the enhancement in the c-lattice parameter of the prepared MXene due to the TMAOH intercalation and the termination of MAX phase from the prepared suspension. However, due to its high metallic conductivity, the fabricated sensor showed almost negligible recovery. Nevertheless, the experimental evaluations of M_2XT_x-type MXenes are hindered due to the lower stability and complex processing.

2.3. Limitations associated with pristine MXenes related to manufacturing, stability and air contaminant monitoring

The practical applications of pristine MXenes for air contaminant monitoring require imperative expansions towards ambient stability, stoichiometric optimization and scalable/safe manufacturing [4,12,82]. These critical limitations are related to manufacturing strategies, scalable manufacturing, secondary environmental contamination and associated health hazards, production of nanoscale waste, and ambient stability of MXenes due to restacking of layers. The state-of-the-art pristine MXene synthesis is conquered by hazardous corrosive acid-based exfoliation, harmfully impacting the ecosystem [48,50,58]. Additionally, the latest fabrication methods entail in-situ HF production, which to a certain extent, pollutes the environment. These fluorine-based precursor assisted harnessing routes result in MXene with

larger fluorine surface terminals, which are highly unfavorable for air contaminant detection [58]. It can be avoided by adopting greener synthesis routes comprising chemical vapor deposition (CVD), salt-template growth, or green precursor assisted routes [50,69]. Moreover, the high metallic conductivity of pristine MXenes limits their utilization for reducing analytes compared to oxidizing analytes [93]. Their uncontrolled high surface reactivity leads to higher binding of analyte molecules resulting in non-recoverable sensing, which limits their commercial viability [4]. Moreover, it leads to instability in oxygen and humid environment, which decreases the lifetime of pristine MXene based air contaminant monitoring chemiresistors [12,17]. It raises the quest of exploring the methods to uphold the interlayer separation and modulate surface chemistry of MXenes for better sensing performance and stability, which is done by fabricating interlayer engineered MXenes (ILe-MXenes).

3. Interlayer engineering of MXenes: Intercalation and surface functionalization for air contaminant monitoring

The multilayer MXenes produced in the preliminary stage of exfoliation possess significant layer stacking and instability in oxygen environment, which raises issues of storage and stability, hindering their scalable and commercial applications [4,12]. Thus, it is indispensable to either isolate the individual MXene layers or insert them with other materials to prevent restacking and modulate their surface functionalities to achieve ambient stability. It is done by various strategies, including intercalation and delamination, surface engineering, heteroatom doping and hybridization [4,48,55]. The processing of MXenes through these routes not only prevents restacking and oxidation but also modulates the interlayer distance. Since the airborne contaminant sensing phenomenon depends upon the interaction between analyte molecules and MXenes, its performance is highly dependent on its effective surface area, surface functionalities, porosity and physicochemical attributes [13]. Moreover, the physicochemical attributes, effective surface area and porosity can be easily tuned by optimizing the interlayer distance of MXene layers. For instance, by increasing the interlayer distance, more analyte molecules can penetrate interlayer gap of MXene layers and interact more, providing a strong sensing signal. Additionally, the electrical properties, such as conductivity of MXenes, can be tuned by introducing dielectrics between the MXene layers, which can be optimized to detect the specific type of analyte (reducing or oxidizing), providing selectivity to sensing device [4,13]. Hence, optimising the interlayer distance of MXene layers is highly desirable for high-performance sensing applications, especially for gas/vapor sensing and monitoring. It results in the formation of interlayer engineered MXenes, i.e. ILe-MXenes, which have been extensively utilized for gas/vapor sensing applications because of their superior stability, selectivity and sensitivity. Various strategies to engineer interlayer distance of MXenes to achieve desirable Ile-MXenes with optimized properties as per targeted applications have been developed with time with scalable prospects.

3.1. Intercalation-Delamination Engineering to architect ILe-MXenes

The ML MXenes obtained from exfoliation stage are majorly unstable due to restacking their layers. It necessitates the requirement of either separate/reduce ML MXenes into single/FL MXenes, or preventing the restacking by inserting other elements/ions/materials between its layers. The former process of reducing ML MXene to FL/single-layer MXenes is done through delamination agents, including organic solvents, sonication and mechanical peeling [50,58]. For instance, Naguib et al. [76] described utilization of different organic solvents for delaminating SL/FL MXene sheets. These delaminated MXenes possess high specific area and are very useful in fabricating miniature gas/vapor sensors, where SL/FL materials are prerequisites for sensing layer fabrication. Moreover, during delamination process, the insertion of
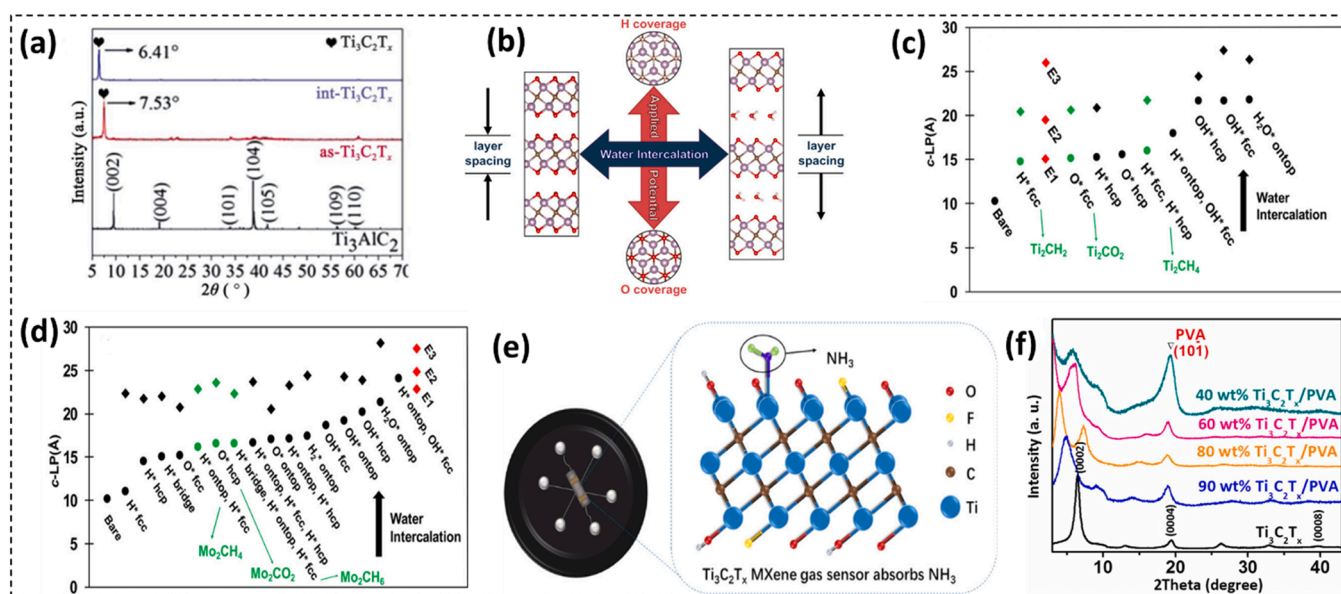
Fig. 6. (a) XRD spectra of Ti_3AlC_2 and $Ti_3C_2T_X$ describing the c-lattice parameters. [95] (b) Schematic illustration of the surface chemistries of MXene through water intercalation [96]. (c-d) Measure out-of-plane lattice parameter *c*-LP for Ti_2C and Mo_2C with various functional groups emphasized in (circle) and same functional group along with one single layer of intercalated water mentioned in (squares). The green circles are related to the functionalized MXene systems with the lowest free energy [96]. (e) Schematic representation of the MXene based sensor for ammonia detecting [97]. (f) XRD spectra of the MXene and MXene/PVA film with different wt% content [98].

delaminating agents/ions can tune the interlayer spacing. However, the more controlled and convenient route to engineer ILe-MXenes and modulate their interlayer space is intercalation [94], which has been significantly utilized for improving gas/vapor sensing performances. Ile-MXenes possess abundant electrochemically active sites, higher specific surface area and porosity, and enhanced structural stability, felicitating MXene surface-environment reactions, ion/analyte diffusion and transport, and long-term stability, which are essential to architect air contaminant detecting, monitoring and remediating devices. Various intercalation strategies have been employed for fabricating Ile-MXenes from pristine MXenes, including cationic intercalation, organic base assisted intercalation, molecule mediated intercalation, and SL/ML delamination.

3.1.1. Molecule-mediated intercalation to architect ILe-MXenes

Molecule-mediated intercalation is an effective strategy to architect Ile-MXenes using molecule-based intercalants such as dimethyl sulphoxide (DMSO), water (H_2O), and polymers. Generally, the pristine MXene obtained as a result of chemical/physical exfoliation is intercalated through H2O molecules to avoid the restacking of its sheets, which not only provides stability to its structure but also enhances the IL spacing of MXenes with several surface modifications [94]. As an example, Wang et al. [95] exhibited the intercalation of $Ti_3C_2T_x$ with H_2O molecule notably enhanced its c-lattice parameter (c-Lp) (23.4 Å) compared to that of its MAX precursor, Ti_3AlC_2 (18.6 Å). Moreover, c-Lp was increased up to 27.6 Å through DMSO molecule mediated intercalation, as highlighted in Fig. 6 (a). These results were supported by theoretical density functional theory (DFT) based outcomes and experimental observations of Fredrickson et al. [96] exhibiting out-of-plane c-Lp of Ti_2C, and Mo_2C MXenes is highly increased upon water-mediated intercalation Fig. 6 (b). They revealed that the c-Lp significantly depends upon the exact hydration conditions and varies accordingly, which is a smart route to tune its electrical and catalytic attributes according to targeted application, as illustrated in Fig. 6 (c-d). It has been observed that the intercalation of MXenes is the easiest with utilizing water. Fascinatingly, this ease of intercalation of H_2O molecules amongst the MXene layers makes them a potential candidate for architecting humidity sensors.

Besides, the DMSO assisted intercalation of MXenes results in higher and selective adsorption of CO_2, turning it promising for CO_2 monitoring and capture [94]. Notably, the volume capacity of ILe-$Ti_3C_2T_x$ increases up to 502 V v^{-1}, which is higher than well-established sorbents. Moreover, the combination of deionized water (DI) and DMSO can be utilized for tuning the interlayer spacing of MXenes, resulting in ILe-MXenes with a high specific surface area. For instance, Wu et al. [97] adopted a liquid phase immersion strategy through centrifugation of $Ti_3C_2T_x$ in DI water and DMSO solution to fabricate ILe-$Ti_3C_2T_x$ with enhanced ammonia sensing attributes, as mentioned in Fig. 6 (e). In contrast, Ling et al. [98] reported an increase in c-Lp of pristine $Ti_3C_2T_x$ from 27.6 Å to 35.3 Å through intercalating with 10% wt poly vinyl alcohol (PVA) molecules through a simple vacuum filtration route Fig. 6 (f). By summarizing these outcomes, it can be stated that the intercalation of different molecules amongst MXene layers surges its interlayer distance, which can be confirmed by monitoring c-Lp values experimentally and theoretically, resulting in the formation of Ile-MXenes favorable to be employed in diversified applications such as gas sensing, where higher surface area and long-term stability are prerequisites.

3.1.2. Cationic intercalation to architect Ile-MXenes

Cationic intercalation is one of the prominent intercalation strategies utilized in fabricating ILe-MXene from ML-MXenes by surging their interlayer spacing. The strategy adopts two routes: aqueous medium assisted cationic intercalation and non-aqueous intercalation [55,94]. Several cations, such as K^+, H^+, Li^+, Mg^{2+}, NH^{4+}, Na^+ and Al^{3+}, are employed as intercalants amongst the MXene layers through adopting aqueous solutions mediated cationic intercalation strategy [55]. During aqueous solutions mediated intercalation, the physicochemical attributes of the fabricated Ile-MXene can be controlled by optimizing the pH of solution and nature of cation and medium. For instance, for high pH solutions, such as K^+ and NH_4^+ solutions, the c-Lp of ILe-$Ti_3C_2T_x$ can be surged by 5.1 Å as compared to that of pristine $Ti_3C_2T_x$ [74]. Generally, liquid phase immersion route is adopted for intercalating metal cations such as Na^+ between the MXene layers. Following this route, Koh et al. [49] and Yang et al. [99] reported a surge in interlayer spacing of $Ti_3C_2T_x$-MXene through intercalation with Na^+ ions. They reported that the interaction with Na^+ serves dual purpose of increasing interlayer
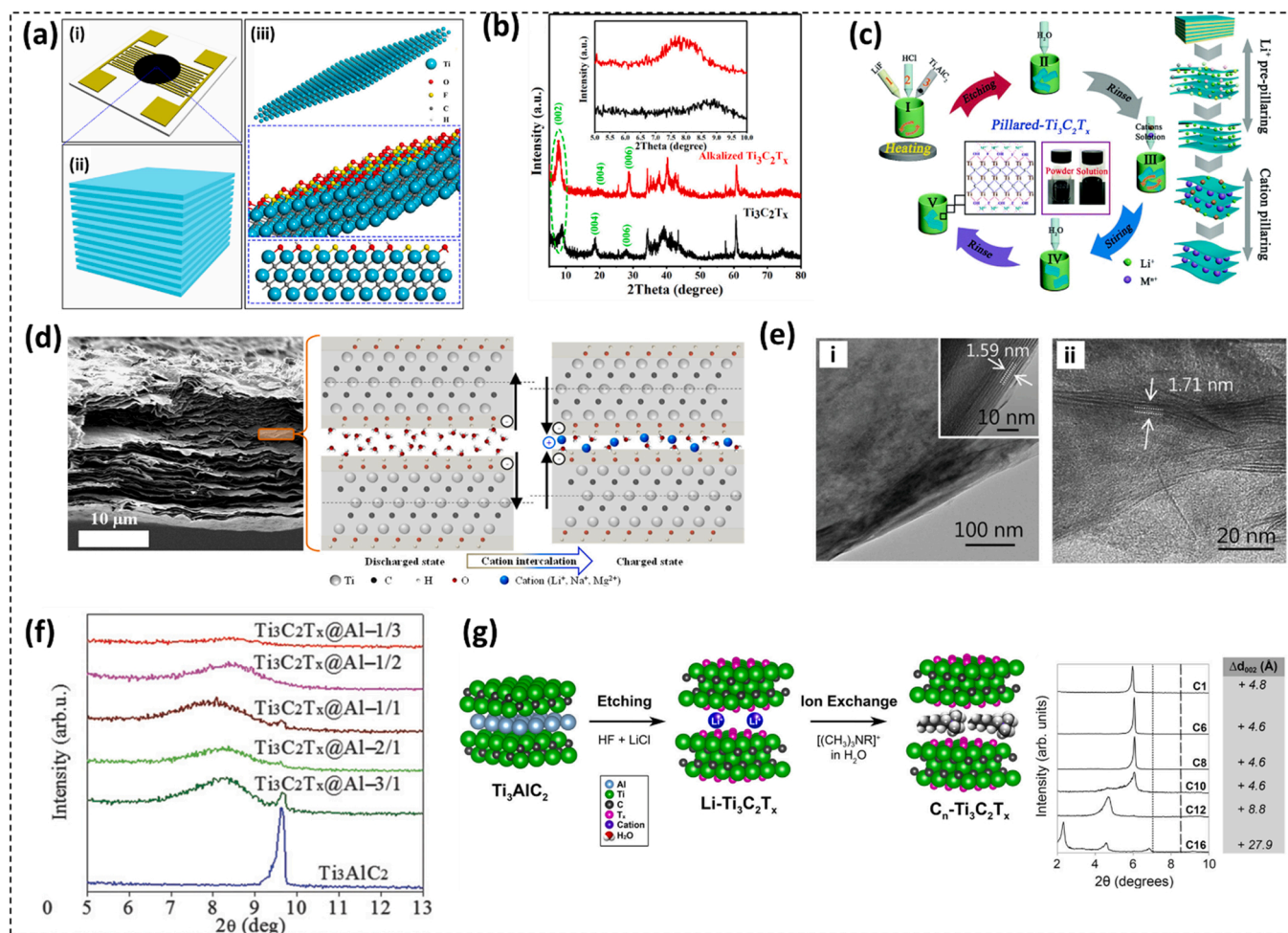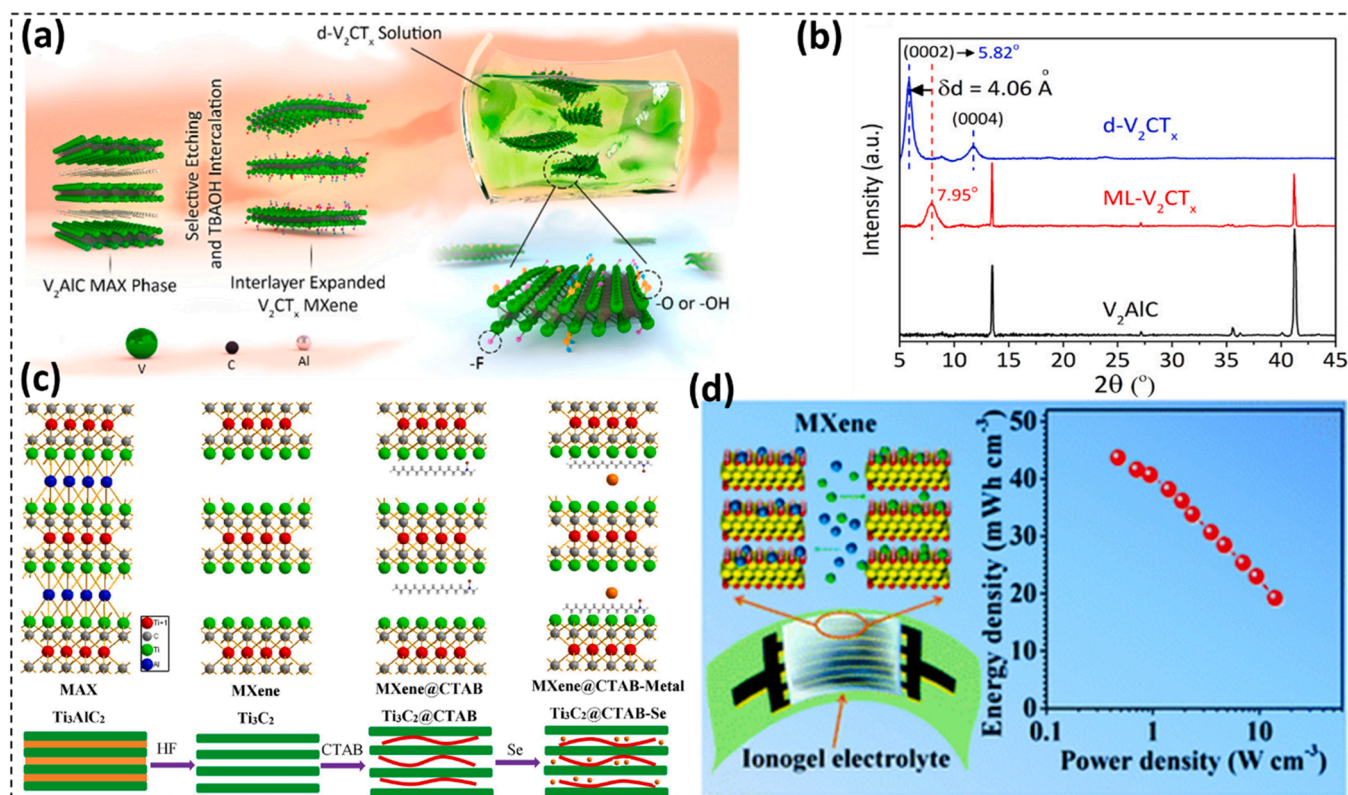
Fig. 7. (a, i) Schematic illustration of the device based on Ti₃C₂Tₓ, and representing the (ii) organ-like structure of the MXene, and (iii) Single sheet after stratification and the functional terminals on the surface of the prepared MXene [107]. (b) XRD pattern of the fabricated MXene and alkalized MXene [107]. (c) Schematic representation of the fabrication process of MXene alteration via two step pillaring strategy [100]. (d) Schematic illustration of the MXene based paper electrode upon intercalation of ions [101]. (e) SEM images of the fabricated MXene illustrating the interlayer distance [102]. (f) XRD spectra of the sample illustrating the (002) peaks [103]. (g) Schematic illustration of the prepared sample and corresponding XRD graph of the intercalated MXene [104].

distance between the Ti₃C₂Tₓ layers and modulating its surface terminal oxygen–fluorine ratio ([O]/[F]), which is key to attain selectivity in air contaminant monitoring applications of MXenes as mentioned in Fig. 7 (a). Whereas the XRD pattern in Fig. 7 (b) illustrates the alkalized Ti₃C₂Tₓ and Ti₃C₂Tₓ pattern in which, after the alkalization of MXene, the characteristics peaks are appeared at plane (002) for the MXene, and exhibits stronger and strengthen. Similarly, the peak was also shifted towards the diffraction angle, while the Na⁺ intercalation enhanced the c-lattice parameter of the sample. In addition, the peaks (004 and 006) also shifted towards the greater angle along with peak (004) representing weakening and peak (006) displaying strengthening, respectively.

Likewise, Li et al. [100] demonstrated the fabrication of ILe-MXene by the facile cationic pre-pillaring strategy utilizing various cations, including K⁺, Li⁺, Ca²⁺, NH₄⁺, Mg²⁺, and Al³⁺ with enhanced interlayer distance with 17.02% enhancement Fig. 7 (c). Interestingly, Come et al. [101] reported that the choice of cation regulates the mechanical attributes of MXenes. They demonstrated that interlayer space deformations induced in MXenes are highly dependent on the nature of intercalant cation Fig. 7 (d). It was observed that the intercalation of K⁺ ions resulted in the expansion of IL space in MXenes. In contrast, intercalation with Li⁺, Mg²⁺ and Na⁺ resulted in its contraction, which was attributed to the variance in intercalants ion radius.

Besides, Deng et al. [102] reported that the interlayer distance in

MXene was enhanced up to 1.71 nm from 1.59 nm of bare MXene on mixing with Fe²⁺ ions using gelation strategy. It is attributed to the dual action of Fe²⁺ ions, including linking with MXene nanosheets and intercalating it during the gelation process, as illustrated in Fig. 7 (e). Moreover, MXene nanosheets restacking was efficiently evaded by Fe²⁺ intercalation. Further, it must be noted that the intercalation of cations is not only done by outside additives but also from inherent atoms by partial etching of MXenes. Following this, Guo et al. [103] proposed the partially etched Al layers from Ti₃AlC₂ precursor to fabricate Ti₃C₂Tₓ with suitable Al-IL (Ti₃C₂Tₓ-Al), which had a high specific surface area. The etching of Al layers resulted in releasing additional space while the remnant intrinsically bound Al aided as "electron bridges" amongst Ti3C2Tx layers, felicitating charge transport, analyte diffusion and long-term stability. The interlayer spacing of Ti3C2Tx-Al was increased from 9.17 to 10.57 Å, signifying its high surface area advantageous for surface reaction-based applications Fig. 7 (f). Besides monoatomic cationic intercalation, Ghidiu et al. [104] and Wang et al. [105] adopted larger polyatomic cations mediated intercalation to enhance the interlayer spacing in ILe-MXenes further. These polyatomic cations include alkylammonium cations ([(CH₃)₃NR]⁺ with R representing CH₃, C₆H₁₃, C₁₀H₂₁, C₁₂H₂₅, C₁₆H₃₃) and aryl diazonium salts (⁺N₂-phenyl-SO₃H) utilizing ion-exchange strategy. It results in tuning the interlayer distance of MXenes in the range of 5–28 Å by modifying the alkyl chain length of alkylammonium cations and widening its intercalation

Fig. 8. (a-b) Schematic of the fabrication and delamination process of V_2CT_X MXene extracted from MAX phase and XRD spectra of the V_2AlC, ML-V_2CT_x and d-V_2CT_x MXenes [91]. (c) Schematic illustration of the fabrication process of the Ti_3C_2 @CTAB-Se [109]. (d) Schematic representation of quasi-solid state MXene supercapacitors with the energy and power density relation [110].

chemistry, as revealed in Fig. 7 (g). Furthermore, VahidMohammadi et al. [106] extended the application of cationic intercalation in fabricating ILe-MXenes to M_2CT_X-MXenes by demonstrating the attainment of self-assembled highly-stable ML V_2CT_x films owing to electrostatic attractions. Summing up all the outcomes, it can be observed that the cationic intercalation is a multipurpose strategy to enhance MXene's specific surface area and porosity, giving it structural and long-term stability, tuning its physicochemical attributes in optimized manner and inducing chemical and surface modifications of MXene layers, resulting high-performance ILe-MXene systems for diversified applications, where controlled optimization of surface interactions and chemistries are prerequisite.

### 3.1.3. Organic base assisted intercalation to architect ILe-MXenes

Various challenges associated with cation-mediated intercalation, which limits their applications. It includes smaller expansion in interlayers due to their minute size and smaller volume. Moreover, the cationic intercalation is not applicable to the entire MXene family. For instance, Naguib et al. [76] exhibited that carbide based MXenes can be intercalated using cationic intercalation and molecular intercalation, but nitride-MXenes could not. Contrary, organic bases and macromolecules are multipurpose for fabricating ILe-MXenes. Mashtalir et al. [108] employed isopropylamine (i-PrA), an organic base, to intercalate $Nb_4C_3T_x$, $Ti_3C_2T_x$, and Nb_2CT_x. During aqueous intercalation, i-PrA forms ammonium cations intercalating Nb_2CTx layers driven by electrostatic forces. Besides, the unique molecular structure of i-PrA contributed to overcoming steric hindrance and pushing MXene layers apart, resulting in ILe-Nb_2CT_x with increases c-Lp of 45.4 Å compared to that of pristine Nb_2CT_X (20.8 Å). Apart from i-PrA, other organic bases, such as choline hydroxide, n-butyl amine and tetrabutylammonium hydroxide (TBAOH), were observed to induce spontaneous swelling resulting in lowering of the bond energy amongst the MXene layers

under mild sonication. For instance, Lee et al. [91] adopted liquid phase immersion technique coupled with manual handshaking to obtain ILe-V_2CT_X using a combination of DI water and TBAOH in Fig. 8 (a). The X-ray diffraction (XRD) outcomes in Fig. 8 (b) revealed that the XRD-peak relates to (0002) planes of V_2CT shifts to about 5.82° from 7.95°, which corresponds to a 4.06 Å and an 8.12 Å surge in the D-spacing and c-Lp of ILe-V_2CT, respectively. Besides, the ILe-V_2CT exhibited an ordered stacked structure compared to the accordion-type structure of pristine V_2CT, demonstrating excellent gas monitoring efficacies towards several non-polar gases. Moreover, TBOAH exhibited versatility in intercalating various MXenes, including V_2CT_x, $V_4C_3T_x$ and Ti_3CNT, illustrating the universality of organic base mediated intercalation in fabricating ILe-MXenes.

Recently, Li et al. [109] adopted CTAB as intercalants to expand the interlayer spacing of Ti_3C_2 and consequent selenium (Se) treatment to hinder the Se-dissolution as mentioned in Fig. 8 (c). Apart from the aqueous routes, intercalation of MXenes has also been attained in ionic liquid mediums. Recently, Zheng et al. [110] employed a quasi-solid state gel electrolyte coupled with preintercalation MXene film to obtain ILe-MXene for supercapacitor applications which exhibits the excellent areal (13.9 μW h cm^{-2}) and volumetric (43.7 mW h cm^{-3}) energy densities respectively Fig. 8 (d). Though the potential of ionic liquid mediated intercalation routes is enormous in synthesizing high-performance ILe-MXenes, their applications are limited to devising energy storage strategies to date. Combining the outcomes from organic base intercalated MXenes, it can be stated that it is a universal technique to surge the interlayer distance of the family of MXenes with applications in diversified sectors, including environmental remediation and energy storage applications.

3.1.4. Physical delamination to engineer ILe-MXenes

In general, the ultimate goal of intercalation processes is to reduce
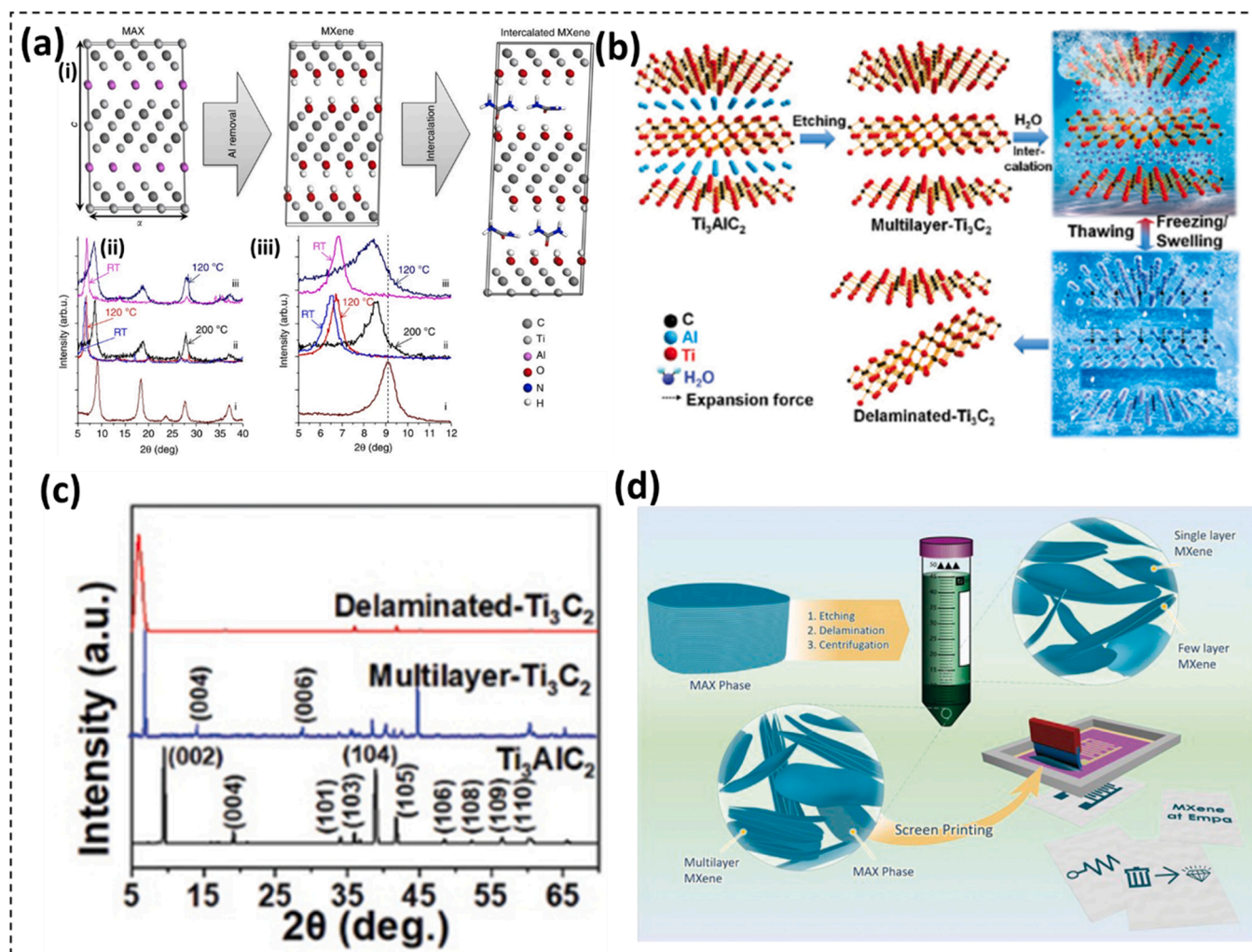
Fig. 9. (a) Schematic illustration of physical fabrication of MXene with the corresponding XRD pattern illustrating the enhancement of c-lattice parameter. [112] (b) Schematic illustration of the fabrication process of the delaminated-Ti$_3$C$_2$ through the freeze-and-thaw (FAT) method [113]. (c) XRD patter of the delaminate-Ti3C2 illustrating the peak shift at plane (002) [113]. (d) Schematic illustration of the harnessing of direct screen printing of MXene sediments [114].

ML-MXenes to a few layers or single-layer MXenes, a process known as delamination. MXenes' physical delamination is similar to the exfoliation of other 2D materials such as graphene, MoS$_2$, and borophene. Furthermore, the physical delamination route is analogous to cationic intercalation, in which solvent molecules typically act as intercalants; thus, the physical delamination process is also referred to as molecular intercalation [111].

Mashtalir et al. [112] conducted extensive research on intercalation and delamination for various MXenes, such as Ti$_3$C$_2$, Ti$_3$CN, and TiNbC. They used urea, hydrazine monohydrate (HM), HM in N, N-dimethylformamide (DMF), and HM in DMSO as intercalants. For instance, on treating these various organic molecules, Ti$_3$C$_2$T$_x$ exhibited different interlayer space modulation (HM/DMF treated Ti$_3$C$_2$T$_x$ with enlarged c-Lp increasing from initial 19.5–25.48/26.8 Å, respectively: Fig. 9 (a)). Moreover, Ti$_3$CN and TiNbC intercalated with HM exhibited increased c-Lp. Besides, they observed that weak sonification is enough to fully delaminate the SL-Ti$_3$C$_2$T$_x$ from ML-Ti$_3$C$_2$T$_x$ using DMSO, and DMSO has no intercalation effect on other observed MXenes. Recently, Huang et al. [113] reported a novel and facile freeze-and-thaw (FAT) mediated delamination strategy. It includes utilizing the expansion of water molecules by slowly cooling to − 20 C to overcome the intermolecular forces acting amongst the MXene layers and then thawing, demonstrated in Fig. 9 (b). Generally, FAT assisted delamination with several cycles results in large size MXenes. The XRD outcomes observed

a peak shift in (002) from 7.2 to 5.9, indicating the successful delamination of Ti$_3$C$_2$T$_x$ layer with an enlarged surface area in Fig. 9 (c). Though the FAT route results in unevenly surfaced MXenes due to many folds of MXene layers, they can be enfolded during the slow freezing process. Additionally, there is no fold in ILe-Mxene was observed while using liquid nitrogen for the freezing process, showing that the squeezing step plays a vital role in governing the delamination quality of MXenes. These outcomes can be concluded by stating that the delaminated MXenes, especially SL-MXenes, are important vectors in different applications where a higher surface area is a perquisite.

Overall, the fundamental in-depth examination of the reported literature shows that several cationic intercalants and the majority of organic base intercalants induce swelling, which weakens the IL interactions in MXenes, followed by simple sonication/shaking/agitation, resulting in large-scale delaminated-MXenes or ILe-MXenes. The intercalation of MXenes enlarges by incorporating various intercalants, including metal cations, organic bases, molecules and even polymers. The enlarged interlayer distance of ILe-MXene contributes to various features, including enhanced charge transport, generation of the chemically active site for electrochemical reactions, improving structural and long-term ambient stability, desired surface modification and tuning of surface chemistries, doping through ions and modulation of physicochemical attributes and enlarged porosity for ion/analyte-exchange/movement. Consequently, future research on MXenes must
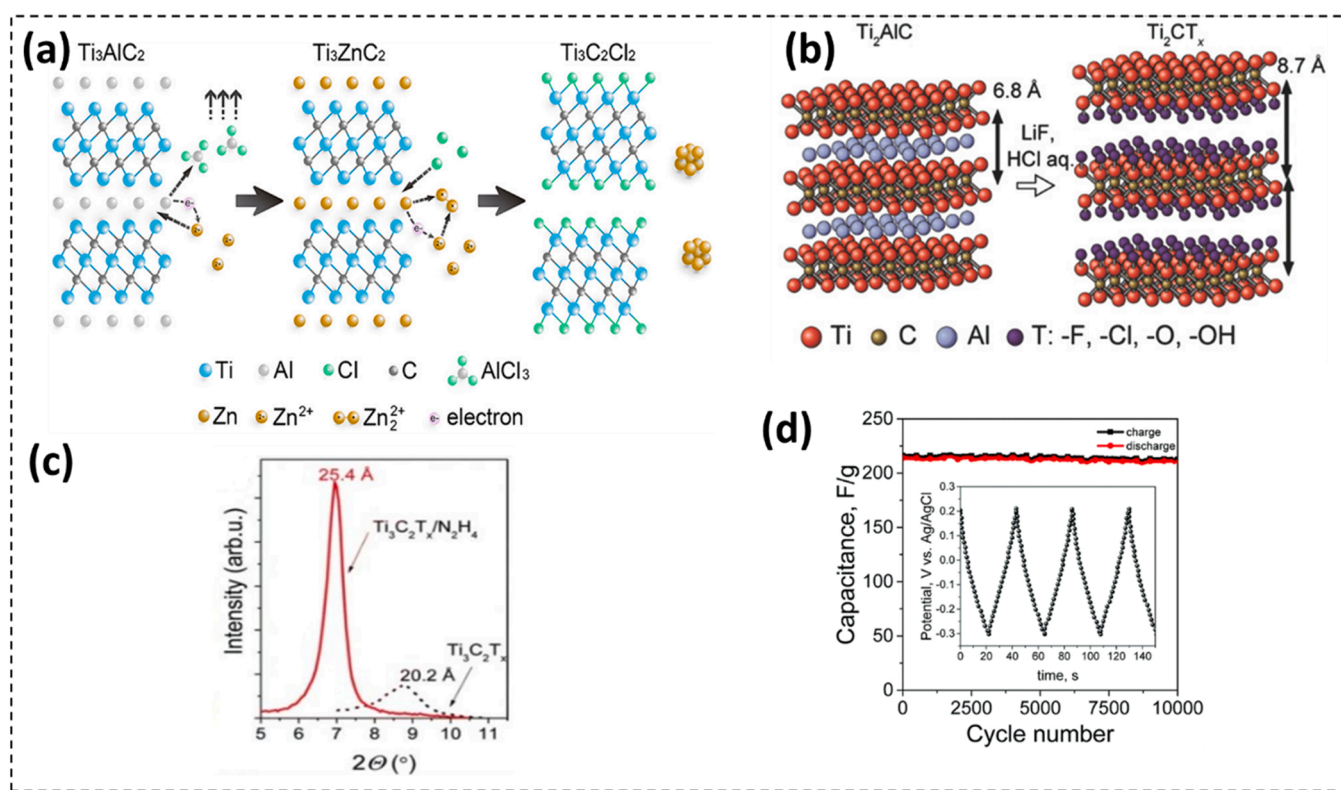
Fig. 10. (a) Schematic illustration of preparation process of MXene utilizing the ZnCl2 salt [117]. **(b)** Schematic illustration of the fabrication of MXene Ti$_2$CT_x by the LiF−HCl treatment of the MAX phase Ti$_2$AlC [118]. **(c-d)** XRD pattern peak (0002) of MXene before and after hydrazine treatment and the conforming c-lattice parameter values and Capacity retention rate of hydrazine treated MXene [119].

be dedicated to evaluating selective and suitable intercalants to fabricate ILe-MXene as per the targeted application. However, most intercalation/delamination strategies include hazardous chemicals, which must be replaced with green strategies consisting of either green intercalants/delaminating agents or repurpose/reuse/recycle of byproducts obtained from this process. For instance, Verma et al. [114] fabricated ink for screen printing from the sediments of unetched precursors and ML-Ti$_3$C$_2$T$_x$ MXenes, as demonstrated in Fig. 9 (d). Furthermore, for scalable production of stable ILe-MXenes with high quality and excellent performance, intercalation/delamination routes other than liquid-phase intercalation and delamination, as well as vapor-solid or vapor-liquid intercalation, must be investigated.

3.1.5. Challenges associated with intercalated/delaminated MXenes: Processability, structural and stability

Other issues pertaining to delaminated and intercalated ILe-MXenes are long-term stability in oxygen and wet environments. It is attributed to the large surface reactivity of ILe-MXenes due to the abundance of surface functionalities that are prone to oxidation [12]. Besides, MXenes are also thermodynamically unstable because of their stoichiometry, in which the edge 'M′' atoms are extremely unstable due to inadequate/weak bonding [4,12,17]. The interaction of 'M′' atoms of MXenes with water/oxygen molecules present in environment results in its structural deformations and increased edge. It steadily results in oxidation of MXene into its transition metal oxides. For example, Ti$_3$C$_2$T$_X$ MXene gradually transforms into TiO$_2$ in oxidative environments like hot surroundings. It results in degradation of performance of ILe-MXenes for different applications due to changes in its unique physicochemical attributes such as hydrophilic nature, thermal or electrical conductivity and mechanical stability. These issues can be task settled through fabricating oxidant-resistant MXenes and preprocessing strategies using surface engineering and heteroatom doping, developing heterostructures through hybridization, and adopting advanced storage

techniques. These methods include storing MXene in an inert atmosphere such as in Argon (Ar) or in organic/inorganic dispersions, low temperature storage to avoid nucleation of 'M′' atoms, attaching anionic salt to edge atoms, and reducing-gas treatment [12]. Besides, fabricating the MXene complexes using hybridization or heteroatom doping and ionic-liquids based dispersion methods are promising anti-oxidant strategies for architecting stable ILe-MXenes. Besides, conventional inert (Ar based) high-temperature treatment (~1200 °C) eliminates surface functionalities of MXenes and induces significant structural ordering to it without destroying its layered structure. This treatment is useful in applications where MXene without surface functionalities is preferred. Consequently, ILe-MXenes must be fabricated rationally according to the requirements of targeted applications.

3.2. Surface Engineering to architect ILe-MXenes for air contaminant monitoring and detection

To cater the issues related to ILe-MXene through intercalation engineering, surface and chemical modifications are induced to ILe-MXenes. In addition to tuning interlayer spacing, surface engineering of MXenes contributes to optimizing physicochemical attributes as per targeted application. Generally, MXenes-based nanosystems can be classified on the basis of surface terminals into halogen surface terminals (–Br, –Cl and –F), chalcogen surface terminals groups (–Te, –S, –OH, –O, –Se), imino (–NH), and null surface terminals [115]. These surface terminals in MXene-based materials can be modified through surface engineering strategies, including surface terminals replacement and heteroatom doping, as per targeted applications.

3.2.1. Surface engineering through surface terminal replacement strategies in architecting high-performance ILe-MXenes

Surface modifications are caused through intercalation, primarily by substituting initial surface terminals and the surface modification of
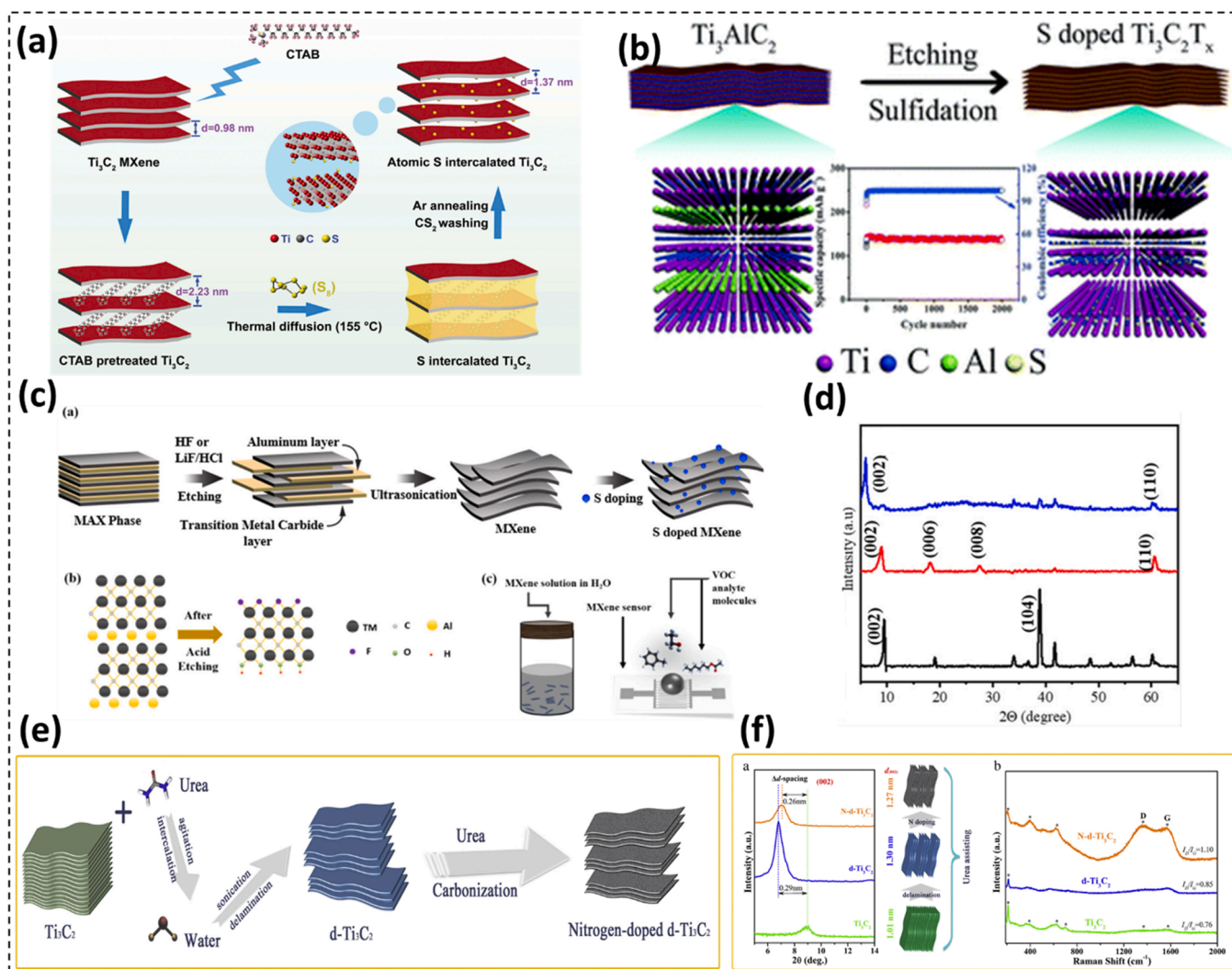
Fig. 11. (a) Synthesis mechanism of S atoms intercalated Ti_3C [122]. (b) Schematic representation of sulfur doped MXene fabrication [123]. (c-d) Schematic diagram of the fabrication route of S-doped MXene at room temperature and XRD pattern of fabricated material after the characterization showing the lattice parameter at (002) plane peaks [124]. (e-f) Schematic diagram of the fabrication method of the nitrogen-doped delaminated Ti_3C_2 nanosheets and XRD characterization of (002) peak of the Ti_3C_2, D-Ti_3C_2, and N-D-Ti_3C_2 samples along with the relevant *d*-spacing values [125].

other ions. The surface engineering in MXenes was first experimentally realized in 2011 with its discovery, in which Ti3C2Tx MXene was etched from its MAX phase using HF exfoliation route resulting in certain –OH and –F surface terminals on its surface [116]. This discovery initiated a quest amongst MXene scientists to modify its surface terminals using various surface engineering strategies as per targeted applications. Recently, Li et al. [117] reported late transition metal halide molten salts (like ZnCl2) based surface engineering, which has moderately strong Lewis acidity and low melting points, as an additive and proved to be universally effective. This approach uses a two-step elemental substitution method on the "A'' atomic plane of conventional MAX phases to yield Cl-surface terminated MXenes, as shown in Fig. 10 (a).

Similarly, halogen-terminal inducement-based surface engineering has been utilized for increasing the interlayer distance to construct ILe-MXenes. For instance, Kajiyama et al. [118] utilized steric chloride termination in MXene to increase its interlayer distance, whereas Mashtalir et al. [119] reported intercalation of hydrazine monohydrate (HMO) to manipulate the Ti3C2Tx surface chemistry in Fig. 10 (b). It was observed that the intercalation of HMO resulted in an increased c-Lp from 20.2 Å to 25.4 Å and a decline in electrochemically inactive Ti-F surface sites, as revealed in Fig. 10 (c). Additionally, the intercalated HMO molecules felicitated the ion transfer by acting as pillars without

hindering the electrochemically active sites. The material also exhibits the volumetric capacitance of 215 F/g (250 F/cm^3) as depicted in Fig. 10 (d), respectively [119].

Besides halogen site substitution, Chalcogen assisted surface terminal substitution, including –OH, –O (epoxy), –S, –Se, and –T, are largely employed to increase the interlayer distance, modify surface chemistries and tune physicochemical features of MXenes resulting into architecting ILe-MXenes. For instance, Jiang et al. [120] exhibited a step-wise functionality-engineering route to architect $Ti_3C_2(OH)_2$ and $Ti_3C_2O_x$ MXenes. Initially, the fabrication of $Ti_3C_2(OH)_2$ through dispersing the intercalated $Ti_3C_2F_2$ MXenes in KOH-based aqueous solution, which resulted in the substitution of –F terminals with –OH terminals attributed to the dissimilarity in bond dissociation energies of Ti–F (about 569 ± 33 kJ/mol) and Ti–O (about 666.5 ± 5.6 kJ/mol) bonds. Additionally, oxygen density coverage in $Ti_3C_2O_x$ surges with the rising of the KOH concentration. The variation in chalcogen site densities was found to alter the electrical and optical attributes of ILe-MXenes, which can be optimized as per the intended application. Moreover, a third surface termination substitution engineering type includes imino (–NH) and vacancy functional groups. Likewise, halides-based surface engineering has also been utilized with the mediation of molten alkali metal.

Apart from chemical treatment-based surface modification, heat

treatment-based strategies have recently been utilized to fabricate ILe-MXenes by surface terminal modifications. For example, it was observed that the heat treatment of calcinating pristine $Ti_3C_2T_x$ around 600 °C resulted in a three-fold increase in its electrical conductivity [121]. Similarly, the annealing of HF etched Ti_2CT_x in N_2/H_2, N_2, Ar, and air atmosphere, in which Ti_2CT_x annealed in N_2/H_2 atmosphere, exhibited the lowermost fluorine content on its surface [94,115]. Furthermore, following the same technique, several surface-modified MXenes were fabricated by annealing the as-synthesized MXene in an ammonia atmosphere to broaden further the IL distance, which is promising for devising the gas/vapor sensors.

To conclude surface terminal substitution engineering, it was observed that the bond energies of –Cl and –Br are comparatively weaker compared to that of –OH and –F terminal bonds. Consequently, halogen terminated ILe-MXenes have the potential to act as useful platforms for additional exchange reactions. Therefore, the controlled optimization of MXenes by controlling the chemical transformation of its various surface terminals can be performed with the aid of molten Lewis basic/acidic salts or heat treatment, which results in its different physicochemical attributes. For instance, the removal of surface terminations of MXene results in its metallic nature owing to the abundance of charge carriers (free electrons) from transition metal. In contrast, the –F and –OH terminated MXenes exhibit semiconducting behavior with well-defined valence and conduction bands. Hence, the surface engineering of MXenes using a surface termination substitution approach possess the potential to optimize its optical, electrical, magnetic, thermal, mechanical and tribological performances as per the intended application. Besides, the selectivity of gas/vapor detection and monitoring in MXenes can also be achieved by smart choice and generation of its surface functionality, which is favorable for binding and interacting with the specific target analyte.

3.2.2. Surface engineering through heteroatom doping strategies in architecting high-performance ILe-MXenes

Heteroatoms doping is a proficient strategy to tune the surface electrical and chemical attributes of 2D materials such as graphene, MXenes, black phosphorus and MoS2. The doping ILe-MXenes with heteroatoms significantly improve its electrochemical performance and interlayer distance. Luo et al. [122] reported S atoms doping into Ti_3C_2-MXene layers using a simple approach that included CTAB pre-treatment, thermal diffusion through elemental S, and subsequent annealing (Fig. 11 (a)). The acquired S intercalated MXene had an anticipated interlayer modulation through the materialisation of Ti-S bonding. Similarly, Li et al. [123] reported that S-atom doping increased the interlayer distance and electrical conductivity of $Ti_3C_2T_x$ MXene. Therefore, to conclude, the high electronegativity of the S-atom leads to a reduction in the majority charge carrier (electron) density of transition metal, which results in the larger binding energy of Ti-S than Ti-C bond in Fig. 11 (b). As Lewis's acid-base interaction theory illustrates, the electron donating hosts (s-species) coordinate with valence D-orbital sites on 'M′ atom surface, resulting in robust S−Ti−C interfacial bonding and chemisorption of polysulfides onto Ti sites and –OH surface terminals. Thus, S-atom doping is a suitable dopant for augmenting the interlayer separation, ion-diffusion and charge transport in ILe-MXene. For instance, Shuvo et al. [124] reported S-doping of $Ti_3C_2T_x$ MXene by milling and mixing it with thiourea (S-atom source), subsequently giving it inert heat treatment at around 500 °C for 3 h. The outcomes exhibited a surge in the interlayer distance of the pristine $Ti_3C_2T_x$ MXene form 0.96–1.91 nm corresponding to the (002) plane upon S-atom doping Fig. 11 (c-d). It results in a higher surface-to-volume ratio of ILe-MXenes fabricated through S-doping, which is vital for designing air contaminant sensors and monitoring devices.

Moreover, Nitrogen atom (N-atom) doping of MXenes via chemical/thermal strategies has been reported to devising high-performance ILe-MXenes for diversified applications like energy storage and air remediation. Recently, N-doped ILe-MXenes have been fabricated by utilizing

various routes, and the augmentation in their interlayer distance and modulation in physicochemical properties are observed to be dependent on doping strategy [55,94]. For example, the urea carbonization technique to fabricate ILe-MXene with N-atom doping resulted in a decrease of interlayer spacing from 1.30 nm to 1.27 nm, whereas the hydrothermal treatment with urea resulted in interlayer expansion in Fig. 11 (e and f) [125]. Besides, a facile technique of utilizing saturated urea alcohol solution or monoethanolamine as liquid nitrogen source was reported to architect flexible films of N-atom doped ILe-$Ti_3C_2T_x$. It results in surge of interlayer distance from 1.15 nm to 1.24 nm, which felicitates charge carrier transport and ion-diffusion in obtained ILe-MXenes.

These outcomes are supported by experimental and theoretical results that Lu et al. reveal the N-atom doping mechanisms in Ti_3C_2 MXenes. As per DFT simulations, N-atoms were doped at three locations in carbide-MXenes, including surface terminal substitution (for –OH), surface adsorption on –O terminals and lattice substitution for carbon. These substitutions were favorable to enhancing the physiochemical attributes of ILe-MXenes for various applications, including energy storage, environmental remediation and contaminant monitoring.

3.3. Air contaminant sensing mechanism in Intercalated/delaminated and surface engineered ILe-MXenes

The sensing mechanism in intercalation/delaminated/surface engineered ILe-MXenes is primarily determined by their electrical properties, with surface functionalities coming in second. DFT calculations revealed that through interlayer engineering, the electrical nature of MXenes can be manipulated between metallic and semiconducting ranges (with band gaps ranging from 0.05 to 1.8 eV) [126]. It also reveals the dependence of the sensing mechanism of MXene towards particular air contaminants over nature of surface terminals and tested analytes. Li et al. [11], for example, discovered the presence of p-type sensing behavior in intercalated $Ti_3C_2T_x$ MXene towards reducing NH_3. When ILe-$Ti_3C_2T_x$ MXene interacted with NH3 molecules, its surface resistance increased. Concurrently, Lee et al. [83] discovered p-type sensing behavior of ILe-$Ti_3C_2T_x$ MXene toward a variety of electron-accepting/donating air contaminants such as C_2H_5OH, C_3H_6O, CH_3OH, and NH_3. It is attributed to adsorbed oxygen/water molecules that act as p-type dopants for ILe-$Ti_3C_2T_x$-MXene during the etching stage. When contaminants are exposed to ILe-$Ti_3C_2T_x$-MXene, they either adsorb or interact with active dopant sites in ILe-$Ti_3C_2T_x$-MXene.

When the pollutant molecules make contact, they are either adsorbed at the active defect sites of MXene or correlate with the surface terminals [13]. In contrast, the interaction of molecules formed by polar impurities and surface termination groups is caused by dispersion forces such as electrostatic forces, which affect resistance variation due to its decreased intermolecular force. As a result, in the extreme scenario, the pollutant molecules' adsorption at the surface has been completely projected to appear by substituting the surface elimination group with pollutant molecules. Consequently, it causes a charge transfer between the adsorbed impurity molecules and the sensing surface, resulting in a significant change in MXene's electrical resistance [4,13]. Furthermore, the essential sensing mechanism present in p-type MXene can be interpreted in terms of electron transfer from adsorbed reducing gas contaminants to Ti3C2Tx MXene, which aids in its electrical resistance.

The kind of surface termination immensely controls the transfer of electrons and further can be elaborated through the following Eqs. (8–9) [4,13]:

$$2NH_3 + 3O^- \rightarrow N_2 + 3H_2O + 3e^- \tag{8}$$

$$NH_3 + OH^- \rightarrow NH_2 + H_2O + e^- \tag{9}$$

It features outcomes in the electron's generations further outcoming the recombination of electrons and holes, which impacts the enhancement in the electrical resistance of Nb_2CT_x based MXene. In contrast,
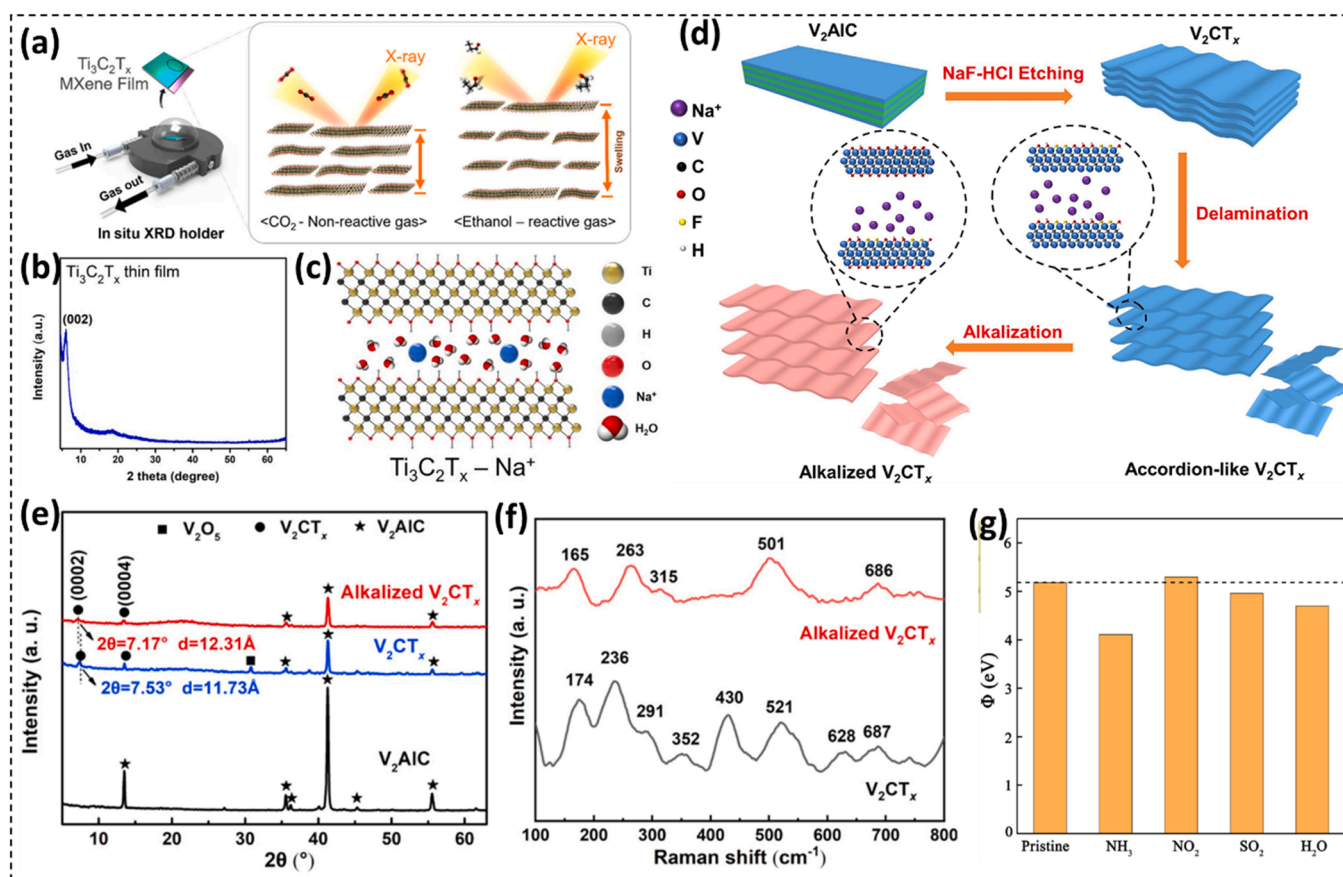
Fig. 12. (a) Schematic representation of the fabrication scheme of In-situ XRD measurements of $Ti_3C_2T_X$ films upon gas introduction [49]. (b-c) XRD pattern of $Ti_3C_2T_X$ film transferred on the SiO_2/Si wafer substrate, and schematic of the IL structure between adjacent $Ti_3C_2T_X$ MXene NSs depicting an IL space with H_2O molecules and Na^+ ions [49]. (d) Schematic of the alkalized V_2CT_X preparation [129]. (e-f) XRD and Raman spectra of the V_2CT_X and alkalized V_2CT_X [129]. (g) Calculated work functions for the pristine Hf_2CO_2 monolayer and molecule adsorbed with NH_3, NO_2, SO_2 and H_2O, respectively [130].

Wang and co-workers [127,128] notice the sensing response of Nb_2CT_X MXene against the ammonia to be of n-type environment. This group mentioned the resistance decline of harnessed Mene in an NH_3 atmosphere. Transferring charges from the adsorbed impurities molecules to prepared MXene enhances its high number of charge carrier concentrations, resulting in a loss in electrical resistance of MXene. Henceforth, the electrical nature of Nb_2CT_X MXene specifies its sensing mechanism against explicit air pollutants.

3.4. Intercalated/delaminated and surface engineered ILe-MXenes for air contamination monitoring

During ML/FL MXene fabrication, the formation of accessible interlayer space amongst the chemically bonded MXene layers provides numerous electrochemically-active sites for interaction with gas/vapor molecules in a sensing system. For air contaminant monitoring, interlayer spacing of MXenes significantly impacts the detecting performance. In general, the application of MXenes with inadequate interlayer space for air contaminant detection is limited. By modulating the interlayer space of MXene, their physicochemical attributes can be optimized, and sensing performance can be enhanced. For instance, MXene with superior interlayer distance offers a lower diffusion barrier and high accessibility. Consequently, modulation of the interlayer spacing or IL interactions of 2D MXene layers through intercalants (intercalating ions/molecules) improves the kinetics of analyte ion/molecule diffusion, which results in superior gas/vapor sensing performance. Moreover, the bonding/multi-interactions of intercalants with MXene layers provide a supportive framework for MXene structure, providing it with long-term stability.

Koh et al. [49] investigated the effect of $Ti_3C_2T_X$-MXene interlayer engineering on its air contaminant monitoring performance. They used a vacuum-mediated filtration route to create a Ti_3C_2Tx-MXene film on an anodized aluminium oxide (AAO) filter, which they then transferred to a SiO_2/Si substrate Fig. 12 (a). Afterwards, they accomplished intercalation of fabricated MXene with NaOH and dI water. It resulted in occupying the interlayer space of $Ti_3C_2T_X$-MXene by sodium ions and H_2O molecules. The interlayer distance of ILe-$Ti_3C_2T_x$ (4.3 Å) decreased by 0.84 Å on purging with nitrogen, as mentioned in Fig. 12 (b-c). Nevertheless, the interlayer distance increased on exposure to C_2H_5OH, and no impact of CO_2 purging was observed on the interlayer distance of MXene. The degree of interlayer expansion was associated with sensing performance of ILe-MXene for various air contaminants. The ILe-MXene exhibited the highest sensing response and selectivity towards C_2H_5OH than other VOCs, which is attributed to enhancing interlayer distance and modified surface functionalities.

Zhang et al. [129] utilized Na^+ ion intercalation technique to fabricate alkalized V_2CT_X for selective and sensitive monitoring of NO_2 (Fig. 12 (d)). The alkaline treatment of V_2CT_X contributed to a surge in its c-Lp and D-spacing as observed from XRD outcomes encompassing a shift of (0002) peak towards a lower angle. It is attributed to the intercalation of Na^+ ions amongst V_2CT_X layers and the surge of surface terminals (Fig. 12 (e)). The interlayer spacing in alkalized V_2CT_X was increased up to 1.23 nm, as observed from TEM and XRD analysis. Moreover, the peak around 430 cm− 1 in the V_2CT_x's Raman outcomes vanishes on alkalization, reflecting the substitution of single bond –F terminals by single bond –O terminals in ILe- V2CTx as displayed in Fig. 12 (f). This is further confirmed by EDS spectrum that there is a rise in the surface terminal oxygen-fluorine ratio ([O]/[F]) on alkalization,
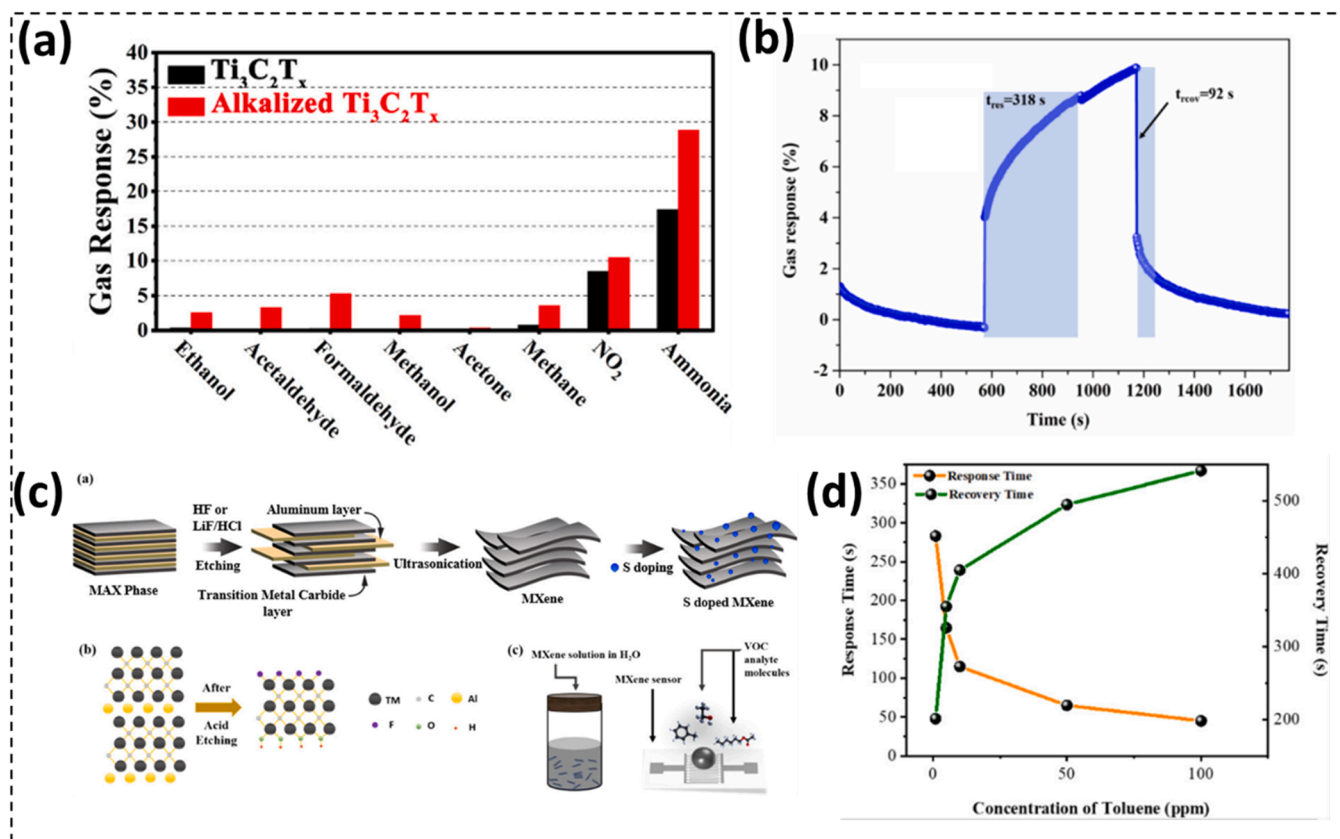
Fig. 13. (a) Response of the devices based on $Ti_3C_2T_X$ and alkalized $Ti_3C_2T_X$ to various test gases with a concentration of 100 ppm [107]. (b) the gas response and recovery of the pure $Ti_3C_2T_X$-based gas sensor at 200 °C to 100 ppm toluene gas [133]. (c-d) response peak vs concentration plots and recovery and response times vs concentration curves for the sulfur-doped $Ti_3C_2T_X$ MXene sensor [124].

which is favorable for air contaminant monitoring. The expansion of interlayer spacing and substitution of –F terminals by –O terminals through surface functionalization resulted in two-fold superior NO_2 detection performance (1.13% ppm−1) than that of pristine V_2CT_x (0.01% ppm−1) towards 5–50 ppm NO2. It is attributed to the unique electrical attributes and facile interlayer contaminant diffusion initiated from ILe-MXene's high concentration of surface terminals, expanded interlayer distance, the suitable extent of Na^+ intercalation and the manifestation of interlayer water molecules. On exposure to air, initial dehydration occurs in alkalized V_2CT_x generating sites for adsorption water-soluble contaminant molecules (NO_2). When the alkalized V_2CT_x is exposed to NO_2, the NO_2 molecules intercalate alkalized V_2CT_x layers, causing swelling. It causes a decrease in electrical conductivity of swollen alkalized V_2CT_x due to the restricted out-of-plane charge carrier transport. On flushing again with air, the adsorbed NO_2 molecules leave the alkalized V_2CT_x resulting in a surge of its electrical conductivity. Thus, the sensing mechanism in ILe-MXenes is governed by intercalation and surface functionalization engineering, which results in improved sensing response due to increased specific surface area, modified surface chemistry, and tuned electrical conductivity.

Furthermore, Wang et al. [130] discovered that the presence of water molecules on the surface of Hf_2CO_2 increases its selective sensitivity to NH_3. The as-prepared material recorded a decrease in the work function (WF) caused by the ammonia molecules adhering to the manufactured Hf_2CO_2, along with a change in WF of 1.07 eV relative to the bare Hf_2CO_2, or 5.18 eV. Whereas the H_2O based molecular adsorbing increases the intermediated reduction in WF by about 0.49 eV, which was larger than the slight decline in WF (0.22 eV) induced by adsorbing SO_2, respectively. In contrast, the WF is slightly increased by the adsorption of an electron-acceptor NO_2 molecule by about 0.12 eV compared to pure Hf_2CO_2. At the same time, the decrease in work function is well synchronized with the charge transfer from the electron-donor molecules, NH_3, SO_2, and H_2O, to the substrate. Overall, a significant decrease in work function and a sharp increase in currents under applied voltage give monolayer Hf_2CO_2 a high sensitivity to NH_3 molecules (Fig. 12 (g)).

Hajian et al. [131] theoretically investigated the effect of -F terminal group variation on the $Ti_3C_2T_X$-MXene surface on its NH_3 sensing behaviour. First, they tested $Ti_3C_2T_X$-MXene for two different -F ratios, $Ti_3C_2(OH)0.44 F_{0.88}O_{0.66}$ and $Ti_3C_2(OH)_{0.66}F_{0.22}O_{0.11}$, and found that lower -F concentrations containing MXene performed better in terms of NH_3 adsorption. It is due to less charge carrier transfer from -F to NH3 molecules than at other surface terminals. Yang et al. [107] conducted an experimental evaluation in which an increase in surface O/F ratio and intercalation due to sodium ions was reported to improve the monitoring performance of $Ti_3C_2T_X$. They discovered that alkali-ion intercalated-MXene with an optimised O/F ratio surface had a two-fold enhanced sensing response towards 100 ppm of NH_3 than pristine $Ti_3C_2T_X$-MXene (Fig. 13 (a)). Furthermore, Khaledialidusti et al. [132] predicted that improving the surface oxygen-fluorine during the architecting of double transition metal MXenes improves their sensing performance. Finally, they tested surface-modified $Mo_2TiC_2T_X$-MXene for CO_2 capture/detection and discovered that specific functional terminals modified $Mo_2TiC_2T_X$-MXene outperform pristine MXene due to defect generation.

Wang et al. [133] reported the N-doped MXene for the acetone gas detection occurred at high temperatures. The presented N-atom acted as heterogenous into MXene NSs and exhibits some cracks found around the doped N-atom, which helps to enhance the adsorption capacity and surface hydrophilicity of MXene NSs. The N-doped MXene attains excellent gas sensing performance by showing response and recovery time of 381 s/92 s, respectively (Fig. 13 (b)).

Table 2
State-of-the-art ILe-MXene chemiresistors fabricated through intercalation, delamination, doping and surface engineering.

Sensing Element	Gaseous Contaminant/ analyte	Preparation Method	D-lattice parameter spacing / Purity (%) /lattice fringe spacing	Concentration	Sensitivity	LDL/ LOD	Recovery/Response Time
Metallic $Ti_3C_2T_x$ MXene[85]	Acetone NO$_2$ SO$_2$ CO$_2$	Experiemental fabrication though metallic channel	-	100 ppm	0.97, 1.7, 0.8, 0.88%	50–100 ppb	NR
single-/few-layer 2D V_2CT_x[83]	Acetone H$_2$S	chemiresistive mechanism	~5.82° - 4.06 Å	200 ppm 100 ppm	25 5	2 ppm for hydrogen	7 min/2 min for hydrogen
2D $Ti_3C_2T_x$ (MXene)[83]	ethanol methanol acetone ammonia	Delamination + ultrasonication	Low angle indication of D-spacing	25–200 ppm	0.115 0.143 0.075 0.21	9.27 ppm	NR
Alkalized organ-likeMXene [107]	NH$_3$ NO$_2$ CH$_4$	Dip coating	0.323 nm	100 ppm 100 ppm 1%	28.87 10 4	NR	NR
Alkalized V_2CT_x [129]	NO$_2$	Alkalization _+ mild etching	0.28 and 0.31 nm	5 ppm	10	5 ppm	120 s
Hf$_2$CS$_2$ Hf$_2$CO$_2$[134]	NH$_3$, NO, NO, CH$_4$, H$_2$S, O$_2$, H$_2$O, CO$_2$, N$_2$	-	a = b = 3.47 Å and c= 2.41 Å a = b = 3.28 and c= 2.35 Å	NR	15% and 121% (without strain)	NR	NR
Mo$_2$CT$_x$[135]	NH$_3$ NO$_2$	TMA intercalation	12.5 Å	5 ppm 5 ppm	1.95% 16.98%	NR	60 s/58 s 474 s/354 s 732 s/214 s
$Ti_3C_2T_x$ MXene [136]	Ethanol	Spray coating	12.5–16.0 Å	5–120 ppm	2.1 − 14.1%	NR	NR
accordion-like $Ti_3C_2T_x$[137]	Acetone	HF-etching	200 nm	0.25 ppm	17.30%	250 ppb	120 s/53 s
TbC$_2$T$_x$[131]	NH$_3$ SO$_2$ H$_2$S NO CO$_2$	Exfoliation	(D$_{gas\ substrate}$) in Å 2.54 3.07 2.32 2.18 2.75	NR	NR	NR	NR
W$_2$CT$_2$[138]	NH$_3$	DFT	a = 2.86 Å ~ 1.8/1.2 Å (F/O atom distance)	NR	NR	NR	77.37 ns (charge transfer) and 40.08 ns (recovery time)
V$_4$C$_3$T$_x$	acetone	Selective etching	22.75–29.23 Å	1–100 ppm	90%	1 ppm	40 s
N-doped MXene [133]	acetone	sacrifice template method	-	NR	36	NR	92/381 s
Nb$_2$CT$_x$-CTAB [139]	NO$_2$	Intercalation + delamination	13.1 Å	50.23%[1]	25 ppm	21 ppb	NR
Nb$_2$CT$_x$[139]	NO$_2$	Intercalation + delamination	-	16.01%	25 ppm	67 ppb	78.9 s/ 46.5
Nb$_2$CT$_x$-0.2 APTES[139]	NO$_2$	Etching	12.59 Å	31.52%	5–25 ppm	3 ppb	NR
Nb$_2$CT$_x$[140]	NO$_2$	etching	12.52 Å	12.5%	5–25 ppm	15 ppb	NR
S-doped MXene [124]	Toluene	Etching _ ultrasonication	0.96 nm	59.10 42.10 11.90	10 ppm 5 ppm 1 ppm	500 ppb	NR
Ti_3C_2Tx[141]	ethanol	Delamination	1.21 nm	700	100 ppm	NR	8.2 min/15.6 min

Shuvo et al. [124] reported a VOC sensor where pristine and S-doped materials were fabricated and applied as the electrode material and evaluated for several VOCs such as hexyl-acetate, hexane, ethanol and toluene, respectively. The as-prepared S-doped material demonstrates that the response peaks' absolute values vary with the toluene concentration for both S-doped and unaltered MXene sensors. For each concentration of the analyte, five sensors with both doped and undoped $Ti_3C_2T_x$ MXenes were tested, and as can be seen in the figure, each sensor had a stable signal response. As a result of the abundance of adsorption sites at lower VOC concentrations, the charge transfer can occur in a concentration-dependent manner. Whereas the slopes of both curves decrease as the point of saturation is approached at higher VOC

concentrations, as highlighted in Fig. 13 (c-d).

A summary of intercalated, delaminated, doped and surface engineered ILe-MXenes have tabulated in Table 2, which illustrates the state-of-the-art ILe-MXene sensing performance with essential sensing parameters in terms of interlayer spacing. Hence, the intercalation, delamination, surface modification and doping engineering enhance the interlayer separation of MXenes resulting in greater sensing performance (Table 2).
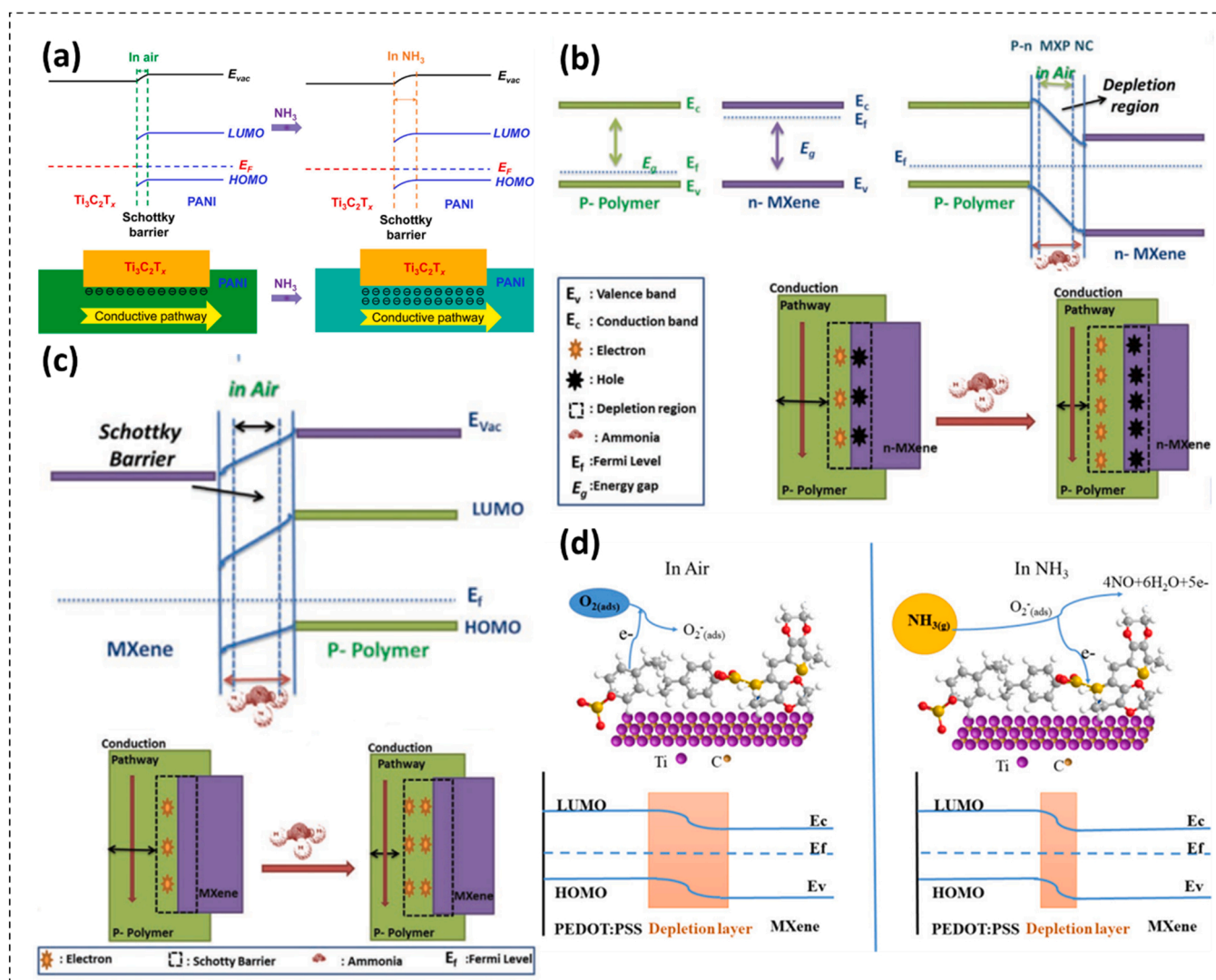
Fig. 14. (a) Energy level alignments and conductivity pathway of the hybrid PANI/Ti$_3$C$_2$T$_X$ sensitive films before and after NH$_3$ molecules absorption [11]. (b) Sensing mechanism in p–p type and p–n type semiconducting ILe-MXenes hybrids [13]. (c) Chemisorption of NH$_3$ over PEDOT:PSS-MXene hybrids [13]. (d) NH$_3$-Sensing Mechanism of the PEDOT:PSS/MXene Sensor [143].

3.5. Challenges associated with interfacial and surface engineering strategies to engineer of ILe-MXenes and their application in air contamination sensing and monitoring

In conclusion, the fundamental and in-depth investigation of the literature shows that surface engineering can be performed by either substituting reaction for replacing MXene surface terminals or by heteroatom doping as per targeted applications. These strategies serve dual purpose of modulating IL spacing of MXene sheets and regulating the physicochemical features of MXenes, including surface chemistry, electrical and optical attributes, morphology, topology and mechanical stability [55,115]. Furthermore, it enhances the fundamental attributes of ILe-MXenes, such as charge carrier transport, ion diffusion and chemical interactions, which are essential in devising high-performance MXenes for various applications. However, despite great efforts dedicated to surface engineering of ILe-MXenes, several critical challenges must be addressed. These challenges include exploring the fundamental role of heteroatom doping in increasing the MXene performance for various applications such as gas sensing and electrochemical storage and task settings required to control the type of surface terminals for selective and precise application [55,115]. Moreover, surface modification can modify the electron-donor capability of MXenes, surface chemistry

and electrical attributes like charge conduction, wettability, ionic interaction and adsorption. Therefore, theoretical evaluations must be emphasised to understand the mechanism of interaction of heteroatom doping in MXenes and its impact on various fundamental attributes of ILe-MXenes. Moreover, emphasis must be given to exploring scalable, safe and controllable surface engineering techniques for architecting ILe-MXenes with intended applications.

4. Hybridization and heterostructure engineering to architect ILe-MXenes for air contaminant monitoring and detection

As discussed, intercalation and surface engineering prevent restacking of MXenes layer and modify its physicochemical attributes for intended applications. However, mutli-step process, controllable optimization and machine processing, achieving mechanical flexibility and safe/scalable manufacturing limit their utilization in various applications. The most prominent way to address most of these challenges in single-step processing includes hybridization and heterostructure engineering of MXenes with other materials [4,13,48]. Other organic, inorganic or both materials can be introduced amongst the MXenes layers either as filler or by architecting hybrids/composites, which prevents restacking, modulates interlayer space, and alters its chemistry
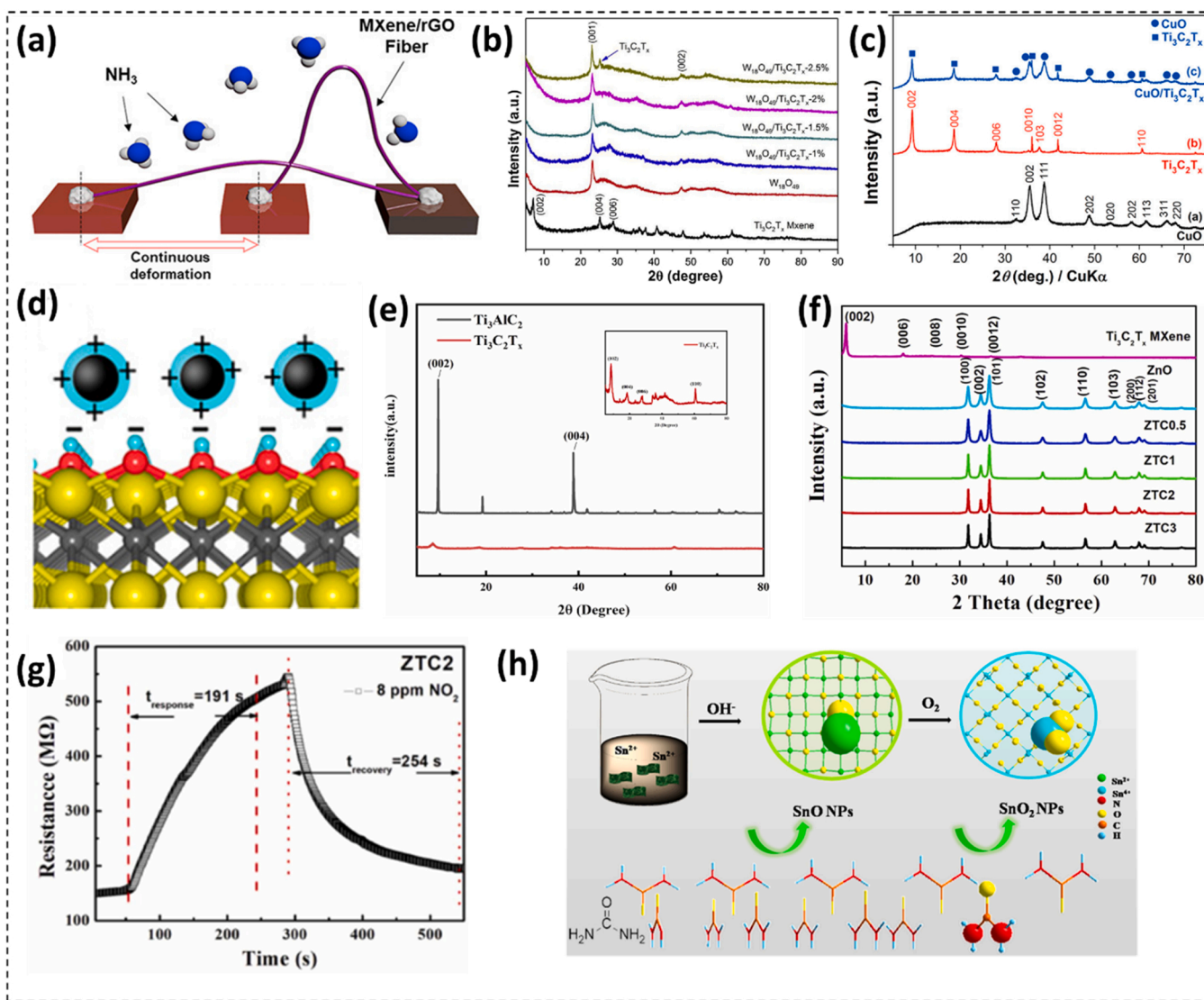
Fig. 15. (a) Schematic illustration of the MXene/RGO for ammonia gas sensing [148]. (b) XRD spectra of $Ti_3C_2T_x$ sheets, $W_{18}O_{49}$ NRs, and $W_{18}O_{49}$/Mxene composites [149]. (c) XRD pattern of CuO nanoparticles, $Ti_3C_2T_x$ after etching by HF and CuO/$Ti_3C_2T_x$ [150]. (d) Representation of electrostatic interaction of CuO/$Ti_3C_2T_x$ [150]. (e) XRD pattern of designed MXene for gas sensing [151]. (f-g) XRD graph of the $Ti_3C_2T_x$, pure ZnO and ZnO/$Ti_3C_2T_X$ nanocomposites with different amounts of $Ti_3C_2T_x$, and the recovery and response curve to 10 ppm NO_2 at different temperatures [152]. (h) Schematic illustration of chemical reactions during the preparation of SnO-SnO_2/$Ti_3C_2T_X$ nanocomposites [153].

and surface properties. Besides, heterostructures address the issue of structure breakage caused due to volume expansion during analyte/ion adsorption during sensing applications. Thus, hybridization alone can cater to multi-issues related ILe-MXenes and is an efficient route for architecting ILe-MXenes with desired properties for intended applications.

4.1. Air contaminant sensing mechanism in ILe-MXenes engineered through hybridization/heterostructure engineering

Numerous reports in the literature credit the formation of various heterointerfaces between the precursors, revealing the sensing mechanism in inorganic-organic nanocomposite systems [13,142]. As a result, the sensing mechanism of ILe-MXenes hybrids depends on the type of heterointerfaces that form between the precursors, such as p-p or p-n junctions. It also depends on the nature of the precursors and how heterojunctions behave. Similarly, it has been found that MXenes' electrical properties can vary from metallic to semiconducting depending on the type of "M" element, "X" type, and surface functional groups. In addition,

the presence of polymers in MXene results in the semiconducting nature of ILe-MXenes hybrids. However, the nature and stochiometry of their precursors control the change in the electrical nature of ILe-MXenes hybrids. As a result, the air contaminant sensing mechanism in ILe-MXenes hybrids is primarily controlled by the type of heterointerface (p-n or p-p) among its precursors, with weak chemical interactions acting as a secondary control [4,13]. As a result, all types of ILe-MXenes hybrids frequently exhibit these chemical interactions, such as hydrogen bonding, chemisorption, and forming distinct heterointerfaces. In addition, the net air contaminant sensing phenomenon in ILe-MXenes hybrids is caused by four key interactions.

4.1.1. Primary sensing phenomena in ILe-MXenes hybrids

The physisorption of air contaminant molecules controls the sensing behaviour of ILe-MXenes hybrids over the hybrid surface. However, the electrical nature of MXene and precursor influences their sensing behaviour in relation to specific air contaminants. As a result, the electrical resistance of ILe-MXenes hybrids varies depending on the type of contamination (oxidising or reducing), the predominance of either of

precursors, and the type of heterojunctions formed between them (p-n or p-p type) [4,13]. Moreover, as an illustration, it has been discovered that the presence of NH_3 causes the electrical resistance of $Ti_3C_2T_x$/PEDOT: PSS hybrid to decline, respectively [143]. This is because it causes a reduction in hybrid's net electrical resistance by causing a direct charge carrier transportation between hybrid and NH_3. The report, however, is not backed up by any experimental data.

Li et al. [11], on the other hand, discovered a surge in the electrical resistance of PAN/$Ti_3C_2T_x$ hybrids in an NH_3 environment, which they attribute to PAN dominance over $Ti_3C_2T_x$ and the presence of Schottky-type heterojunctions between them. Because the work function of p-type PAN was slightly larger than that of p-type $Ti_3C_2T_x$, miniature Schottky junctions formed at the precursor's interfaces, it causes a hole depletion region to form in PAN. When the hole depletion layer interacts with electron-donating NH_3, its width decreases, resulting in narrower conducting channels for charge carriers to transport through the PAN during the sensing process. It increases the net electrical resistance of hybrid when it interacts with the NH_3 molecules shown in Fig. 14 (a). Zhao et al. [38] found similar results for a $Ti_3C_2T_x$/CPAM-based NH3 chemiresistor. As a result, synergistic effects caused by the formation of Schottky heterojunctions and the dominance of either of the precursors determine the sensing phenomenon for p-p type semiconducting ILe-MXenes hybrids (Fig. 14 (b)). As a result, the presence of either of the precursors in ILe-MXenes hybrids, as well as their concentration and the nature of contaminant molecules, determine its sensing mechanism.

Wang et al. [127,128] found that p-type PAN precursor outperformed n-type Nb_2CT_x-MXene during NH_3 monitoring using p-n semiconducting ILe-MXenes hybrids. It was hypothesised that p-n heterojunctions would form at the MXene-PAN interface, forming barrier layers between them. When PAN interacts with NH_3, the hole concentration decreases, resulting in an increase in the width of the depletion region towards the PAN side, which increases HNC resistance in an NH_3 environment. A similar sensing mechanism exists for various p-n type semiconducting organic-inorganic ILe-MXenes hybrids [144] (Fig. 14 (c)). As a result, the sensing mechanism of ILe-MXenes hybrids is determined by the predominance of either of the precursors, their concentration, and the nature of contaminant molecules.

Zhou et al. [51] reported similar results for CO_2 detection using ternary hybrid of polyethyleneimine (PEI), nitrogen-doped $Ti_3C_2T_x$-MXene (N-MXene), and rGO. In such ternary ILe-MXenes hybrids, all three precursors play an important role in the sensing mechanism. The precise nature of sensing phenomena is determined by the dominance of one of the precursors. Their studies found that PEI dominates the sensing mechanism. N-MXene and rGO played important roles during the sensing process due to their hydrophilic nature and excellent conductivity. Nonetheless, MXene is observed to dominate in detecting VOCs in ILe-MXenes hybrids, which identifies the nature of the sensing mechanism.

4.1.2. Secondary sensing phenomenon in MXene-Polymer HNCs

4.1.2.1. Chemisorption.
The most common sensing mechanism observed in various materials, including metal oxides, is the adsorption of ambient oxygen molecule [144]. The p-type semiconducting ILe-MXenes hybrids surface converts ambient oxygen molecules into oxygen radicals while adsorbing them by trapping electrons in the conduction band of the HNCs [13]. It causes the formation of an electron depletion region with high electrical resistance between the precursors. Trapped electrons are rereleased into the HNC's conduction band upon interaction with adsorbed reducing contaminant molecules like NH_3. It causes a change in the space charge region of the conduction band of the HNC, lowering its electrical resistance. Similar findings were reported by Jin et al. [143] for $Ti_3C_2T_x$/PEDOT: PSS HNC for monitoring NH_3 (Fig. 15 (d)), and they also provided a summary of the entire chemisorption process.

$$O_2 + e^- \rightarrow O_2^- \tag{10}$$

$$4NH_3 + 5 O_2^- \rightarrow 4NO + 5e^- + 6 H_2O \tag{11}$$

At room temperature, however, there is insufficient chemisorption because there is a much lower rate of oxygen molecule to oxygen radical conversion. As a result, at room temperature, chemisorption plays a trivial part in the net sensing phenomenon.

4.1.2.2. Formation of hydrogen bonds and unique heterointerfacial functional groups.
Several theoretical and experimental findings have predicted the formation of intermolecular hydrogen bonds and distinctive heterointerfacial functional groups among precursors during the synthesis of ILe-MXenes hybrids [13,81,145]. The electric nature of MXene changes from conducting to semiconducting when specific heterointerfacial functional terminals are present over the hybrid surface. In addition, it has been claimed that these special functionalities facilitate interfacial charge transfer when interacting with contaminant molecules, improving the effectiveness of hybrids as monitoring devices.

Due to the involvement of surface functionalities, Kim et al. [85] reported the sensing mechanism in ILe-MXenes hybrids for monitoring various VOCs and explained how the devices could form hydrogen bonds and detect different VOCs. However, according to Yuan et al. [146], regardless of the type of VOCs used, ILe-MXenes hybrids resistance rises in the presence of all of them. This is believed to be because of MXene's dominance in ILe-MXenes hybrids and its superior conductivity. In addition, Yuan et al. [146] suggested that ILe-MXenes hybrids have a selectivity mechanism for VOCs by their ability to form hydrogen bonds with extra electronegative atoms like O_2 atoms and their electrostatic interactions with MXene. As a result, ILe-MXenes hybrids are effective at detecting VOCs like alcohol and ketones. However, using a similar sensing mechanism to control the polar VOCs and non-polar VOCs with low hydrogen-bonding capacities turn challenging.

4.2. MXene-Inorganic hybridization/heterostructure engineering to architect high-performance ILe-MXenes for air contamination sensing and monitoring

Inorganic materials, including carbon nanomaterials and metal-based materials, are the suggested materials as spacers to optimize the IL structure in MXenes due to their high chemical stability and tunable band gap from metallic to insulating range [147]. The insertion of inorganic materials amongst the layers of MXenes results in ILe-MXenes with enhanced interlayer separation, high specific surface area, robust mechanical strength due to chemical bonding, large porosity, abundant surface chemistry and synergistic effects due to host-guest chemistry, which is highly favorable for air contamination monitoring.

Lee et al. [148] reported MXene with rGO hybrid to monitor several air contaminants, including H_2S, NH_3, C_2H_5OH, SO_2, C_6H_6, and xylene. However, the sensing response of MXene/rGO hybrid towards NH_3 was excellent compared to that of pristine precursor-contain sensors, as illustrated in Fig. 15 (a). The purification and functionalization of rGO and processability with MXene are tedious and require sophisticated means. Furthermore, Sun et al. [149] investigated the air contaminant detection performance of the $W_{18}O_{49}/Ti_3C_2T_x$ hybrid. The hybrid exhibited excellent and selective sensing response towards low concentrations of C_3H_6O. Yet, due to the -F surface functionalities, the response was inadequate at a larger concentration of C_3H_6O using $W_{18}O_{49}$ precursors. In addition, the XRD pattern in Fig. 15 (b) indicated that the peak sharpness occurs at 6.2° related to peak (002) of MXene together with the D-spacing of 14.3 Å. Hermawan et al. [150] proposed the CuO/ $Ti_3C_2T_x$ hybrid to monitor very low trace of C_7H_8 efficiently. The operation temperature for CuO/ $Ti_3C_2T_x$ hybrid to monitor C_7H_8 was optimized at 250 °C, which surges the sensor's cost and energy demands, limiting its commercial viability. The XRD pattern in Fig. 15 (c) exhibits the MXene peak appeared at (002) plane, which is related to

Table 3
State-of-the-art ILe-MXene prepared from inorganic hybridization for air contaminant monitoring.

Sensing Element	Gaseous Contaminant	Preparation Method	D-lattice parameter spacing / Purity (%) /lattice fringe spacing	Concentration	Sensitivity	LDL/ LOD	Recovery/ Response Time
RGO/$Ti_3C_2T_x$[154]	NH_3	Wet spinning	-	50 ppm	6.8	NR	NR
CuO/$Ti_3C_2T_x$[150]	Toluene	Electrostatic self-assembly	0.268 and 0.256 nm	50 ppm	7	NR	10 s to 50 ppm toluene
$Ti_3C_2T_x$/SnO[155]	NH_3	Hydrothermal method	78.7 nm and 2.6 Å	10 ppm	7.8	1 ppm	61 s and 119 s
$Ti_3C_2T_x$/WSe$_2$[44]	Ethanol	Solution method	-	1 − 40 ppm	0.5 − 9.2	NR	9.7/6.6 s
ZnO/$Ti_3C_2T_x$[152]	Acetone	Hydrothermal method	1.42 nm	100 ppm	14.4	NR	8 s/ 12 s
$W_{18}O_{49}$/$Ti_3C_2T_x$[149]	NH_3	Acid etching + solvothermal route	14.3 Å	20 ppm	2	NR	NR
αFe$_2$O$_3$/Ti_3C_2Tx[156]	NH_3	Hydrothermal method	0.25 nm	5 ppm	18.3	5 ppm	2.5 s
SnO_2/$Ti_3C_2T_x$[157]	NH_3	Hydrothermal method	-	50 ppm	0.40	500 ppb	36 s/44 s
MXene/TiO_2[158]	NH_3	Spraying method	-	10 ppm	3.1	0.5 ppm	60 s/750 s
WO_3/$Ti_3C_2T_x$[159]	NH_3	ultrasonication	0.264 nm and 0.376 nm	1 ppm	1.23	1000 ppb	119 s/228 s
SnO_2/MXene heterostructure[160]	NO_2	Hydrothermal method	46 nm	30 ppb	2.31	NR	146 s/102 s
MXene/In_2O_3[161]	NH_3	Hydrothermal method	a=b=c= 10.118 Å.	20 ppm	0.36 and 1.007	NR	Less than 2 s
α-Fe$_2$O$_3$/$Ti_3C_2T_x$[156]	Acetone	Hydrothermal method	0.361 nm and 0.261 nm	5 ppm	0.166	NR	5 s/5 s
Au- $Ti_3C_2T_x$[162]	NH_3	Solution Mixing method	13.4–16.0 Å	1 ppm	NR	92 ppb	NR
Ti_3C_2/TiO_2[163]	NO_2	hydrothermal oxidation	0.23 and 0.25 nm	5 ppm	1.13	NR	(2 and 3.8 times

the ILE distance not shifted towards the higher or lower angle and representing the no expansion response over the ILE spacing of MXene whereas, CuO NPs implanted in amongst the vacant space of delaminated sheets and comprises of various layers respectively. In addition, the sample attained the lattice fringe spacing of 0.268 and 0.256 nm for both CuO and MXene, which could be ascribed to the plane (110) for CuO and MXene as mentioned in Fig. 15 (d), respectively.

Similarly, Zhu et al. [151] reported the ZnO/$Ti_3C_2T_X$ fabricated through the hydrothermal process in which ZnO was dispersed on MXene and implemented for the gas sensing mechanism. The XRD pattern in Fig. 15 (e) illustrating the corresponding peaks appeared at 6.3° for (002) peak plane and attained the D-spacing of 1.42 nm, respectively. After sensing evaluation, the material exhibits recovery and response times of 8 and 12 s at a concentration of 100 ppm, respectively.

In another report, Liu et al. [152] applied the same methodology for the ZnO/MXene nanomaterials for NO_2 detection. The as synthesized material through XRD characterization in Fig. 15 (f) demonstrates the appearance of (001) peaks and basal face. Whereas the peaks appeared a (002) exhibits the interplanar spacing of 14.58 Å centered at the 6.07°. Moreover, the same material during NO_2 (8 ppm) detection achieved recovery and response times of 254 and 191 s, as elaborated in Fig. 15 (g), respectively. Wang et al. [153] reported the fabrication of SnO-SnO2 with MXene for the acetone-based gas sensor, as displayed in Fig. 15 (h).

The as-prepared material harnessed through hydrothermal method attained the gas sensing response of (Rg/Ra=12.1), which was closely 11 and 4 times greater than the pristine SnO-SnO2 and MXene accordingly. Similarly, same sample possessed excellent reproducibility along with a recovery and response time of 9 and 18 s at the concentration of 100 ppm. The state-of-the-art MXene-inorganic hybrids are summarized in Table 3.

There are significant sensing performances associated to ILe-MXenes fabricated by inorganic hybridization as evident from Table 3. However, the bottlenecks of high-temperature operation, sulphur poisoning, complex processing, associated toxicity, and rigidity impede the practical development of MXene-Inorganic hybrids and open the door to developing MXene-abundant organic molecule hybrids.

4.3. MXene-organic hybridization/heterostructure engineering to architect high-performance ILe-MXenes for air contamination sensing and monitoring

The practical viability of experimentally reported pristine MXene-based and its inorganic hybrids-based sensors possessed common bottlenecks, with low flexibility, slow recovery and oxidation because of their greater affinity for polar air pollutants [13]. These were partially catered by surface engineering and intercalation/delamination engineering. For instance, by its functionalization, surface engineering can cater to issues of oxidation, and intercalating MXene layers can provide structural stability. Moreover, the fabrication of MXene-inorganic hybrids can cater to both issues, i.e. ambient stability and structural stability and results in enhanced physicochemical features. However, fabricating MXene-organic hybrids can cater to majority of these issues, as integration of organic materials such as macromolecules averts the layer restacking, modify surface functionality, tune physicochemical attributes and provides mechanical flexibility for devising flexible sensors [164]. Besides, the interaction of organic materials with MXene's surface functionalities by multi-interactions provides stability in varying environmental conditions and tunes opto-electronic band gaps. Additionally, the generation of interfacial heterojunctions between organic materials and MXenes increases the sensitivity and recovery time owing to synergistic effects.

There are numerous reports in the literature on synthesizing MXene-organic hybrids with various hydrophilic (silicones, PE, PS, PVA, PI) and conducting (PAN, PEDOT, PVP, PSS, PPy, PAP) organic materials [13, 164–166]. The research has been dedicated to augmenting the physicochemical attributes evolving from organic-inorganic interfaces in hybrids by molecular and supra-molecular dynamics [4,54]. Moreover, numerous reports based on MD and DFT evaluations have exhibited that the MXenes have a larger affinity for organic materials to make hybrids owing to their abundant surface chemistry [13,164–166]. The surface terminals on interaction with MXenes lead to multi-interactions, including electrostatic, covalent, or hydrogen bonding, which results in stable MXene-organic hybrids in a variable environment [165,167]. Furthermore, captivating merits of organic materials like abundance, easy processability, lower toxicity, biocompatibility, mechanical flexibility, controllable bad gap and low cost, the MXene-organic hybrids result in high performance for air contaminant monitoring.
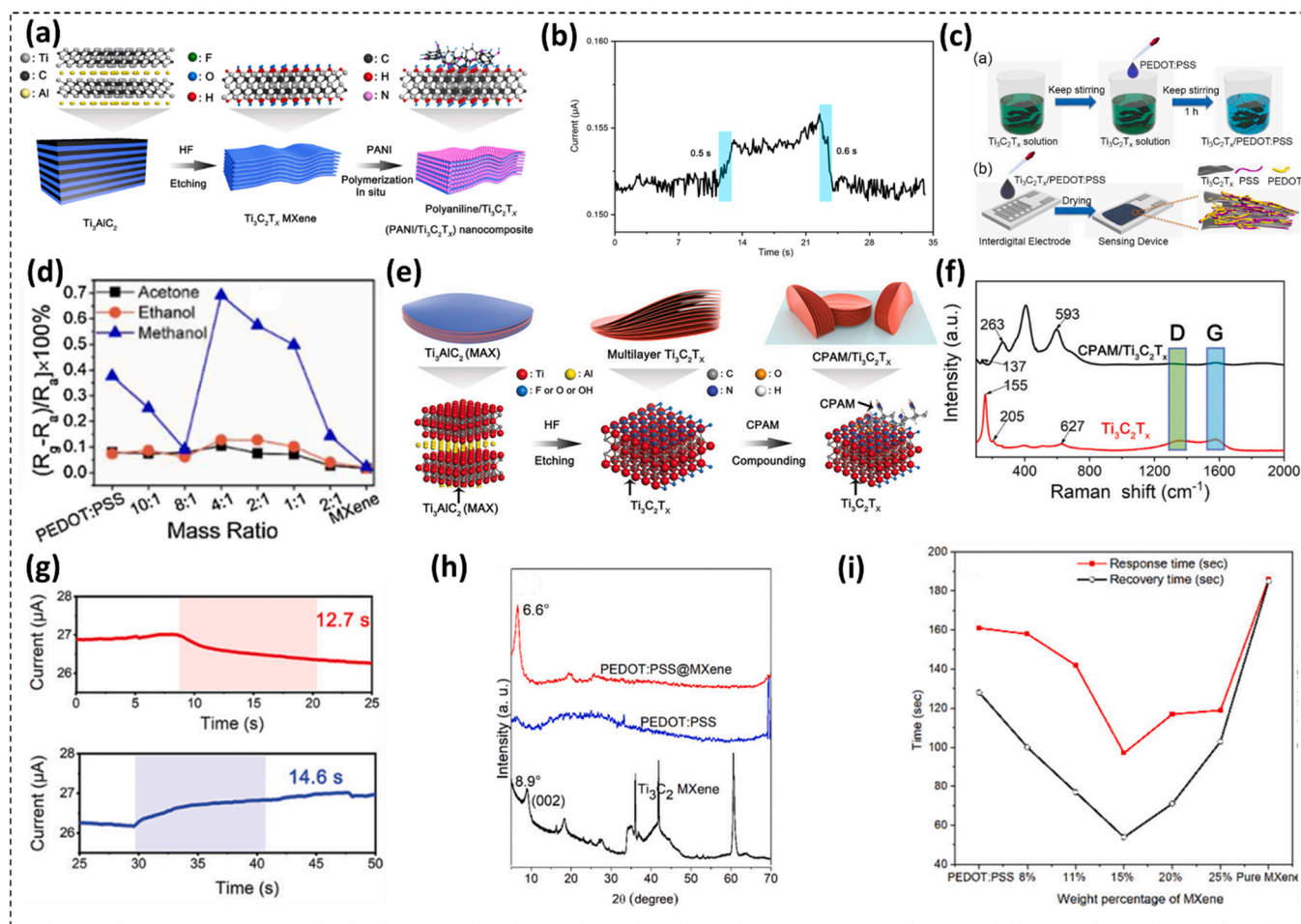
Fig. 16. (a-b) Schematic illustration of the MXene/PANI fabrication and response anad recovery time curve of PANI/Ti$_3$C$_2$T$_X$-based flexible sensors to 1 ppm ethanol gases [168]. (c-d) Schematic representation of the fabrication route of MXene/PEDOT: PSS and sensing responses of the sensors toward 300 ppm acetone, ethanol and methanol at ambient temperature [169]. (e) Synthesis process of CPAM/Ti$_3$C$_2$T$_x$ nanocomposites. [38]. (f-g) Raman representation of CPAM/Ti$_3$C$_2$T$_x$ nanocomposites and Recovery and response time of CPAM/Ti$_3$C$_2$T$_X$. [38]. (h-i) Raman characterization of the prepared PEDOT: PSS, Ti$_3$C$_2$T$_x$ MXene, and PEDOT: PSS/MXene composites. and response and recovery time [143].

For instance, Zhao et al. [168] reported a very low temperature (0–5 °C) fabricated Ti$_3$C$_2$T$_X$-PAN hybrid and deposited it over PET substrate for monitoring several VOCs at room temperature. Incorporating PAN into MXene resulted in a fine accordion-like morphology felicitating rapid VOC diffusion due to the creation of mass-transport pathways, which resulted in rapid VOC detection. The sensor exhibited excellent sensing response (1.56% at 1 ppm), high selectivity (~20% for 200 ppm of CH$_3$OH, C$_3$H$_6$O, and NH$_3$), good repeatability (140 exposure cycles), prompt response and recovery (~0.5 s), significant linear detection range (1–200 ppm) and high flexibility (in bend angles 0–120°) towards low traces of C$_2$H$_5$OH at room temperature. DFT outcomes supported these experimental findings in terms of adsorption energies of various contaminants over hybrid surface and their bond length on surface encompassing O-terminated Ti$_3$C$_2$T$_X$, F-terminated Ti$_3$C$_2$T$_X$ and OH-terminated Ti$_3$C$_2$T$_X$, accordingly. The highest binding energy and smallest bond length towards C$_2$H$_5$OH were observed for OH-terminated Ti$_3$C$_2$T$_X$ than further terminated MXenes and bare precursors. Despite excellent sensing features, the study lacks to evaluate long-term stability and efficiency of sensor in the variable environment, which is necessary for its practical applications **(Fig. 16 (a-b)).**

The sensing behaviors in MXene-organic hybrids are also dependent on synthesis strategy. To explore this, Wang et al. [169] harnessed a Ti$_3$C$_2$T$_X$/PEDOT:PSS hybrid using ex-situ route for selective CH$_3$OH monitoring Fig. 16 (c). Moreover, the impact of variation in precursor nature and concentration (changing the PEDOT:PSS/Ti$_3$C$_2$T$_X$ mass ratio

as precisely of 10:1,8:1,4:1, 2:1,1:1and1:2) on VOC sensing performance of hybrid was evaluated. The sensor encompassing 4:1 mass ratio demonstrated the highest sensing response towards 300 ppm of tested VOCs, as shown in Fig. 16 (d). The dependence of sensing response over precursor concentration was ascribed to variation in sensing mechanism due to the predominance of specific precursors. Similarly, bare PEDOT: PSS followed a typical p-type sensing mechanism, which is prominent in macromolecules due to diffusion, charge transfer, and swelling, reducing its conductivity in a contaminant environment. A similar mechanism was observed in hybrids with mass ratios 10:1 and 8:1 due to dominance of PEDOT:PSS precursors. Nevertheless, the sensing response of 10:1 and 8:1 hybrids was significantly lesser than that of the pristine PEDOT:PSS, which is attributed to the integration of MXene causing lesser swelling of the PEDOT:PSS matrix. Based on the dominance pattern of precursors, three charge transport pathways in hybrids, including MXene-MXene, polymer-MXene and polymer-polymer trials, were proposed to contribute towards sensing phenomena. Besides, 4:1 hybrid exhibited the highest sensing response, ascribed to the presence of PEDOT:PSS amongst MXene layers, breaking MXene-MXene pathways. However, in other hybrids with a dominance of MXene concentration (2:1, 1:1, 1:2), the MXene-MXene pathways were primarily dominant, resulting in resistance decline leading to reduced sensitivity.

The evaluation of sensing behavior of MXene-organic hybrids is not limited to VOCs but also extended to other air contaminants. For instance, Zhao et al. [38] explored the NH$_3$ detection performance of

Table 4

State-of-the-art ILe-MXene-Organic hybrid based air contamination monitoring and detection.

Sensing Elements	Gaseous Contaminant	Preparation Method	Sensitivity Response	Concentration	LDL/ LOD	Recovery/ Response Time
$Ti_3C_2T_X$/PEDOT:PSS(4:1)[169]	CH_3OH	Solution method	0.4%	180 ppm	180 ppm	250 s/500 s
	C_2H_5OH		0.1%	300 ppm	60 ppm	250 s/500 s
	C_3H_6O		0.09%	300 ppm	NR	250 s/500 s
$Ti_3C_2T_X$- PANIsensor[168]	C_2H_5OH	In-situ polymerization	1.56%	1 ppm	1 ppm	0.4 s/0.5 s
PEDOT:PSS/$Ti_3C_2T_X$[143]	C_7H_8	Dip-coating technique	1.2%	100 ppm	NR	NR
	CH_3OH		14%	100 ppm	NR	NR
	CH_3OH		4.6%	100 ppm	NR	NR
	C_3H_6O		3.4%	100 ppm	NR	NR
PANI/$Ti_3C_2T_X$[11]	HCHO	In-situ self assembly	0.2%	25 ppm	NR	NR
Ti_3C_2Tx- PANI sensor[168]	NH_3	In-situ polymerization	20	200 ppm	NR	NR
PEDOT:PSS/$Ti_3C_2T_X$[143]	NH_3	Dip-coating technique	36.6	100 ppm	10 ppm	40 s/116 s for 100 ppm
Polysquaraine, poly-(1,4-diamino-2,5-dichlorobenzene-squarine)(PDDS)/ $Ti_3C_2T_x$ [170]	NH_3	Microwave assisted in-situ polymerization	2.2%	1 ppm	500 ppb	NR
N- $Ti_3C_2T_X$/PEDOT:PSS[51]	NH_3	-	13%	10 ppm	10 ppm	280 s/293 s
	CO		0.5%	10 ppm	NR	NR
	NO_X		1%	10 ppm	NR	NR
	H_2S		3%	10 ppm	10 ppm	NR
	SO_2		2 $	10 ppm	10 ppm	NR
PANI/$Ti_3C_2T_X$[11]	NH_3	In-situ self assembly	0.05	25 ppb	25 ppb	600 s/1400 s for 25ppb
	H_2S		1	25 ppm	NR	NR
	CO_2		0.01	10%	NR	NR
	CO		0.05	25 ppm	NR	NR
	SO_2		0.02	25 ppm	NR	NR
						NR
Nb_2CT_X/PANI[128]	NH_3	In-situ polymerization	1.19	20 ppm	20 ppb	218 s/300 s for
	HCHO		0.5	10 ppm	NR	10 ppm
	SO_2		9	10 ppm	NR	NR
	C_2H_5OH		2	10 ppm	NR	NR
	C_3H_6O		2	10 ppm	NR	NR
	H_2S		1	10 ppm	NR	NR
						NR
Nb_2CT_X/PANI-TENG[127]	NH_3	-	9.33	1 ppm	1 ppm	105 s/143 s for
	CH_4		2.5	10 ppm	NR	100 ppm
	CO		1	10 ppm	NR	NR
	HCHO		0.5	10 ppm	NR	NR
	C_2H_5OH		3	10 ppm	NR	NR
	C_3H_6O		2	10 ppm	NR	NR
	SO_2		6	10 ppm	NR	NR
	H_2S		2	10 ppm	NR	NR
						NR
CPAM/$Ti_3C_2T_X$[38]	CH3OH	In-situ polymerization	15%	2000 ppm	NR	NR
	C3H6O		10%	2000 ppm	NR	NR
	C2H5OH		10%	2000 ppm	NR	NR
CPAM/$Ti_3C_2T_X$[38]	NH3	-	1.5	50 ppm	NR	12–14 s for 150 ppm
N-doped $Ti_3C_2T_X$ /PEDOT: PSS[51]	NH_3	Solvothermal	13%	10 ppm	NR	393.6 s/280 s
MXene/PU[171]	Acetone, Ethanol, Methanol	Wet spinning	0.012 20.17	10 ppm Saturated vapor	0.05 ppm	3.5/3.5
MXene-PI[83]	Acetone, Ethanol, Methanol	wet etching solution deposition	0.034	25 ppm	25 ppm	5/5
$Ti_3C_2T_X$/PDDS[170]	NH_3	microwave-assisted synthetic route	2.2%	10 ppm	0.5 ppm	NR
$Ti_3C_2T_X$/urchin-like PAN[172]	NH_3	template + in situ polymerization	3.70	10 ppm	30 ppb	NR

flexible cross-linked CPAM/$Ti_3C_2T_X$ (C-Tx) hybrid in Fig. 16 (e). Interestingly, the expansion in interlayer separation of $Ti_3C_2T_X$ was observed due to the integration of CPAM amongst its layers, as confirmed by a shift in (002) peak of XRD spectra. Moreover, the surge in the I(D):I(G) (the D-peak-to-G-peak intensity ratio) observed from Raman spectroscopy from 0.93 to 0.98 are attributed to the generation of defects in hybridized ILe-MXene offering larger adsorption sites for contaminant molecules as illustrated in Fig. 16 (f). The sensor exhibited excellent NH3 characteristics, including prompt detection/recovery (within 12.7/14.6 s), good repeatability (10 consecutive cycles), and excellent flexibility (for 3 bending cycles with bending angles between 0 and 100o) than its pristine counterparts (Fig. 16 (g)). Thus, the ILe of Ti3C2Tx through CPAM hybridization resulted in devising a highly

flexible, stable and NH_3 sensitive chemiresistor, which is attributed to gluing action of CPAM and creation of defects during hybrid formation. Besides, a surge in NH_3 sensitivity with an increase in relative humidity (RH) was observed but only till 45%, and afterwards, it decreased. The higher concentration of water molecules adsorbed on ILe-MXene surface blocks its interaction with NH_3 and limits its sensitivity. These observations are supported by outcomes reported by Li et al. [11] for PAN/$Ti_3C_2T_X$ chemiresistor. The threshold RH was observed to be 40% RH and sensor exhibited high-performance in terms of LDL of 25 ppb, re-usable and sustainable (up to 88% of the initial response on the 35th day) and highly flexible for (100, 300, and 500 bending times with 20°, 30°, and 40° bending angles). Captivatingly, their agricultural simulation-based outcomes evidenced the practical feasibility of
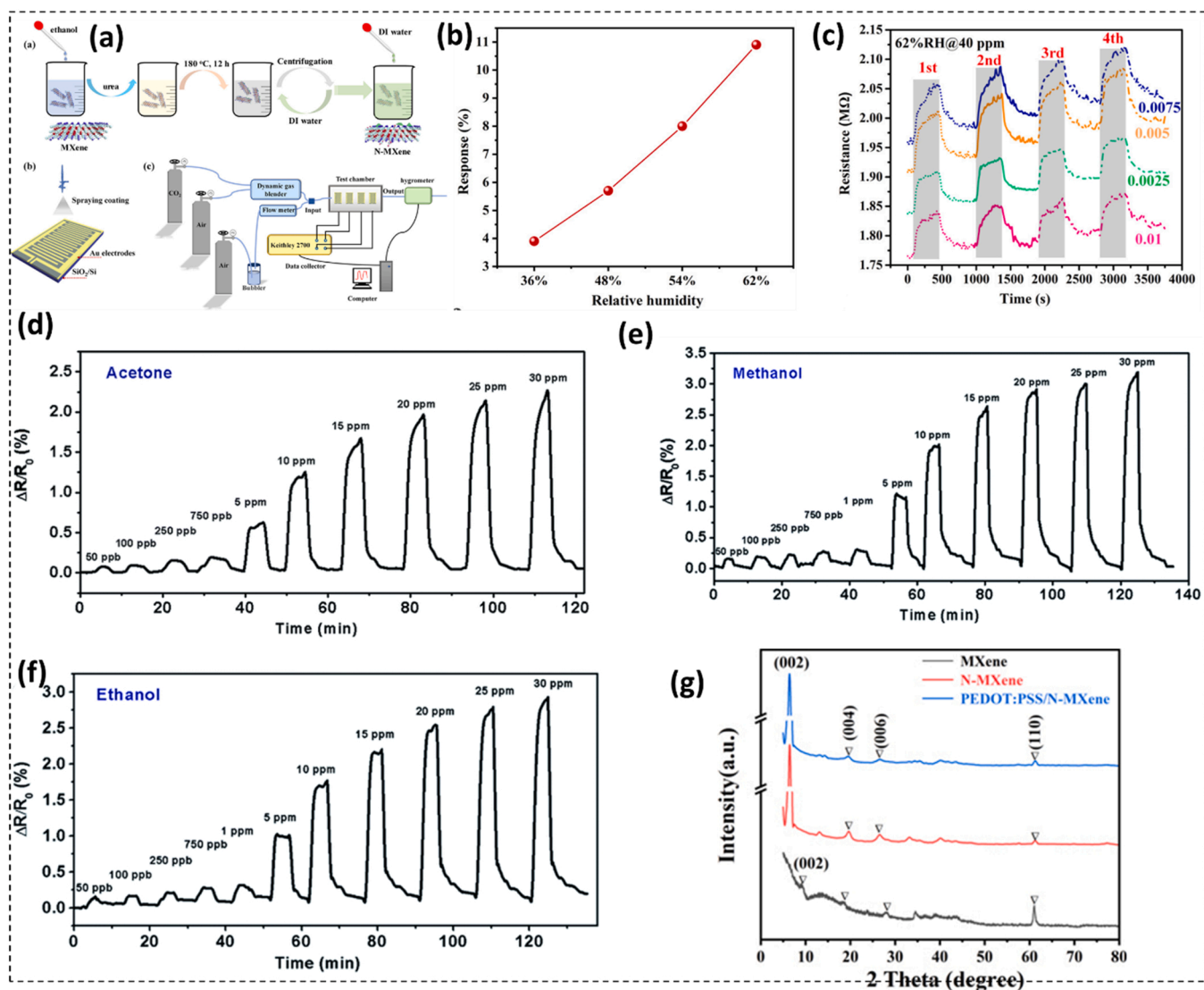
Fig. 17. (a) Schematic of N-MXene sample preparation method, spraying coating on IDEs, and gas measurement system [173]. (b) response as a function of RH illustrated 62% [173]. (c) resistance transients of fabricated four ternary gas sensors prepared with various PEI concentrations toward 40 ppm CO_2 gas under 62% RH@ 20 °C condition [173]. (d-f) Dynamic response curve representation for a 3D-M/P gas sensor upon exposure to acetone, methanol and ethanol with concentrations from 50 ppb to 30 ppm, respectively [146]. (g) XRD results of MXene, N-MXene and PEDOT:PSS/N-MXene (1:0.5) samples [51].

ILe-MXene-based sensor for precise, prompt, real-time, human resource-free, field-deployable and smart agricultural practices.

On the contrary, Jin et al. [143] observed trivial decline in the NH_3 sensing response of $Ti_3C_2T_X$/PEDOT:PSS sensor in variable RH environments (20–90%). They observed a rise in NH_3 sensing response with increased RH and ascribed it to enriched charge transfer results to lessen the average spacing between accrued water molecules. Besides, they witnessed rise in interlayer separation (D-spacing) of Ti3C2Tx sheets due to the integration of PEDOT: PSS in hybrid utilizing spectroscopic and morphological results. The XRD outcomes exhibited shift in (002) plane $Ti_3C_2T_X$ MXene from 8.9° to 6.6° corresponding to rise in interlayer separation in ILe-MXene. The sensor exhibited high-performance NH_3 sensing in terms of room temperature operation, and high sensitivity (9.6% at 10 ppm) as displayed in Fig. 16 (h). Furthermore, Jin et al. [143] observed the variation in sensing response, response span and recovery time with wt% of Ti3C2Tx (0%, 8%, 11%, 15%, 25%, 100%) in ILe-hybridized-MXene. The highest sensing performance was optimized for 15 wt% ILe-MXene due to an increase in its interlayer separation and electrical conductivity, which decreased with a rise in MXene wt% by any further mentioned in Fig. 16 (i). This study portrays that optimising

precursor concentration in ILe-MXenes is key to enhancing its sensing response by regulating its interlayer spacing.

On the contrary, Li et al. [11] mentioned the dependence of NH_3 monitoring behavior of PAN/$Ti_3C_2T_X$ on operational temperatures in the range of 0–40 °C. The sensor exhibited negligible variation in sensing response with a change in operational temperature, illustrating its sensing stability in variable environments. Moreover, the sensor also showed a significant response of around 8% towards 10 ppm of SO_2 and CO, which are significant in light of literature. However, the study lack to further evaluate the sensing features, including 3 S's and 5 R's for both contaminants.

Furthermore, they are a good candidate for developing high-performance air contaminant sensing platforms because of the excellent electrical conductivity caused by faster charge transport in a few layered MXenes. Wang et al. [127,128], for example, evaluated the air contaminant detection performance of Nb_2CT_X/PANI hybrids in two separate reports. The reports differed in terms of the fabrication route used for hybridization of Nb_2CT_X with PANI, which included ex-situ (alternate precursor spraying) and in-situ (one-pot polymerization) techniques. The ex-situ route-assisted fabricated sensor with optimised

Nb_2CTx concentration (0.1 ML spray volume) demonstrated a high sensing response of 2.57% per ppm of NH_3 and 1 ppm of LDL. The sensor was integrated with a triboelectric nanogenerator (TENG) based on two Al electrodes, two triboelectric films (polytetrafluoroethylene (PTFE) film and nylon), and a flexible PET substrate, allowing it to operate on its own [127]. Furthermore, the chemiresistor demonstrated stable sensing performance under changing RH and temperature conditions, emphasising its applications in harsh environments. This report provides preliminary projections for latent ILe-MXene-Organic hybrid-based self-powered and sustainable sensor for smart detection of air contaminants. However, the Nb_2CT_X/PAN hybrid fabricated through in-situ polymerization exhibited 14 times superior sensing response of 29.95% towards 1 ppm of NH_3 than that of ex-situ synthesized hybrid [128]. It is attributed to eh formation of interfacial heterojunctions amongst the precursors throughout the hybrid and expansion of interlayer spacing of MXene layers due to PAN integration. Fascinatingly, the hybrid also exhibited sensitivity of 9% towards 10 ppm of airborne SO_2, which is good in light of literature dedicated to precursors. However, the interference of SO_2 on NH_3 sensing behavior can be picked out of proper choice of electronic circuitry while devising the chemiresistor based on the sensing mechanism and nature of air contaminants (NH_3: reducing and SO_2: oxidizing).

Furthermore, the sensing response of low dimensional MXenes-based sensors is found steady in a varying environment through RH and temperature. For instance, Wang et al. [127,128] exhibited that Nb_2CT_X/PAN sensor was stable for 35 consecutive days, sustaining a sturdy sensing response towards 10 ppm of NH_3. However, in variable environments, they discovered that the sensitivity of Nb_2CT_X/PAN to NH_3 initially increases (0–40% RH) and then decreases (40–90% RH) with increasing RH, with the threshold observed at 40% RH. The accumulation of a thin layer of water molecules on the sensor surface, impeding analyte adsorption sites, is attributed to the RH threshold. As a result, a dynamic equilibrium exists between RH magnitude and NH_3 sensing response, determining the specific threshold RH. Furthermore, as the working temperature of the hybrid increases, the sensing response decreases, which is attributed to the desorption of H_3O^+ ions from the hybrid surface, reducing the sensing response.

The state-of-the-art ILe-MXene-organic hybrids based air contaminant sensors are summarized in Table 4. It is evident that MXene-organic hybrids cater to various bottlenecks associated to commercialization of MXene-based sensors. However, inclusion of more than two precursors can further enhance their sensing performance as discussed for ternary –mixed hybrids in subsequent section.

4.4. Ternary hybridization/heterostructure engineering to architect high-performance ILe-MXenes for air contamination sensing and monitoring

To further improve the sensing performance, mixed ternary hybrids have also been utilized to architect ILe-MXene hybrids for gas contaminant sensing. It aids in including the merits of different types of materials in single hybrid system. For instance, Zhou et al. [173] explored air contaminant detection performance of ternary ILe-MXene hybrid of N-doped MXene, PEI, and rGO (NMPG) (Fig. 17 **(a)**). The fabricated hybrid-based sensor outperformed its competitors in indoor CO_2 detection, including PEI, $Ti_3C_2T_X$, rGO-PEI, $Ti_3C_2T_x$-PEI, N-$Ti_3C_2T_X$, and $Ti_3C_2T_x$-rGO. The sensor was optimized for RH (threshold 62%) and operational temperature (20 oC) for optimum sensing response **(Fig. 17 (b))**. Moreover, this is the case because the pristine rGO and N-doped MXene showed no change in conductivity at these RH-Temperature conditions. Furthermore, the variation in PEI conductivity with RH due to humidity-activated proton conduction reaches saturation at 62%. The PEI concentration variation was also observed for 0.0025, 0.005, 0.0075, and 0.01 mg/ML concentrations, with 0.01 mg/ML exhibiting the highest sensitivity **(Fig. 17 (c))**. It happens owing to the dominance of PEI during detection phenomena at optimized concentration, RH and temperature conditions. Moreover, the issue of negligible recovery was

prominent on purging the sensing chamber with dry air. Moreover, though PEI dominated the sensing phenomena, all three precursor plays a role in the net sensing mechanism. For instance, rGO provided prompt charge carrier pathways owing to its high conductivity, MXene amplified the charge mobility carrier, and PEI generated the charge carriers. The CO_2 detection performance of NMPG sensor (~1% for 8 ppm at 20 °C) was many-fold higher than that of prominent sensing materials, including Ru@WS2 (~1.8% for 20 ppm at 25 °C), LaFeO3 (119% for 2000 ppm at 300 °C), ZnO (20% for 200 ppm at 250 °C), Ag@CuO/-BaTiO3 (9% for 100 ppm at 120 °C), PEEK/MWCNTs (10.5% for 500 ppm at 25 °C), Ca/Al@ZnO (33% for 2500 ppm at 250 °C), and CeO2 (1–10% for 150 ppm at 100 oC). Nevertheless, the processing of ILe-ternary-MXene hybrid is multifarious due to the concurrent optimization of all parameters, comprising the precursor's concentration and operation conditions.

Yuan et al. [146] mentioned a 3D MXene-ternary hybrid (3D-T) of three precursors, including PEI, $Ti_3C_2T_X$, and PVA and evaluated it to detect various air contaminants, including CH_3OH, C_2H_5OH, and C_3H_6O. The electrostatic interaction between the negatively charged Ti3C2Tx surface and the positively charged PEI polymer framework components resulted in self-assembly, which functionalized the surface of the 3D framework. The 3D ternary hybrid demonstrated high porosity, interconnected morphology and high specific surface area, which resulted in superior sensing performance for detecting low trace (~50 ppb) of several VOCs (C_3H_6O, CH_3OH, and C_2H_5OH). Nevertheless, 3D-T-based sensor exhibited negligible sensing response towards hydrocarbons (cyclohexane and C7H8) and low sensing response towards polar inorganic analytes (NH_3 and NO_x). The surface terminals on 3D-T surface (especially -OH and -F) form hydrogen bonds with polar inorganic contaminants and hydrocarbons, leading to charge transfer. The magnitude of sensing response was reliant on the degree of hydrogen bonding between contaminant molecules and 3D-T surface. Fascinatingly, it was noticed that the 3D-T sensor resistance increases on exposure to all tested contaminants, regardless of their nature. It is due to the dominance of $Ti_3C_2T_x$-MXene in the fabricated hybrid contributing to high metallic conductivity during interaction with a contaminant environment. The sensor showed a significant linear range of detection at 50 ppb–3×10^5 ppm, 50 ppb – 8×10^4 ppm and 50 ppb–1.5×10^5 ppm for C_3H_6O, C_2H_5OH and CH_3OH, respectively Fig. 17 (d-f). Besides, the sensor exhibited high flexibility and consistent sensing response even for one thousand bending cycles and worked at ambient temperature. Moreover, the sensor demonstrated manifold superior sensing performance towards C_3H_6O, C_2H_5OH, and CH_3OH than well-established rGO-based 3D polymer framework sensors. It is ascribed to the limited oxygen terminations present on basal and edge planes of rGO compared to MXenes, reducing the probability of interaction between rGO and air contaminants. The scarcity of oxygen surface terminals also felicitates the hydrogen bonding between air contaminant molecules and rGO, hindering recovery and saturating sensitivity. Despite excellent sensing performance, the major issue associated with 3D-T sensor was its slow response and recovery time of order of few minutes, which limits its practical applications.

Qiu et al. [51] fabricated an accordion-like N-doped-$Ti_3C_2T_X$/PEDOT:PSS hybrid for sensing NH_3 at the molecular level. This study reports integrating two ILe techniques, including heteroatom doping and hybridization. It was observed that the integration of PEDOT:PSS and urea treatment resulted in the expansion of $Ti_3C_2T_X$ layers, as observed from a downward shift in (002) peak of MXene in XRD spectra, which felicitates molecular transport in ternary ILe-MXene system (Fig. 17 (g)). The sensor exhibited n-type sensing and semiconducting behavior, which was attributed to the formation of n-type TiO2 nanoparticles due to oxidation of several Ti-sites along with N-doping substitution. These nanoparticles served as active electron donors, catalyzing the system during the sensing mechanism. Moreover, the synergistic effects resulting from interfacial integration of p-type PEDOT:PSS and n-type N-$Ti_3C_2T_X$ favored the air contaminant
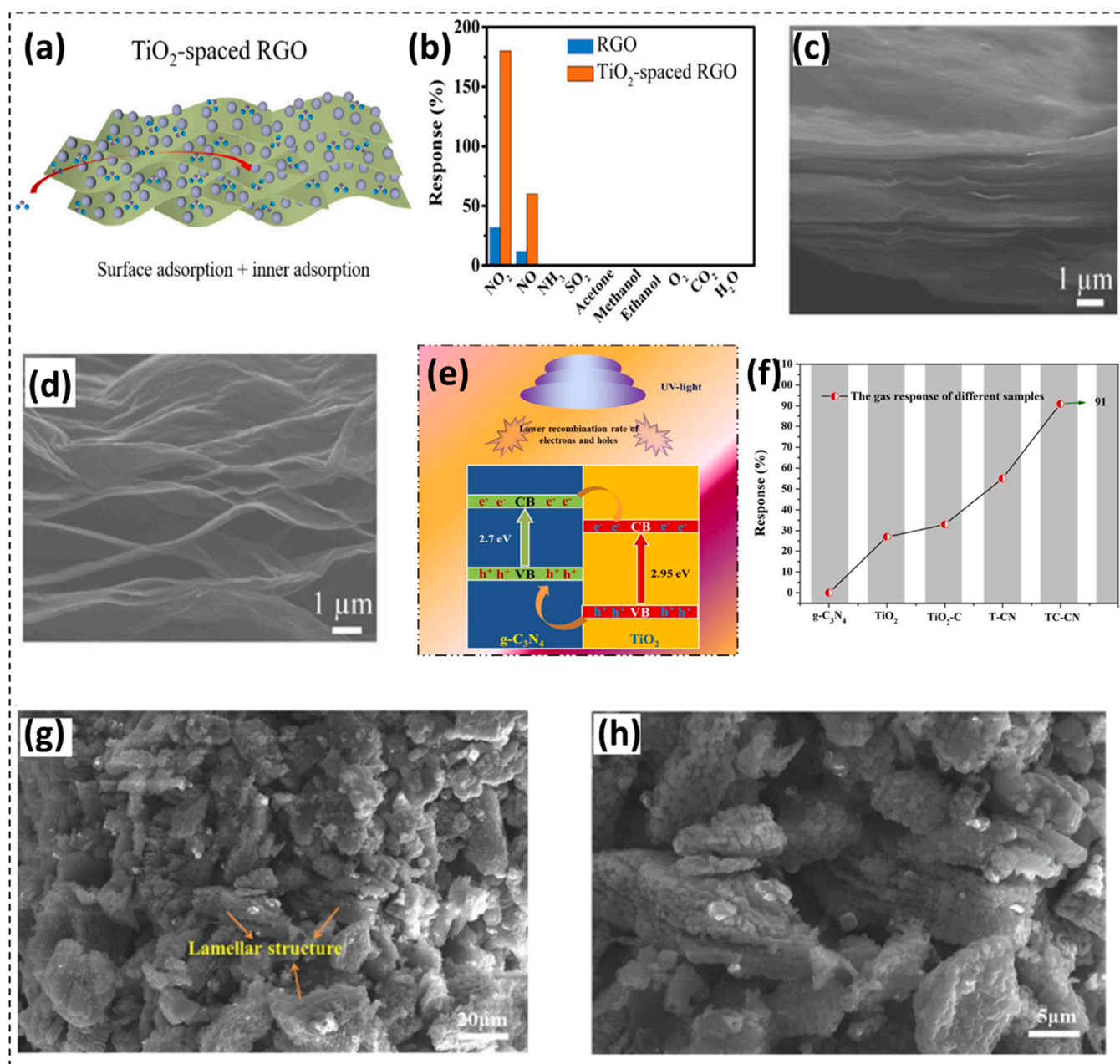
Fig. 18. (a-b) Schematic illustration of pristine RGO films, TiO-spaced RGO films and Sensing response of the sensor upon exposure to different gas analytes [174]. (c-d) Cross-sectional SEM images of the pure RGO film and TiO$_2$-spaced RGO film [174]. (e-f) Schematic illustration of the derived MXene-based TiO$_2$-C/g-C$_3$N$_4$ lamellar structure under UV irradiation and sensitivity response curve of the materials by utilizing ethanol analyte [175]. (g-h) Cross-sectional SEM images of TC-CN [175] and (i) T-CN [175].

monitoring performance. The sensing behavior was ascribed to modulation of the depletion layer formed at p-n interface in air contaminant environment.

Besides, Song and co-workers [174] reported the MXene-derived TiO$_2$ NPs intercalating amidst the RGO NS for sensitive gas detection. The as synthesized prepared through spray coating method in which TiO$_2$ nanospacers dereived from the MXene to further intercalate amongst the RGO sheet. Whereas in the resultant, the prepared assembly (TiO$_2$-spaced RGO) sheets are connected in mm-scale pores as described in Fig. 18 (a). Moreover, the material sensing in various gas detection, including (NO$_2$, NO, NH$_3$, SO$_2$, acetone, methanol, ethanol, O$_2$, CO$_2$, and H$_2$O) respectively. Amongst all, for NO sensing, the derived TiO$_2$-spaced RGO yields an excellent response of 55% towards the 1 ppm of NO concentration. Similar results are obtained for NO$_2$, which has a

sensitivity response of up to 62% for 1 ppm and was probably similar to N$_2$ (Fig. 18 (b)). In addition, the improvement in the sensing performance is ascribed to enhance the interlayer spacing and accessible surface area through TiO$_2$ NP. At the same time, the evolution of gas during the in-situ oxidation mechanism enhanced the ILE distance amidst the RGO layers, affirmed by the evaluation among the cross-sectional SEM images of the TiO$_2$-spaced RGO and pristine RGO films. Moreover, the prepared nanosheets (Pristine RGO) showed the tightly closed stacked LBL morphology along with the flat sheet assembly. While on the other side, TiO$_2$ spaced RGO configuration possessed the closed wrinkled sheet assembly along with the plentiful macropores having the ranges from tens of nm to few µm amidst RGO sheets as highlighted in Fig. 18 (c-d).

Hou et al. [175] reported the MXene derived lamellar structure with

Table 5

State-of-the-art ternary ILe-MXene hybrids for air contaminant detection.

Sensing Elements	Gaseous Contaminant	Preparation Method	Sensitivity	Concentration	LDL/ LOD	Recovery/Response Time
N-Ti3C2Tx-PEI-rGO[173]	HCHO	Spray coating	0.3%	40 ppm	NR	NR
ZnTi-LDHs (LDHs/Ti$_3$C$_2$T$_x$[52]	NH$_3$	Hydrothermal method	1.26	100 ppb	100 ppb	9 s/11 s
SnO-SnO$_2$/ Ti$_3$C$_2$T$_x$[153]	Acetone	Hydrothermal	12.1	100 ppm	NR	9 s/18 s
Co$_3$O$_4$ @PEI/Ti$_3$C$_2$T$_x$[176]	NO$_x$	Hydrothermal	27.9	100 ppm	30 ppb	73 s/2 s
MXene/rGO/CuO[177]	Acetone	Hydrothermal	52.09%	100 ppm	NR	7.5/6.5 s
MXene/PANI/BC[178]	NH$_3$	Self assembly process	54.92%	2.5–12.5 ppm	56.49 ppb	NR
TiO$_2$-RGO/MXene[179]	NO$_2$	in situ oxidation	172%	1 ppm	50 ppb	210 s/78 s
N-MXene with TiO$_2$ heterophase and PTFE[180]	NH$_3$	urea-involved solvothermal treatment	7.3%	1 ppm	200 ppb	NR
TiO$_2$-C/g-C$_3$N$_4$[175]	Ethanol	in situ growth	91	10 ppm	NR	NR
MXene/TiO$_2$/C-NFs[181]	NH$_3$	electrospinning	1	100 ppm	NR	62 s/76 s
Co$_3$O$_4$/Al$_2$O$_3$ @Ti$_3$C$_2$T$_x$[182]	NO$_x$	Hydrothermal	40.3	100 ppm	NR	1.3 s
Co$_3$O$_4$/Ti$_3$C$_2$T-MOF[183]	Ethanol	In-situ growth	190	50 ppm	<1 ppm	50 s/45 s
N-doped MXene/TiO$_2$ with RGO[184]	HCHO	Solvothermal	4	40 ppm	NR	132/26
Ag@TiO$_2$ /MXene[185]	NH$_3$	sonochemical	71.8	50 ppm	5 ppm.	NR
Ti$_2$C$_2$T$_X$ MXene@TiO$_2$/MoS$_2$[186]	NH$_3$	hydrothermal method	163.3%	100 ppm	500 ppb	88/117
Ti$_3$C$_2$/V$_2$O$_5$/CuWO$_4$[187]	NH$_3$	-	53.5 6.4	51 ppm	0.3 ppm 5 ppm	NR
[MIL-125(Ti)/FexTiyOz]T-X[188]	Acetone	Calcination +solvothermal	351.1	100 ppm	NR	5 s/16 s
Ti$_3$C$_2$T$_x$ MXene/rGO/SnO$_2$[189]	HCHO	Hydrothermal	54.97%	10 ppm	NR	2.2 s/2.9 s
MoO$_2$/MoO$_3$/MXene[190]	Ethanol	Hydrothermal	19.77	200 ppm	5 ppm	276 s/46 s
Au-In$_2$O$_3$/Ti$_3$C$_2$T$_x$[191]	HCHO	electrostatic self-assembly + in-situ reduction	31%	5 ppm	NR	4 s/5 s
MoO$_3$/TiO$_2$/Ti$_3$C$_2$T$_x$[190]	isopropanol	Hydrothermal	245%	50 ppm	NR	40/100

TiO$_2$-C/g-C$_3$N$_4$ for gas sensing performance by applying the UV irradiation of light. The as-fabricated material exhibits an excellent sensitive response up to 91 at the concentration of 10 ppm for ethanol analyte (Fig. 18 (e-f)). Furthermore, the SEM image in Fig. 18 (g) ascribes the MXene-like layered structure of TC-CN with the TiO2 particles, which further affirms the accumulation of g-C$_3$N$_4$ well-preserved the MXene layered structure. Besides, the T-CN structure exhibits no layered structure like TC-CN, as shown in Fig. 18 (h). in addition, it is noteworthy that the creation of structural differences disturbs the gas-sensing performance among these two heterojunctions.

The state-of-the-art ternary ILe-MXene hybrids for air contaminant detection are summarized in Table 5. It is evident that ternary-mixed ILE-MXene hybrids are high- performance material to develop gas sensing platforms. They have potential to develop next-generation air contaminant sensors for environmental remediation and monitoring applications.

4.5. Challenges associated with hybridization/heterostructure engineering strategies to engineer of ILe-MXenes and their application in air contamination sensing and monitoring

The state-of-the-art ILe-MXene-hybrids for air contaminant monitoring demand imperative progresses towards improving the manufacturing and processing strategies, precursor optimization, and sensor configuration. Moreover, it raises challenges of safe, scalable and controlled manufacturing, simultaneous optimization of precursors to achieve desired physicochemical attributes, advancing sensing performance and configuration, and regulating caused environmental contamination. Therefore, more work is required to investigate potential alternate solutions and strategically build specialised protocols for each corresponding difficulty. By doing so, eco-friendly, prompt, economical, energy-efficient and high-performance sensors based on hybridized ILe-MXene can be developed. Amongst all, hybridization is most suitable technique as compared to others since it serves multiple purposes including structural and ambient stability, improving sensing performance due to synergistic effects and modifying composite chemistry as per targeted analyte. However, every interlayer modulation strategy is concerned with generic and specific challenges, which needs to be address.

4.5.1. Eco-friendly, scalable and controlled manufacturing and storage

The existing techniques for ILe-MXene manufacturing through hybridization/heterostructure engineering are conquered by hazardous, corrosive and punitive chemical-based exfoliation, which harmfully affects human health and ecosystem. Even the advanced, scalable in-situ HF strategy contaminates the ecosystem significantly. Additionally, it generates unfavorable surface terminals, such as fluorine surface terminals degrading its air contaminant sensing performance [13,54,58]. As a result, there is a desire to investigate alternative manufacturing strategies such as chemical vapour deposition (CVD), green chemistry assisted manufacturing, and salt-template growth [4,192–194]. However, the use of salt-template routes is limited due to the ILe-MXene structures' dependence on crystal symmetry and lattice parameters of the used precursors [50]. Contrary, CVD strategy is reasonable for manufacturing ILe-MXene with fewer layers and not for ML-MXene hybrids [58]. It is because of its metamorphosis structure and manifold stoichiometry related to ML-MXenes and its hybrids. Moreover, scalability is the most prominent issue associated with these alternative strategies, including mechanical exfoliation, MBE and CVD and, due to low yield. Besides, there are no dedicated studies evaluating green precursors such as phytochemcials or biomes for manufacturing ILe-MXenes. However, the abundance, biocompatible, renewable and non-toxic attributes of green precursors have the potential to devise safe and eco-friendly fabrication techniques for ILe-MXene manufacturing. Thus, it raises demand to explore safe and scalable manufacturing strategies for engineering ILe-MXenes. Additionally, the storage and post-processing requirements of ILe-MXenes harden the trials owing to their high reactivity towards humid and oxygen environments. Although there are substantial techniques to store and post-process ILe-MXenes, they are still multifaceted, expensive, and time-consuming, increasing human resource requirements. Thus, enriched production methods are a prerequisite to achieving a high yield of ILe-MXene and hybrids with preferred surface chemistry given targeted detecting applications.

Furthermore, the scalable hybridization engineering of ILe-MXenes necessitates concurrent optimization of precursors, which is perplexing and limits their commercial viability. For example, the attainment of flexibility through integrating polymers in MXenes costs its electrical conductivity. In addition, there exists a relationship between the mechanical robustness of MXene and the flexibility due to polymers during

the machine processing stage of hybridization engineering of ILe-MXenes. The superior concentration of one precursor may potentially disrupt the distinct advantage of other precursors. For instance, the integration of macromolecules/inorganic materials between the MXene layers surges its interlayer spacing ensuing in a specific strain, which disrupts the charge transport pathways in MXenes [143].

On the contrary, the higher concentration of MXenes results in metallic conductivity and loss of its semiconducting nature. Thus, there is a synchronized interplay between the precursor's concentration and processing factors. Furthermore, it involves numerous tribological valuations to govern the threshold concentration of precursors in ILe-MXene with desired attributes. These indications highlight the requirement of controlled trade-offs amongst the processing parameters and precursor's concentration of ILe-MXene fabricated using hybridization/heterostructure engineering. In this context, percolation threshold of every precursor in context of particular desired property must be evaluated using theoretically using advanced data analytics and machine learning techniques, which results in revealing of optimized trade-offs of precursors.

4.5.2. Improvements in sensing characteristics

ILe-MXene sensors fabricated through hybridization engineering show a delayed response and recovery towards several air contaminants, hindering their commercial prospects. It results from specific interactions between air contaminant and MXene, due to their higher binding and adsorption energies over MXene surface. Consequently, the sensor takes a long time to recover to its preliminary conducting state. Nevertheless, the response and recovery of a few seconds or fractions of seconds is a criterion to architect next-generation air contaminant sensors. It can be achieved by improving the architect and configuration of sensor by using interdigitated electrodes of innovative configurations as a substitute for conventional sensing electrodes with parallel configurations, decreasing the noise accompanied by sensing signal originated due to electrode-material-device interface through suitable choice of constituents with fundamental considerations, integration of two or more ILe routes such as heteroatom doping followed by hybridization, utilizing catalytic nanoparticles for surface enrichment of MXenes resulting in prompt response on environment variation, appropriate selection of stoichiometry of hybrid as per target contaminant by investigating their surface interactions using advanced machine learning approaches based on DFT and MD, augmenting the thickness of device for fast adsorption/desorption of contaminant molecule, and incorporating rapid data acquisition tools.

Moreover, several ILe-MXene displays robust sensing response towards numerous environmental stimuli, including gases, humidity, VOCs, and biomes ensuing in an analogous deceiving response. Though it aids in architecting multifunctional sensors for the detection of various stimuli simultaneously, it also results in augmented cross-sensitivity. Such interfering sensing signals are not desirable during sensing performance since it leads to incorrect stimuli detection and quantification. For example, human breath based sensing devices detecting VOCs in exhaled breath are strongly interfered with by humidity present in human breath resulting from various biological metabolisms [195,196]. Thus, a robust anti-interference competency towards undesired environmental stimulus is required for durable, accurate and reliable operation of air contaminant sensors. It can be attained by appropriate choice of electronic configuration of sensing device and machine-trained modules based on nature and contaminant interaction with ILe-MXenes. Numerous modern-age technologies, including neural network analysis, AI, pattern determination, correlation analysis and data analytic tools, play a vital function in formulating such smart sensing modules, which can address the prominent challenge of cross-sensitivity.

5. Prospects of ILe-MXenes for advanced sensing applications and integration of modern-age technologies

The advanced monitoring systems architected utilizing sensor arrays and ILe-MXenes like electrical nose or on-site sensors can be devised by integrating modern-age technologies, including ML, bioinformatics, AI, and pattern recognition. Besides, assimilating IoTs/IoNTs, 5 G/6 G communication, and data clouding with sensors can transform the state-of-the-art ILe-MXene-based air pollutant detection and monitoring systems. The single-chip sensor integrated with feature for internet connection, Bluetooth, and several other are crucial for real-time smart monitoring of various air toxins. These sensors must also possess exceptional flexibility and robustness to endure extreme environmental variations. The sensor chip integrated into IoT/IoNT can be mounted at each plausible contaminant emission/leakage site. They can simultaneously monitor various air contaminants and send sensing signals wirelessly to sensing devices programmed with the IoTs/IoNTs demonstrating the "on-site monitoring" module. It can revolutionize conventional public management, public transport and healthcare structures with reduced human resources. For example, installing IoT-supported sensors in vehicles can help to timely monitor vehicular emissions and control environmental contamination. Moreover, it can account for strategic and smart fuel consumption in vehicles by real-time monitoring of vehicular emission and its component analysis, along with the integration of advanced ML algorithms. Moreover, IoT/IoNT integrated intelligence can be devised for a solution-on-chip module for plentiful complex problems. For example, integrating IoNT sensors on face masks can cater to air pollution problems and infectious outbreaks. To detect any such trapped contaminant or pathogen, the pre-trained module-based face masks and respirators can activate inhibition mode and destroy the airborne contaminant using various strategies such as electrostatic, photocatalytic or anti-pathogenic activations [2,197]. Such intelligent strategies can revolutionize modern public healthcare and management systems.

Furthermore, ILe-MXenes has been used in smart agricultural practices by integrating IoNTs, AI, drones, and data clouding. For example, Li et al. [11] discovered the latent of a flexible PAN/Ti$_3$C$_2$T$_X$ hybrid for smart NH$_3$ volatilization detection in agricultural fields. In the context of air pollution, advanced functional and hybridised materials can be combined on a single sensor chip to scavenge trapped air contaminants, assisting in achieving sustainability in modern "point-of-solution" monitoring technologies [2,7]. Sonu et al. [198] also investigated the potential of intelligent sensing systems in conjunction with drone and bioinformatics technologies for detecting and combating airborne plant pathogens with minimal human resources. Furthermore, Khosla et al. [54] demonstrated ILe-MXenes' potential as smart and intelligent membranes for environmental remediation applications. Moreover, the scope of ILe-MXenes also extends to detection of airborne pathogens such as SARS-CoV-2, which is highly required in combatting public health emergencies and spread of contagion through air [17,199]. Thus, the cutting-edge ILe-MXene sensors necessitate the rapid expansion of current machine algorithms to pre-train and examine the pragmatic statistics to deliver big data-based forecasts such as early detection of infectious diseases and epidemic outbreaks or timely recognition of air contaminant emission/leakages that contribute to human and ecological welfare.

ILe-MXenes are also being developed as high-performance humidity sensing platforms with food packaging, chain, processing, storage, and transport applications. However, ILe-MXene-based sensors are not limited to detecting air contaminants. Instead, it develops non-invasive breath biomarker detection strategies to replace sophisticated, time-consuming biosensing strategies. The detection of 0.8 ppm or lower traces of NH$_3$ in human breath, for example, has the potential to detect gastric ulcers and renal failure in humans [20]. Furthermore, a C$_3$H$_6$O with LDL levels ranging from 300 to 1800 ppb can be used to diagnose diabetes [195]. However, dedicated efforts are required to assess these
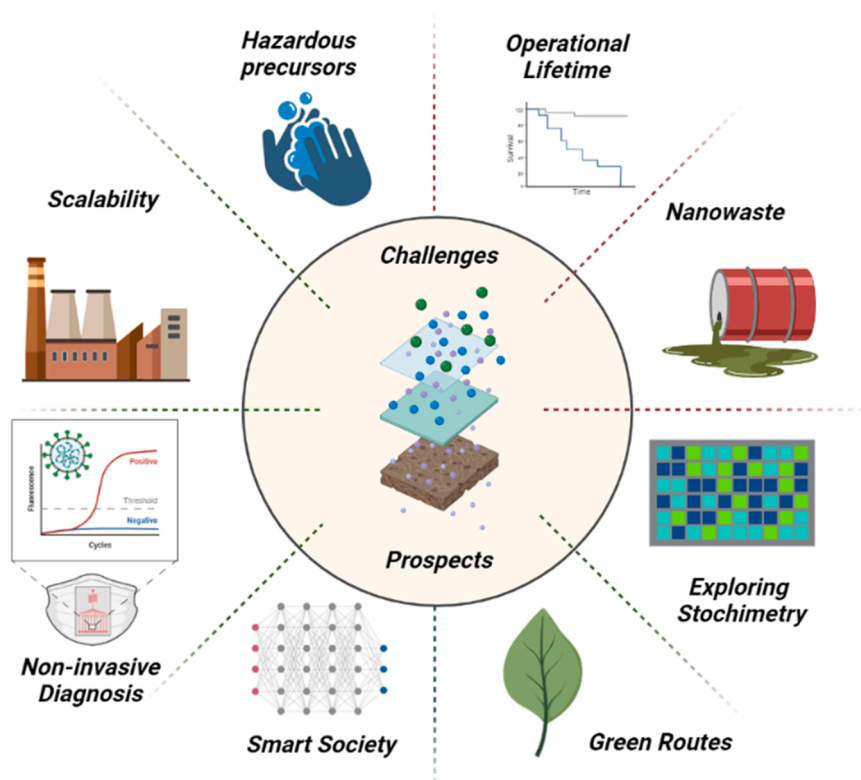
Fig. 19. Challenges, alternate solutions and cutting-edge prospects of ILe-MXene to develop air contamination detecting sensors.

possibilities and conduct clinical trials for validation.

Besides, integrating triboelectric generators with sensors adds a self-operation feature without requiring any peripheral energy supply [200]. In addition, ILe-MXenes are themselves utilized for fabrication of nanogenerators owing to their metallic and flexible attributes [201]. ILe-MXene layers can also be utilized as joule heaters to operate sensors fabricated using MXenes or other sensing materials [202]. The generation of solid waste due to the large-scale use of ILe-MXene-based sensors is a matter of concern. However, the surface modification strategies reduce their cytotoxicity and eco-toxicity. Moreover, ILe- MXenes can be repurposed, reused and recycled, addressing the issue of solid-waste management. A discussion has been added as required places. The secondary environmental contamination is due ILe-MXene can be catered by using its repurpose, biodegradable and recyclable derivatives in specific solutions, which diminishes the possibility of nano waste generation anticipated due to large-scale application of ILe-MXenes [203, 204]. For instance, Zhang et al. [204] demonstrated the degradation of sensor based on ILe-MXene aerogel and cross-linked collagen fibers within forty days of keeping it in an alkaline solution. The biodegradable attribute is due to the reinforcement of ILe-MXenes with natural fibres. Hence, ILe-MXenes open innovative prospects for smart sensing of air contaminants with economical, field-deployable, compact, flexible, energy-efficient and prompt sensors with excellent sensing response, stability, and selectivity, satisfying sustainable development goals (Fig. 19).

6. Conclusion

In conclusion, ILe-MXenes, in utmost topical studies, embrace all indispensable features in terms of advanced physicochemical attribute and proficiency to be developed as modern-age multi-functional sustainable sensors with a real-world and commercial perspective. Nevertheless, several challenges necessitate substantial and devoted research explorations prior to projecting ILe-MXenes as superlative sensing materials for smart, field-deployable, on-site, single-chip and next-generation sensors and substituting the existing prevalent sensors. These progressive features can only be integrated into sensors through versatile efforts of engineers, public health workers, data scientists, informatics, material scientists, environmentalists, medical experts, policymakers, and industries toward the possible commercialization of ILe-MXenes as advanced and functional sensing materials. In proximity, ILe-MXenes are expected to scale and progress in each panorama for devising modern-age intelligent sensors for human and ecological betterment, with prospects of circular and sustainable economy.

Declaration of Competing Interest

The authors declare that they have no known competing financial interests or personal relationships that could have appeared to influence the work reported in this paper.

Data Availability

No data was used for the research described in the article.

Acknowledgment

References

[1] I. Manisalidis, E. Stavropoulou, A. Stavropoulos, E. Bezirtzoglou, Environmental and health impacts of air pollution: a review, Front. Public Heal. 8 (2020) 14, https://doi.org/10.3389/fpubh.2020.00014.

[2] V. Chaudhary, A. Gautam, P. Silotia, S. Malik, R. de Oliveira Hansen, M. Khalid, A. Khosla, A. Kaushik, Y.K. Mishra, Internet-of-nano-things (IoNT) driven

intelligent face masks to combat airborne health hazard, Mater. Today (2022), https://doi.org/10.1016/j.mattod.2022.08.019.

[3] V. Chaudhary, P. Bhadola, A. Kaushik, M. Khalid, H. Furukawa, A. Khosla, Assessing temporal correlation in environmental risk factors to design efficient area-specific COVID-19 regulations: Delhi based case study, Sci. Rep. 12 (2022) 12949, https://doi.org/10.1038/s41598-022-16781-4.

[4] V. Chaudhary, N. Ashraf, M. Khalid, R. Walvekar, Y. Yang, A. Kaushik, Y. K. Mishra, Emergence of MXene–polymer hybrid nanocomposites as high-performance next-generation chemiresistors for efficient air quality monitoring, Adv. Funct. Mater. (2022) 2112913, https://doi.org/10.1002/adfm.202112913.

[5] WHO, Ambient (outdoor) air pollution, ⟨Https://Www.Who.Int/En /News-Room/Fact-Sheets/Detail/Ambient-(Outdoor)-Air-Quality-and-Health⟩. (2018).

[6] R.D. Brook, S. Rajagopalan, C.A. Pope, J.R. Brook, A. Bhatnagar, A.V. Diez-Roux, F. Holguin, Y. Hong, R.V. Luepker, M.A. Mittleman, A. Peters, D. Siscovick, S. C. Smith, L. Whitsel, J.D. Kaufman, Particulate matter air pollution and cardiovascular disease, Circulation 121 (2010) 2331–2378, https://doi.org/10.1161/CIR.0b013e3181dbece1.

[7] J. Cherusseri, C.M. Savio, M. Khalid, V. Chaudhary, A. Numan, S.J. Varma, A. Menon, A. Kaushik, SARS-CoV-2-on-chip for long COVID management, Biosensors 12 (2022) 890, https://doi.org/10.3390/bios12100890.

[8] S.K. Maurya, M.S. Baghel, Gaurav, V. Chaudhary, A. Kaushik, A. Gautam, Putative role of mitochondria in SARS-CoV-2 mediated brain dysfunctions: a prospect, Biotechnol. Genet. Eng. Rev. (2022) 1–26, https://doi.org/10.1080/02648725.2022.2108998.

[9] D.E. Schraufnagel, J.R. Balmes, C.T. Cowl, S. De Matteis, S.-H. Jung, K. Mortimer, R. Perez-Padilla, M.B. Rice, H. Riojas-Rodriguez, A. Sood, G.D. Thurston, T. To, A. Vanker, D.J. Wuebbles, Air pollution and noncommunicable diseases, Chest 155 (2019) 417–426, https://doi.org/10.1016/j.chest.2018.10.041.

[10] V.Chaudhary Sonu, A paradigm of internet-of-nano-things inspired intelligent plant pathogen-diagnostic biosensors, ECS Sens. 1 (2022) 031401, https://doi.org/10.1149/2754-2726/AC92ED.

[11] X. Li, J. Xu, Y. Jiang, Z. He, B. Liu, H. Xie, H. Li, Z. Li, Y. Wang, H. Tai, Toward agricultural ammonia volatilization monitoring: a flexible polyaniline/Ti3C2T hybrid sensitive films based gas sensor, Sens. Actuators B Chem. 316 (2020), 128144, https://doi.org/10.1016/j.snb.2020.128144.

[12] V. Chaudhary, A. Kaushik, H. Furukawa, A. Khosla, Review—towards 5th generation ai and iot driven sustainable intelligent sensors based on 2d mxenes and borophene, ECS Sens. 1 (2022) 013601, https://doi.org/10.1149/2754-2726/ac5ac6.

[13] V. Chaudhary, A. Gautam, Y.K. Mishra, A. Kaushik, Emerging MXene–polymer hybrid nanocomposites for high-performance ammonia sensing and monitoring, Nanomaterials 11 (2021) 2496, https://doi.org/10.3390/nano11102496.

[14] F. Da Silva Santos, L. Vitor da Silva, P.V.S. Campos, C. de Medeiros Strunkis, C.M. G. Ribeiro, M.O. Salles, Review—recent advances of electrochemical techniques in food, energy, environment, and forensic applications, ECS Sens. 1 (2022), 013603, https://doi.org/10.1149/2754-2726/ac5cdf.

[15] S. Ghosh, B. Sachdeva, P. Sachdeva, V. Chaudhary, G.M. Rani, J.K. Sinha, Graphene quantum dots as a potential diagnostic and therapeutic tool for the management of Alzheimer's disease, Carbon Lett. (2022), https://doi.org/10.1007/s42823-022-00397-9.

[16] V. Chaudhary, Prospects of green nanotechnology for efficient management of neurodegenerative diseases, Front. Nanotechnol. 4 (2022), https://doi.org/10.3389/fnano.2022.1055708.

[17] V. Chaudhary, V. Khanna, H.T. Ahmed Awan, K. Singh, M. Khalid, Y. Mishra, S. Bhansali, C.-Z. Li, A. Kaushik, Towards hospital-on-chip supported by 2D MXenes-based 5th generation intelligent biosensors, Biosens. Bioelectron. (2022) 114847, https://doi.org/10.1016/j.bios.2022.114847.

[18] K. Markandan, Y.W. Tiong, R. Sankaran, S. Subramanian, U.D. Markandan, V. Chaudhary, A. Numan, M. Khalid, R. Walvekar, Emergence of infectious diseases and role of advanced nanomaterials in point-of-care diagnostics: a review, Biotechnol. Genet. Eng. Rev. (2022) 1–89, https://doi.org/10.1080/02648725.2022.2127070.

[19] U. Reddicherla, S.M. Ghoreishian, M.R. Gokana, Y. Cho, Y.S. Huh, Review—emerging trends in the development of electrochemical devices for the on-site detection of food contaminants, ECS Sens. (2022), https://doi.org/10.1149/2754-2726/ac9d4a.

[20] A. Gautam, Towards Modern-Age Advanced Sensors for the Management of Neurodegenerative Disorders: Current Status, Challenges and Prospects, ECS Sens Plus 1 (2022), 042401, https://doi.org/10.1149/2754-2726/ac973e.

[21] P. Yadav, A. Singh, S. Singh, R.P. Singh, Design and Development of Paper/ZnO–SnO₂ Heterostructured Ultra-Fast TENG Based LPG Sensor,, ECS Sens. (2022), https://doi.org/10.1149/2754-2726/aca48b.

[22] S. Dhall, B.R. Mehta, A.K. Tyagi, K. Sood, A review on environmental gas sensors: materials and technologies, Sens. Int. 2 (2021) 100116, https://doi.org/10.1016/j.sintl.2021.100116.

[23] K.R. Singh, V. Nayak, J. Singh, R.P. Singh, Nano-enabled wearable sensors for the Internet of Things (IoT), Mater. Lett. 304 (2021) 130614, https://doi.org/10.1016/j.matlet.2021.130614.

[24] S.N. Banitaba, S.V. Ebadi, P. Salimi, A. Bagheri, A. Gupta, W.U. Arifeen, V. Chaudhary, Y.K. Mishra, A. Kaushik, E. Mostafavi, Biopolymer-based electrospun fibers in electrochemical devices: versatile platform for energy, environment, and health monitoring, Mater. Horiz. (2022), https://doi.org/10.1039/D2MH00879C.

[25] A.F. Payam, B. Kim, D. Lee, N. Bhalla, Unraveling the liquid gliding on vibrating solid liquid interfaces with dynamic nanoslip enactment, Nat. Commun. 13 (2022) 6608, https://doi.org/10.1038/s41467-022-34319-0.

[26] N. Bhalla, A.F. Payam, A. Morelli, P.K. Sharma, R. Johnson, A. Thomson, P. Jolly, F. Canfarotta, Nanoplasmonic biosensor for rapid detection of multiple viral variants in human serum, Sens. Actuators B Chem. 365 (2022), 131906, https://doi.org/10.1016/j.snb.2022.131906.

[27] R.C. Nnachi, N. Sui, B. Ke, Z. Luo, N. Bhalla, D. He, Z. Yang, Biosensors for rapid detection of bacterial pathogens in water, food and environment, Environ. Int. 166 (2022), 107357, https://doi.org/10.1016/j.envint.2022.107357.

[28] P. Rawat, P. Kumar Sharma, V. Malik, R. Umapathi, N. Kaushik, J.-S. Rhyee, Emergence of high-performing and ultra-fast 2D-graphene nano-biosensing system, Mater. Lett. 308 (2022) 131241, https://doi.org/10.1016/j.matlet.2021.131241.

[29] C. Venkateswara Raju, C. Hwan Cho, G. Mohana Rani, V. Manju, R. Umapathi, Y. Suk Huh, J. Pil Park, Emerging insights into the use of carbon-based nanomaterials for the electrochemical detection of heavy metal ions, Coord. Chem. Rev. 476 (2023), 214920, https://doi.org/10.1016/j.ccr.2022.214920.

[30] R. Umapathi, S.M. Ghoreishian, G.M. Rani, Y. Cho, Y.S. Huh, Review—emerging trends in the development of electrochemical devices for the on-site detection of food contaminants, ECS Sens. 1 (2022), 044601, https://doi.org/10.1149/2754-2726/ac9d4a.

[31] P. Yadav, A. Singh, S. Singh, D. Kumar, Design and development of paper/ZnO–SnO 2 heterostructured ultra-fast TENG based LPG sensor, ECS Sens. 1 (2022), 042601, https://doi.org/10.1149/2754-2726/aca48b.

[32] A. Gautam, Towards modern-age advanced sensors for the management of neurodegenerative disorders: current status, challenges and prospects, ECS Sens. 1 (2022), 042401, https://doi.org/10.1149/2754-2726/ac973e.

[33] S. Agrohiya, S. Dahiya, P.K. Goyal, I. Rawal, A. Ohlan, R. Punia, A.S. Maan, Nickel doped zinc oxide thin films for visible blind ultraviolet photodetection applications, ECS Sens. 1 (2022), 043601, https://doi.org/10.1149/2754-2726/ac973f.

[34] V. Khanna, K. Singh, S. Kumar, S.A. Bansal, M. Channegowda, I. Kong, M. Khalid, V. Chaudhary, Engineering electrical and thermal attributes of two-dimensional graphene reinforced copper/aluminium metal matrix composites for smart electronics, ECS J. Solid State Sci. Technol. 11 (2022), 127001, https://doi.org/10.1149/2162-8777/aca933.

[35] V. Chaudhary, M C, S.A. Ansari, R.H. Krishna, A. Kaushik, V. Khanna, Z. Zhao, H. Furukawa, A. Khosla, Low-trace monitoring of airborne sulphur dioxide employing SnO2-CNT hybrids-based energy-efficient chemiresistor, J. Mater. Res. Technol. (2022), https://doi.org/10.1016/j.jmrt.2022.07.159.

[36] Y.C. Wong, B.C. Ang, A.S.M.A. Haseeb, A.A. Baharuddin, Y.H. Wong, Review—conducting polymers as chemiresistive gas sensing materials: a review, J. Electrochem. Soc. 167 (2020), https://doi.org/10.1149/2.0032003jes.

[37] Y. Tang, Y. Xu, J. Yang, Y. Song, F. Yin, W. Yuan, Stretchable and wearable conductometric VOC sensors based on microstructured MXene/polyurethane core-sheath fibers, Sens. Actuators B Chem. 346 (2021), 130500, https://doi.org/10.1016/j.snb.2021.130500.

[38] L. Zhao, Y. Zheng, K. Wang, C. Lv, W. Wei, L. Wang, W. Han, Highly stable cross-linked cationic polyacrylamide/Ti 3C 2 T x MXene nanocomposites for flexible ammonia-recognition devices, Adv. Mater. Technol. 5 (2020) 2000248, https://doi.org/10.1002/admt.202000248.

[39] C. Wu, X. Zhang, R. Wang, L.J. Chen, M. Nie, Z. Zhang, X. Huang, L. Han, Low-dimensional material based wearable sensors, Nanotechnology 33 (2022), 072001, https://doi.org/10.1088/1361-6528/ac33d1.

[40] L. Wang, M. Zhang, B. Yang, J. Tan, X. Ding, W. Li, Recent advances in multidimensional (1D, 2D, and 3D) composite sensors derived from mxene: synthesis, structure, application, and perspective, Small Methods 5 (2021) 2100409, https://doi.org/10.1002/smtd.202100409.

[41] T. Zhou, T. Zhang, Recent progress of nanostructured sensing materials from 0D to 3D: overview of structure–property-application relationship for gas sensors, Small Methods 5 (2021) 2100515, https://doi.org/10.1002/smtd.202100515.

[42] S. Kumar, V. Pavelyev, P. Mishra, N. Tripathi, P. Sharma, F. Calle, A review on 2D transition metal di-chalcogenides and metal oxide nanostructures based NO2 gas sensors, Mater. Sci. Semicond. Process. 107 (2020), 104865, https://doi.org/10.1016/j.mssp.2019.104865.

[43] S. Yang, C. Jiang, S. Wei, Gas sensing in 2D materials, Appl. Phys. Rev. 4 (2017), 021304, https://doi.org/10.1063/1.4983310.

[44] W.Y. Chen, X. Jiang, S.-N. Lai, L. Peroulis, L. Stanciu, Nanohybrids of a MXene and transition metal dichalcogenide for selective detection of volatile organic compounds, Nat. Commun. 11 (2020) 1302, https://doi.org/10.1038/s41467-020-15092-4.

[45] C. Anichini, W. Czepa, D. Pakulski, A. Aliprandi, A. Ciesielski, P. Samorì, Chemical sensing with 2D materials, Chem. Soc. Rev. 47 (2018) 4860–4908, https://doi.org/10.1039/C8CS00417J.

[46] Y. Sheth, S. Dharaskar, V. Chaudhary, M. Khalid, R. Walvekar, Prospects of titanium carbide-based MXene in heavy metal ion and radionuclide adsorption for wastewater remediation: a review, Chemosphere 293 (2022), 133563, https://doi.org/10.1016/j.chemosphere.2022.133563.

[47] V. Chaudhary, A. Sharma, P. Bhadola, A. Kaushik, Adv. MXenes (2022) 301–324, https://doi.org/10.1007/978-3-031-05006-0_12.

[48] V. Chaudhary, A. Sharma, P. Bhadola, A. Kaushik, Adv. MXenes (2022) 301–324, https://doi.org/10.1007/978-3-031-05006-0_12.

[49] H.-J. Koh, S.J. Kim, K. Maleski, S.-Y. Cho, Y.-J. Kim, C.W. Ahn, Y. Gogotsi, H.-T. Jung, Enhanced selectivity of MXene gas sensors through metal ion

intercalation: in Situ X-ray diffraction study, ACS Sens. 4 (2019) 1365–1372, https://doi.org/10.1021/acssensors.9b00310.

[50] Y. Wei, P. Zhang, R.A. Soomro, Q. Zhu, B. Xu, Advances in the synthesis of 2D MXenes, Adv. Mater. 33 (2021) 2103148, https://doi.org/10.1002/adma.202103148.

[51] J. Qiu, X. Xia, Z. Hu, S. Zhou, Y. Wang, Y. Wang, R. Zhang, J. Li, Y. Zhou, Molecular ammonia sensing of PEDOT:PSS/nitrogen doped MXene Ti3C2T xcomposite film at room temperature, Nanotechnology 33 (2022), 065501, https://doi.org/10.1088/1361-6528/ac33d3.

[52] Y. Qin, H. Gui, Y. Bai, S. Liu, Enhanced NH3 sensing performance at ppb level derived from Ti3C2T -supported ZnTi-LDHs nanocomposite with similar metal-semiconductor heterostructure, Sens. Actuators B Chem. 352 (2022), 131077, https://doi.org/10.1016/j.snb.2021.131077.

[53] J. Wu, Y. Yu, G. Su, Safety assessment of 2D MXenes: in vitro and in vivo, Nanomaterials 12 (2022) 828, https://doi.org/10.3390/nano12050828.

[54] A. Khosla, Sonu, H.T.A. Awan, K. Singh, Gaurav, R. Walvekar, Z. Zhao, A. Kaushik, M. Khalid, V. Chaudhary, Emergence of MXene and MXene–polymer hybrid membranes as future- environmental remediation strategies, Adv. Sci. (2022) 2203527, https://doi.org/10.1002/advs.202203527.

[55] J. Tang, X. Huang, T. Qiu, X. Peng, T. Wu, L. Wang, B. Luo, L. Wang, Interlayer space engineering of MXenes for electrochemical energy storage applications, Chem. A Eur. J. 27 (2021) 1921–1940, https://doi.org/10.1002/chem.202002283.

[56] M. Khazaei, M. Arai, T. Sasaki, C.-Y. Chung, N.S. Venkataramanan, M. Estili, Y. Sakka, Y. Kawazoe, Novel electronic and magnetic properties of two-dimensional transition metal carbides and nitrides, Adv. Funct. Mater. 23 (2013) 2185–2192, https://doi.org/10.1002/adfm.201202502.

[57] M. Naguib, M. Kurtoglu, V. Presser, J. Lu, J. Niu, M. Heon, L. Hultman, Y. Gogotsi, M.W. Barsoum, Two-dimensional nanocrystals produced by exfoliation of Ti3AlC2, Adv. Mater. 23 (2011) 4248–4253, https://doi.org/10.1002/adma.201102306.

[58] M. Naguib, M.W. Barsoum, Y. Gogotsi, Ten years of progress in the synthesis and development of MXenes, Adv. Mater. 33 (2021) 2103393, https://doi.org/10.1002/adma.202103393.

[59] L. Wang, H. Zhang, B. Wang, C. Shen, C. Zhang, Q. Hu, A. Zhou, B. Liu, Synthesis and electrochemical performance of Ti3C2Tx with hydrothermal process, Electron. Mater. Lett. 12 (2016) 702–710, https://doi.org/10.1007/s13391-016-6088-z.

[60] R. Meshkian, M. Dahlqvist, J. Lu, B. Wickman, J. Halim, J. Thörnberg, Q. Tao, S. Li, S. Intikhab, J. Snyder, M.W. Barsoum, M. Yildizhan, J. Palisaitis, L. Hultman, P.O.Å. Persson, J. Rosen, W-based atomic laminates and their 2D derivative W 1.33C MXene with vacancy ordering, Adv. Mater. 30 (2018) 1706409, https://doi.org/10.1002/adma.201706409.

[61] J. Zhou, X. Zha, F.Y. Chen, Q. Ye, P. Eklund, S. Du, Q. Huang, A. Two-Dimensional, Zirconium carbide by selective etching of Al 3C 3 from nanolaminated Zr 3 Al 3C 5, Angew. Chem. Int. Ed. 55 (2016) 5008–5013, https://doi.org/10.1002/anie.201510432.

[62] J. Rosen, M. Dahlqvist, Q. Tao, L. Hultman, In- and out-of-plane ordered MAX phases and their MXene derivatives. 2D Met. Carbides Nitrides, Springer International Publishing,, Cham, 2019, pp. 37–52, https://doi.org/10.1007/978-3-030-19026-2_3.

[63] M. Dahlqvist, J. Lu, R. Meshkian, Q. Tao, L. Hultman, J. Rosen, Prediction and synthesis of a family of atomic laminate phases with Kagomé-like and in-plane chemical ordering, Sci. Adv. 3 (2017), https://doi.org/10.1126/sciadv.1700642.

[64] Z. Chen, H. Chong, S. Sun, J. Yang, G. Yao, Q. Wang, J. Zhu, S. Yang, W. Cui, Synthesis and characterizations of solid-solution i-MAX phase (W1/3Mo1/3R1/3) 2AlC (R = Gd, Tb, Dy, Ho, Er and Y) and derived i-MXene with improved electrochemical properties, Scr. Mater. 213 (2022), 114596, https://doi.org/10.1016/j.scriptamat.2022.114596.

[65] K. Maleski, M. Alhabeb, Top-Down MXene synthesis (selective etching). 2D Met. Carbides Nitrides, Springer International Publishing, Cham, 2019, pp. 69–87, https://doi.org/10.1007/978-3-030-19026-2_5.

[66] X.-H. Zha, J. Zhou, P. Eklund, X. Bai, S. Du, Q. Huang, Non-MAX Phase Precursors for MXenes. 2D Met. Carbides Nitrides, Springer International Publishing, Cham, 2019, pp. 53–68, https://doi.org/10.1007/978-3-030-19026-2_4.

[67] B. Ahmed, A. El Ghazaly, J. Rosen, i -MXenes for energy storage and catalysis, Adv. Funct. Mater. 30 (2020) 2000894, https://doi.org/10.1002/adfm.202000894.

[68] M. Alhabeb, K. Maleski, B. Anasori, P. Lelyukh, L. Clark, S. Sin, Y. Gogotsi, Guidelines for synthesis and processing of two-dimensional titanium carbide (Ti 3C 2 T x MXene), Chem. Mater. 29 (2017) 7633–7644, https://doi.org/10.1021/acs.chemmater.7b02847.

[69] Y. Gogotsi, Chemical vapour deposition: transition metal carbides go 2D, Nat. Mater. 14 (2015) 1079–1080, https://doi.org/10.1038/nmat4386.

[70] X. Sang, Y. Xie, D.E. Yilmaz, R. Lotfi, M. Alhabeb, A. Ostadhossein, B. Anasori, W. Sun, X. Li, K. Xiao, P.R.C. Kent, A.C.T. van Duin, Y. Gogotsi, R.R. Unocic, In situ atomistic insight into the growth mechanisms of single layer 2D transition metal carbides, Nat. Commun. 9 (2018) 2266, https://doi.org/10.1038/s41467-018-04610-0.

[71] X. Su, J. Zhang, H. Mu, J. Zhao, Z. Wang, Z. Zhao, C. Han, Z. Ye, Effects of etching temperature and ball milling on the preparation and capacitance of Ti3C2 MXene, J. Alloy. Compd. 752 (2018) 32–39, https://doi.org/10.1016/j.jallcom.2018.04.152.

[72] Y. Shang, Y. Ji, J. Dong, G. Yang, X. Zhang, F. Su, Y. Feng, C. Liu, Sandwiched cellulose nanofiber /boron nitride nanosheet /Ti3C2Tx MXene composite film with high electromagnetic shielding and thermal conductivity yet insulation

performance, Compos. Sci. Technol. 214 (2021), 108974, https://doi.org/10.1016/j.compscitech.2021.108974.

[73] M. Alhabeb, K. Maleski, B. Anasori, P. Lelyukh, L. Clark, S. Sin, Y. Gogotsi, Guidelines for synthesis and processing of two-dimensional titanium carbide (Ti 3C 2 T x MXene), Chem. Mater. 29 (2017) 7633–7644, https://doi.org/10.1021/acs.chemmater.7b02847.

[74] M.R. Lukatskaya, O. Mashtalir, C.E. Ren, Y. Dall'Agnese, P. Rozier, P.L. Taberna, M. Naguib, P. Simon, M.W. Barsoum, Y. Gogotsi, Cation intercalation and high volumetric capacitance of two-dimensional titanium carbide, Science 341 (2013) 1502–1505, https://doi.org/10.1126/science.1241488.

[75] M. Ghidiu, M. Naguib, C. Shi, O. Mashtalir, L.M. Pan, B. Zhang, J. Yang, Y. Gogotsi, S.J.L. Billinge, M.W. Barsoum, Synthesis and characterization of two-dimensional Nb 4C 3 (MXene), Chem. Commun. 50 (2014) 9517–9520, https://doi.org/10.1039/C4CC03366C.

[76] M. Naguib, R.R. Unocic, B.L. Armstrong, J. Nanda, Large-scale delamination of multi-layers transition metal carbides and carbonitrides "MXenes", Dalton Trans. 44 (2015) 9353–9358, https://doi.org/10.1039/C5DT01247C.

[77] T. Li, L. Yao, Q. Liu, J. Gu, R. Luo, J. Li, X. Yan, W. Wang, P. Liu, B. Chen, W. Zhang, W. Abbas, R. Naz, D. Zhang, Fluorine-free synthesis of high-purity Ti 3C 2 T x (T=OH, O) via alkali treatment, Angew. Chem. Int. Ed. 57 (2018) 6115–6119, https://doi.org/10.1002/anie.201800887.

[78] Y. Li, H. Shao, Z. Lin, J. Lu, L. Liu, B. Duployer, P.O.Å. Persson, P. Eklund, L. Hultman, M. Li, K. Chen, X.-H. Zha, S. Du, P. Rozier, Z. Chai, E. Raymundo-Piñero, P.-L. Taberna, P. Simon, Q. Huang, A general Lewis acidic etching route for preparing MXenes with enhanced electrochemical performance in non-aqueous electrolyte, Nat. Mater. 19 (2020) 894–899, https://doi.org/10.1038/s41563-020-0657-0.

[79] L. Yao, Q. Gu, X. Yu, Three-dimensional MOFs@MXene aerogel composite derived MXene threaded hollow carbon confined CoS nanoparticles toward advanced alkali-ion batteries, ACS Nano 15 (2021) 3228–3240, https://doi.org/10.1021/acsnano.0c09898.

[80] A. Numan, S. Rafique, M. Khalid, H.A. Zaharin, A. Radwan, N.A. Mokri, O. P. Ching, R. Walvekar, Microwave-assisted rapid MAX phase etching and delamination: a paradigm shift in MXene synthesis, Mater. Chem. Phys. 288 (2022), 126429, https://doi.org/10.1016/j.matchemphys.2022.126429.

[81] S. Mehdi Aghaei, A. Aasi, B. Panchapakesan, Experimental and theoretical advances in MXene-based gas sensors, ACS Omega 6 (2021) 2450–2461, https://doi.org/10.1021/acsomega.0c05766.

[82] D.H. Ho, Y.Y. Choi, S.B. Jo, J. Myoung, J.H. Cho, Sensing with MXenes: progress and prospects, Adv. Mater. 33 (2021) 2005846, https://doi.org/10.1002/adma.202005846.

[83] E. Lee, A. VahidMohammadi, B.C. Prorok, Y.S. Yoon, M. Beidaghi, D.-J. Kim, Room Temperature gas sensing of two-dimensional titanium carbide (MXene), ACS Appl. Mater. Interfaces 9 (2017) 37184–37190, https://doi.org/10.1021/acsami.7b11055.

[84] Y. Zhang, Z. Zhou, J. Lan, P. Zhang, Prediction of Ti3C2O2 MXene as an effective capturer of formaldehyde, Appl. Surf. Sci. 469 (2019) 770–774, https://doi.org/10.1016/j.apsusc.2018.11.018.

[85] S.J. Kim, H.-J. Koh, C.E. Ren, O. Kwon, K. Maleski, S.-Y. Cho, B. Anasori, C.-K. Kim, Y.-K. Choi, J. Kim, Y. Gogotsi, H.-T. Jung, Metallic Ti 3C 2 T x MXene gas sensors with ultrahigh signal-to-noise ratio, ACS Nano 12 (2018) 986–993, https://doi.org/10.1021/acsnano.7b07460.

[86] C.E. Shuck, M. Han, K. Maleski, K. Hantanasirisakul, S.J. Kim, J. Choi, W.E. B. Reil, Y. Gogotsi, Effect of Ti 3 AlC 2 MAX phase on structure and properties of resultant Ti 3C 2 T x MXene, ACS Appl. Nano Mater. 2 (2019) 3368–3376, https://doi.org/10.1021/acsanm.9b00286.

[87] X. Yu, Y. Li, J. Cheng, Z. Liu, Q. Li, W. Li, X. Yang, B. Xiao, Monolayer Ti 2 CO 2: a promising candidate for NH 3 sensor or capturer with high sensitivity and selectivity, ACS Appl. Mater. Interfaces 7 (2015) 13707–13713, https://doi.org/10.1021/acsami.5b03737.

[88] B. Xiao, Y. Li, X. Yu, J. Cheng, MXenes: reusable materials for NH3 sensor or capturer by controlling the charge injection, Sens. Actuators B Chem. 235 (2016) 103–109, https://doi.org/10.1016/j.snb.2016.05.062.

[89] S. Ma, D. Yuan, Z. Jiao, T. Wang, X. Dai, Monolayer Sc 2 CO 2: a promising candidate as a SO 2 gas sensor or capturer, J. Phys. Chem. C. 121 (2017) 24077–24084, https://doi.org/10.1021/acs.jpcc.7b07921.

[90] S.R. Naqvi, V. Shukla, N.K. Jena, W. Luo, R. Ahuja, Exploring two-dimensional M2NS2 (M = Ti, V) MXenes based gas sensors for air pollutants, Appl. Mater. Today 19 (2020), 100574, https://doi.org/10.1016/j.apmt.2020.100574.

[91] E. Lee, A. VahidMohammadi, Y.S. Yoon, M. Beidaghi, D.-J. Kim, Two-dimensional vanadium carbide MXene for gas sensors with ultrahigh sensitivity toward nonpolar gases, ACS Sens. 4 (2019) 1603–1611, https://doi.org/10.1021/acssensors.9b00303.

[92] W. Guo, S.G. Surya, V. Babar, F. Ming, S. Sharma, H.N. Alshareef, U. Schwingenschlögl, K.N. Salama, Selective toluene detection with Mo 2 CT x MXene at room temperature, ACS Appl. Mater. Interfaces 12 (2020) 57218–57227, https://doi.org/10.1021/acsami.0c16302.

[93] V. Chaudhary, M. Chavali, Novel methyl-orange assisted core-shell polyaniline-silver nanosheets for highly sensitive ammonia chemiresistors, J. Appl. Polym. Sci. 138 (2021) 51288, https://doi.org/10.1002/app.51288.

[94] J. Zou, J. Wu, Y. Wang, F. Deng, J. Jiang, Y. Zhang, S. Liu, N. Li, H. Zhang, J. Yu, T. Zhai, H.N. Alshareef, Additive-mediated intercalation and surface modification of MXenes, Chem. Soc. Rev. 51 (2022) 2972–2990, https://doi.org/10.1039/D0CS01487G.

[95] B. Wang, A. Zhou, F. Liu, J. Cao, L. Wang, Q. Hu, Carbon dioxide adsorption of two-dimensional carbide MXenes, J. Adv. Ceram. 7 (2018) 237–245, https://doi.org/10.1007/s40145-018-0275-3.

[96] K.D. Fredrickson, B. Anasori, Z.W. Seh, Y. Gogotsi, A. Vojvodic, Effects of applied potential and water intercalation on the surface chemistry of Ti 2C and Mo 2C MXenes, J. Phys. Chem. C 120 (2016) 28432–28440, https://doi.org/10.1021/acs.jpcc.6b09109.

[97] M. Wu, M. He, Q. Hu, Q. Wu, G. Sun, L. Xie, Z. Zhang, Z. Zhu, A. Zhou, Ti 3C 2 MXene-based sensors with high selectivity for NH 3 detection at room temperature, ACS Sens. 4 (2019) 2763–2770, https://doi.org/10.1021/acssensors.9b01308.

[98] Z. Ling, C.E. Ren, M.-Q. Zhao, J. Yang, J.M. Giammarco, J. Qiu, M.W. Barsoum, Y. Gogotsi, Flexible and conductive MXene films and nanocomposites with high capacitance, Proc. Natl. Acad. Sci. 111 (2014) 16676–16681, https://doi.org/10.1073/pnas.1414215111.

[99] Z. Yang, A. Liu, C. Wang, F. Liu, J. He, S. Li, J. Wang, R. You, X. Yan, P. Sun, Y. Duan, G. Lu, Improvement of gas and humidity sensing properties of organ-like mxene by alkaline treatment, ACS Sens. 4 (2019) 1261–1269, https://doi.org/10.1021/acssensors.9b00127.

[100] Y. Li, Y. Deng, J. Zhang, Y. Han, W. Zhang, X. Yang, X. Zhang, W. Jiang, Tunable energy storage capacity of two-dimensional Ti 3C 2 T x modified by a facile two-step pillaring strategy for high performance supercapacitor electrodes, Nanoscale 11 (2019) 21981–21989, https://doi.org/10.1039/C9NR07259D.

[101] J. Come, J.M. Black, M.R. Lukatskaya, M. Naguib, M. Beidaghi, A.J. Rondinone, S. V. Kalinin, D.J. Wesolowski, Y. Gogotsi, N. Balke, Controlling the actuation properties of MXene paper electrodes upon cation intercalation, Nano Energy 17 (2015) 27–35, https://doi.org/10.1016/j.nanoen.2015.07.028.

[102] Y. Deng, T. Shang, Z. Wu, Y. Tao, C. Luo, J. Liang, D. Han, R. Lyu, C. Qi, W. Lv, F. Kang, Q. Yang, Fast gelation of Ti 3C 2 T x MXene initiated by metal ions, Adv. Mater. 31 (2019) 1902432, https://doi.org/10.1002/adma.201902432.

[103] M. Guo, C. Liu, Z. Zhang, J. Zhou, Y. Tang, S. Luo, Flexible Ti 3C 2 T x @Al electrodes with ultrahigh areal capacitance: in situ regulation of interlayer conductivity and spacing, Adv. Funct. Mater. 28 (2018) 1803196, https://doi.org/10.1002/adfm.201803196.

[104] M. Ghidiu, S. Kota, J. Halim, A.W. Sherwood, N. Nedfors, J. Rosen, V. N. Mochalin, M.W. Barsoum, Alkylammonium cation intercalation into Ti 3C 2 (MXene): effects on properties and ion-exchange capacity estimation, Chem. Mater. 29 (2017) 1099–1106, https://doi.org/10.1021/acs.chemmater.6b04234.

[105] H. Wang, J. Zhang, Y. Wu, H. Huang, G. Li, X. Zhang, Z. Wang, Surface modified MXene Ti3C2 multilayers by aryl diazonium salts leading to large-scale delamination, Appl. Surf. Sci. 384 (2016) 287–293, https://doi.org/10.1016/j.apsusc.2016.05.060.

[106] A. VahidMohammadi, M. Mojtabavi, N.M. Caffrey, M. Wanunu, M. Beidaghi, Assembling 2D MXenes into highly stable pseudocapacitive electrodes with high power and energy densities, Adv. Mater. 31 (2019) 1806931, https://doi.org/10.1002/adma.201806931.

[107] Z. Yang, A. Liu, C. Wang, F. Liu, J. He, S. Li, J. Wang, R. You, X. Yan, P. Sun, Y. Duan, G. Lu, Improvement of gas and humidity sensing properties of organ-like MXene by alkaline treatment, ACS Sens. 4 (2019) 1261–1269, https://doi.org/10.1021/acssensors.9b00127.

[108] O. Mashtalir, M.R. Lukatskaya, M.-Q. Zhao, M.W. Barsoum, Y. Gogotsi, Amine-assisted delamination of Nb 2C MXene for Li-Ion energy storage devices, Adv. Mater. 27 (2015) 3501–3506, https://doi.org/10.1002/adma.201500604.

[109] Z. Li, X. Wang, W. Zhang, S. Yang, Two-dimensional Ti3C2@CTAB-Se (MXene) composite cathode material for high-performance rechargeable aluminum batteries, Chem. Eng. J. 398 (2020) 125679, https://doi.org/10.1016/j.cej.2020.125679.

[110] S. Zheng, C. Zhang, F. Zhou, Y. Dong, X. Shi, V. Nicolosi, Z.S. Wu, X. Bao, Ionic liquid pre-intercalated MXene films for ionogel-based flexible micro-supercapacitors with high volumetric energy density, J. Mater. Chem. A 7 (2019) 9478–9485, https://doi.org/10.1039/c9ta02190f.

[111] J. Xu, T. Peng, X. Qin, Q. Zhang, T. Liu, W. Dai, B. Chen, H. Yu, S. Shi, Recent advances in 2D MXenes: preparation, intercalation and applications in flexible devices, J. Mater. Chem. A. 9 (2021) 14147–14171, https://doi.org/10.1039/D1TA03070A.

[112] O. Mashtalir, M. Naguib, V.N. Mochalin, Y. Dall'Agnese, M. Heon, M.W. Barsoum, Y. Gogotsi, Intercalation and delamination of layered carbides and carbonitrides, Nat. Commun. 4 (2013) 1716, https://doi.org/10.1038/ncomms2664.

[113] X. Huang, P. Wu, A facile, high-yield, and freeze-thaw-assisted approach to fabricate MXene with plentiful wrinkles and its application in on-chip micro-supercapacitors, Adv. Funct. Mater. 30 (2020) 1910048, https://doi.org/10.1002/adfm.201910048.

[114] S. Abdolhosseinzadeh, R. Schneider, A. Verma, J. Heier, F. Nüesch, C.J. Zhang, Turning trash into treasure: additive free mxene sediment inks for screen-printed micro-supercapacitors, Adv. Mater. 32 (2020), e2000716, https://doi.org/10.1002/adma.202000716.

[115] J. Peng, X. Chen, W.J. Ong, X. Zhao, N. Li, Surface and heterointerface engineering of 2D MXenes and their nanocomposites: insights into electro- and photocatalysis, Chem 5 (2019) 18–50, https://doi.org/10.1016/j.chempr.2018.08.037.

[116] M. Naguib, M. Kurtoglu, V. Presser, J. Lu, J. Niu, M. Heon, L. Hultman, Y. Gogotsi, M.W. Barsoum, Two-dimensional nanocrystals produced by exfoliation of Ti3AlC2, Adv. Mater. 23 (2011) 4248–4253, https://doi.org/10.1002/adma.201102306.

[117] M. Li, J. Lu, K. Luo, Y. Li, K. Chang, K. Chen, J. Zhou, J. Rosen, L. Hultman, P. Eklund, P.O.Å. Persson, S. Du, Z. Chai, Z. Huang, Q. Huang, Element replacement approach by reaction with lewis acidic molten salts to synthesize nanolaminated MAX phases and MXenes, J. Am. Chem. Soc. 141 (2019) 4730–4737, https://doi.org/10.1021/jacs.9b00574.

[118] S. Kajiyama, L. Szabova, H. Iinuma, A. Sugahara, K. Gotoh, K. Sodeyama, Y. Tateyama, M. Okubo, A. Yamada, Enhanced Li-Ion accessibility in MXene titanium carbide by steric chloride termination, Adv. Energy Mater. 7 (2017) 1601873, https://doi.org/10.1002/aenm.201601873.

[119] O. Mashtalir, M.R. Lukatskaya, A.I. Kolesnikov, E. Raymundo-Piñero, M. Naguib, M.W. Barsoum, Y. Gogotsi, The effect of hydrazine intercalation on the structure and capacitance of 2D titanium carbide (MXene), Nanoscale 8 (2016) 9128–9133, https://doi.org/10.1039/C6NR01462C.

[120] Y. Jiang, T. Sun, X. Xie, W. Jiang, J. Li, B. Tian, C. Su, Oxygen-functionalized ultrathin Ti 3C 2 T x MXene for enhanced electrocatalytic hydrogen evolution, ChemSusChem 12 (2019) 1368–1373, https://doi.org/10.1002/cssc.201803032.

[121] H. Wang, Y. Wu, J. Zhang, G. Li, H. Huang, X. Zhang, Q. Jiang, Enhancement of the electrical properties of MXene Ti3C2 nanosheets by post-treatments of alkalization and calcination, Mater. Lett. 160 (2015) 537–540, https://doi.org/10.1016/j.matlet.2015.08.046.

[122] J. Luo, J. Zheng, J. Nai, C. Jin, H. Yuan, O. Sheng, Y. Liu, R. Fang, W. Zhang, H. Huang, Y. Gan, Y. Xia, C. Liang, J. Zhang, W. Li, X. Tao, Atomic sulfur covalently engineered interlayers of Ti 3C 2 MXene for ultra-fast sodium-ion storage by enhanced pseudocapacitance, Adv. Funct. Mater. 29 (2019) 1808107, https://doi.org/10.1002/adfm.201808107.

[123] J. Li, D. Yan, S. Hou, Y. Li, T. Lu, Y. Yao, L. Pan, Improved sodium-ion storage performance of Ti 3C 2 T x MXenes by sulfur doping, J. Mater. Chem. A 6 (2018) 1234–1243, https://doi.org/10.1039/C7TA08261D.

[124] S.N. Shuvo, A.M. Ulloa Gomez, A. Mishra, W.Y. Chen, A.M. Dongare, L.A. Stanciu, Sulfur-doped titanium carbide MXenes for room-temperature gas sensing, ACS Sens. 5 (2020) 2915–2924, https://doi.org/10.1021/acssensors.0c01287.

[125] C. Yang, W. Que, X. Yin, Y. Tian, Y. Yang, M. Que, Improved capacitance of nitrogen-doped delaminated two-dimensional titanium carbide by urea-assisted synthesis, Electrochim. Acta 225 (2017) 416–424, https://doi.org/10.1016/j.electacta.2016.12.173.

[126] X. Jiang, A.V. Kuklin, A. Baev, Y. Ge, H. Ågren, H. Zhang, P.N. Prasad, Two-dimensional MXenes: from morphological to optical, electric, and magnetic properties and applications, Phys. Rep. 848 (2020) 1–58, https://doi.org/10.1016/j.physrep.2019.12.006.

[127] S. Wang, B. Liu, Z. Duan, Q. Zhao, Y. Zhang, G. Xie, Y. Jiang, S. Li, H. Tai, PANI nanofibers-supported Nb2CTx nanosheets-enabled selective NH3 detection driven by TENG at room temperature, Sens. Actuators B Chem. 327 (2021), 128923, https://doi.org/10.1016/j.snb.2020.128923.

[128] S. Wang, Y. Jiang, B. Liu, Z. Duan, H. Pan, Z. Yuan, G. Xie, J. Wang, Z. Fang, H. Tai, Ultrathin Nb2CT nanosheets-supported polyaniline nanocomposite: enabling ultrasensitive NH3 detection, Sens. Actuators B Chem. 343 (2021), 130069, https://doi.org/10.1016/j.snb.2021.130069.

[129] Y. Zhang, Y. Jiang, Z. Duan, Q. Huang, Y. Wu, B. Liu, Q. Zhao, S. Wang, Z. Yuan, H. Tai, Highly sensitive and selective NO2 sensor of alkalized V2CT MXene driven by interlayer swelling, Sens. Actuators B Chem. 344 (2021), 130150, https://doi.org/10.1016/j.snb.2021.130150.

[130] Y. Wang, S. Ma, L. Wang, Z. Jiao, A novel highly selective and sensitive NH3 gas sensor based on monolayer Hf2CO2, Appl. Surf. Sci. 492 (2019) 116–124, https://doi.org/10.1016/j.apsusc.2019.06.212.

[131] S. Hajian, P. Khakbaz, M. Moshayedi, D. Maddipatla, B.B. Narakathu, V. S. Turkani, B.J. Bazuin, M. Pourfath, M.Z. Atashbar, Impact of different ratios of fluorine, oxygen, and hydroxyl surface terminations on Ti3C2T<inf>x</inf> MXene as ammonia sensor: a first-principles study. 2018 IEEE Sensors, IEEE, 2018, pp. 1–4, https://doi.org/10.1109/ICSENS.2018.8589699.

[132] R. Khaledialidusti, A.K. Mishra, A. Barnoush, Atomic defects in monolayer ordered double transition metal carbide (Mo 2 TiC 2 T x) MXene and CO 2 adsorption, J. Mater. Chem. C 8 (2020) 4771–4779, https://doi.org/10.1039/C9TC06046D.

[133] Z. Wang, F. Wang, A. Hermawan, J. Zhu, S. Yin, A facile method for preparation of porous nitrogen-doped Ti 3C 2 Tx MXene for highly responsive acetone detection at high temperature, Funct. Mater. Lett. 14 (2021), https://doi.org/10.1142/S1793604721510437.

[134] X.H. Zha, J. Zhou, K. Luo, J. Lang, Q. Huang, X. Zhou, J.S. Francisco, J. He, S. Du, Controllable magnitude and anisotropy of the electrical conductivity of Hf3C2O2 MXene, J. Phys. Condens. Matter 29 (2017) 165701, https://doi.org/10.1088/1361-648X/aa62da.

[135] J. Choi, B. Chacon, H. Park, K. Hantanasirisakul, T. Kim, K. Shevchuk, J. Lee, H. Kang, S.-Y. Cho, J. Kim, Y. Gogotsi, S.J. Kim, H.-T. Jung, N–p-conductor transition of gas sensing behaviors in Mo 2 CT x MXene, ACS Sens. 7 (2022) 2225–2234, https://doi.org/10.1021/acssensors.2c00658.

[136] W.Y. Chen, S.-N. Lai, C.-C. Yen, X. Jiang, D. Peroulis, L.A. Stanciu, Surface functionalization of Ti 3C 2 T x MXene with highly reliable superhydrophobic protection for volatile organic compounds sensing, ACS Nano 14 (2020) 11490–11501, https://doi.org/10.1021/acsnano.0c03896.

[137] S.M. Majhi, A. Ali, Y.E. Greish, H.F. El-Maghraby, N.N. Qamhieh, A. R. Hajamohideen, S.T. Mahmoud, Accordion-like-Ti 3C 2 MXeNe-based gas sensors with sub-ppm level detection of acetone at room temperature, ACS Appl. Electron. Mater. 4 (2022) 4094–4103, https://doi.org/10.1021/acsaelm.2c00717.

[138] R.K. Choudhury, B.R. Bhagat, K.H. Mali, R. Pokar, A. Dashora, Effect of surface functional group over tungsten carbide MXene for efficient NH3 gas sensing using density functional theory, Appl. Surf. Sci. 603 (2022), 154426, https://doi.org/10.1016/j.apsusc.2022.154426.

[139] K. Rathi, N.K. Arkoti, K. Pal, Fabrication of delaminated 2D metal carbide MXenes (Nb 2 CT x) by CTAB-based NO 2 gas sensor with enhanced stability, Adv. Mater. Interfaces 9 (2022) 2200415, https://doi.org/10.1002/admi.202200415.

[140] A.N. Kumar, K. Pal, Amine-functionalized stable Nb 2 CT x MXene toward room temperature ultrasensitive NO 2 gas sensor, Mater. Adv. 3 (2022) 5151–5162, https://doi.org/10.1039/D2MA00301E.

[141] J. Lee, Y.C. Kang, C.M. Koo, S.J. Kim, Ti 3C 2 T x MXene nanolaminates with ionic additives for enhanced gas-sensing performance, ACS Appl. Nano Mater. 5 (2022) 11997–12005, https://doi.org/10.1021/acsanm.2c03141.

[142] V. Chaudhary, One-dimensional variable range charge carrier hopping in polyaniline–tungsten oxide nanocomposite-based hydrazine chemiresistor, Appl. Phys. A 127 (2021) 536, https://doi.org/10.1007/s00339-021-04690-8.

[143] L. Jin, C. Wu, K. Wei, L. He, H. Gao, H. Zhang, K. Zhang, A.M. Asiri, K.A. Alamry, L. Yang, X. Chu, Polymeric Ti3C2T xMXene composites for room temperature ammonia sensing, ACS Appl. Nano Mater. 3 (2020) 12071–12079, https://doi.org/10.1021/acsanm.0c02577.

[144] V. Chaudhary, A. Kaur, Enhanced room temperature sulfur dioxide sensing behaviour of in situ polymerized polyaniline–tungsten oxide nanocomposite possessing honeycomb morphology, RSC Adv. 5 (2015) 73535–73544, https://doi.org/10.1039/C5RA08275G.

[145] E. Lee, D.-J. Kim, Review— recent exploration of two-dimensional MXenes for gas sensing: from a theoretical to an experimental view, J. Electrochem. Soc. 167 (2020), 037515, https://doi.org/10.1149/2.0152003JES.

[146] W. Yuan, K. Yang, H. Peng, F. Li, F. Yin, A flexible VOCs sensor based on a 3D Mxene framework with a high sensing performance, J. Mater. Chem. A. 6 (2018) 18116–18124, https://doi.org/10.1039/C8TA06928J.

[147] H. Riazi, G. Taghizadeh, M. Soroush, MXeNe-based Nanocomposite Sensors, ACS Omega 6 (2021) 11103–11112, https://doi.org/10.1021/acsomega.0c05828.

[148] S.H. Lee, W. Eom, H. Shin, R.B. Ambade, J.H. Bang, H.W. Kim, T.H. Han, Room-temperature, highly durable Ti 3C 2 T x MXene/graphene hybrid fibers for NH 3 gas sensing, ACS Appl. Mater. Interfaces 12 (2020) 10434–10442, https://doi.org/10.1021/acsami.9b21765.

[149] S. Sun, M. Wang, X. Chang, Y. Jiang, D. Zhang, D. Wang, Y. Zhang, Y. Lei, W18O49/Ti3C2Tx Mxene nanocomposites for highly sensitive acetone gas sensor with low detection limit, Sens. Actuators B Chem. 304 (2020), 127274, https://doi.org/10.1016/j.snb.2019.127274.

[150] A. Hermawan, B. Zhang, A. Taufik, Y. Asakura, T. Hasegawa, J. Zhu, P. Shi, S. Yin, CuO nanoparticles/Ti 3C 2 T x MXeNe hybrid nanocomposites for detection of toluene gas, ACS Appl. Nano Mater. 3 (2020) 4755–4766, https://doi.org/10.1021/acsanm.0c00749.

[151] Y. Zhu, Y. Ma, D. Wu, G. Jiang, Preparation and gas sensing properties of ZnO/MXene composite nanomaterials, Sens. Actuators A Phys. 344 (2022), 113740, https://doi.org/10.1016/j.sna.2022.113740.

[152] X. Liu, H. Zhang, Y. Song, T. Shen, J. Sun, Facile solvothermal synthesis of ZnO/Ti3C2Tx MXene nanocomposites for NO2 detection at low working temperature, Sens. Actuators B Chem. 367 (2022), 132025, https://doi.org/10.1016/j.snb.2022.132025.

[153] Z. Wang, F. Wang, A. Hermawan, Y. Asakura, T. Hasegawa, H. Kumagai, H. Kato, M. Kakihana, J. Zhu, S. Yin, SnO-SnO2 modified two-dimensional MXene Ti3C2T for acetone gas sensor working at room temperature, J. Mater. Sci. Technol. 73 (2021) 128–138, https://doi.org/10.1016/j.jmst.2020.07.040.

[154] S.H. Lee, W. Eom, H. Shin, R.B. Ambade, J.H. Bang, H.W. Kim, T.H. Han, Room-temperature, highly durable Ti 3C 2 T x MXene/graphene hybrid fibers For NH 3 gas sensing, ACS Appl. Mater. Interfaces 12 (2020) 10434–10442, https://doi.org/10.1021/acsami.9b21765.

[155] L. Yao, X. Tian, X. Cui, R. Zhao, M. Xiao, B. Wang, X. Xiao, Y. Wang, Two-dimensional Ti3C2Tx MXene/SnO nanocomposites: towards enhanced response and selective ammonia vapor sensor at room temperature, Sens. Actuators B Chem. 358 (2022) 131501, https://doi.org/10.1016/j.snb.2022.131501.

[156] M. Liu, J. Ji, P. Song, M. Liu, Q. Wang, α-Fe2O3 nanocubes/Ti3C2Tx MXene composites for improvement of acetone sensing performance at room temperature, Sens. Actuators B Chem. 349 (2021) 130782, https://doi.org/10.1016/j.snb.2021.130782.

[157] T. He, W. Liu, T. Lv, M. Ma, Z. Liu, A. Vasiliev, X. Li, MXene/SnO2 heterojunction based chemical gas sensors, Sens. Actuators B Chem. 329 (2021), 129275, https://doi.org/10.1016/j.snb.2020.129275.

[158] H. Tai, Z. Duan, Z. He, X. Li, J. Xu, B. Liu, Y. Jiang, Enhanced ammonia response of Ti3C2T nanosheets supported by TiO2 nanoparticles at room temperature, Sens. Actuators B Chem. 298 (2019), 126874, https://doi.org/10.1016/j.snb.2019.126874.

[159] X. Guo, Y. Ding, D. Kuang, Z. Wu, X. Sun, B. Du, C. Liang, Y. Wu, W. Qu, L. Xiong, Y. He, Enhanced ammonia sensing performance based on MXene-Ti3C2Tx multilayer nanoflakes functionalized by tungsten trioxide nanoparticles, J. Colloid Interface Sci. 595 (2021) 6–14, https://doi.org/10.1016/j.jcis.2021.03.115.

[160] S. Gasso, M.K. Sohal, A. Mahajan, MXene modulated SnO2 gas sensor for ultra-responsive room-temperature detection of NO2, Sens. Actuators B Chem. 357 (2022), 131427, https://doi.org/10.1016/j.snb.2022.131427.

[161] Z. Liu, T. He, H. Sun, B. Huang, X. Li, Layered MXene heterostructured with In2O3 nanoparticles for ammonia sensors at room temperature, Sens. Actuators B Chem. 365 (2022) 131918, https://doi.org/10.1016/j.snb.2022.131918.

[162] W.Y. Chen, C.D. Sullivan, S.-N. Lai, C.-C. Yen, X. Jiang, D. Peroulis, L.A. Stanciu, Noble-nanoparticle-decorated Ti 3C 2 T x MXenes for highly sensitive volatile organic compound detection, ACS Omega 7 (2022) 29195–29203, https://doi.org/10.1021/acsomega.2c03272.

[163] S. Liu, M. Wang, G. Liu, N. Wan, C. Ge, S. Hussain, H. Meng, M. Wang, G. Qiao, Enhanced NO2 gas-sensing performance of 2D Ti3C2/TiO2 nanocomposites by in-situ formation of Schottky barrier, Appl. Surf. Sci. 567 (2021), 150747, https://doi.org/10.1016/j.apsusc.2021.150747.

[164] C.-F. Du, X. Zhao, Z. Wang, H. Yu, Q. Ye, Recent advanced on the mxene–organic hybrids: design, synthesis, and their applications, Nanomaterials 11 (2021) 166, https://doi.org/10.3390/nano11010166.

[165] H. Aghamohammadi, N. Amousa, R. Eslami-Farsani, Recent advances in developing the MXene/polymer nanocomposites with multiple properties: a review study, Synth. Met. 273 (2021), 116695, https://doi.org/10.1016/j.synthmet.2020.116695.

[166] A. Kausar, Polymer/MXene nanocomposite–a new age for advanced materials, Polym. Technol. Mater. 60 (2021) 1377–1392, https://doi.org/10.1080/25740881.2021.1906901.

[167] H. Riazi, S.K. Nemani, M.C. Grady, B. Anasori, M. Soroush, Ti3C2MXene-polymer nanocomposites and their applications, J. Mater. Chem. A 9 (2021) 8051–8098, https://doi.org/10.1039/d0ta08023c.

[168] L. Zhao, K. Wang, K. Wei, L. Wang, W. Han, High-performance flexible sensing devices based on polyaniline/MXene nanocomposites, InfoMat 1 (2019) 407–416, https://doi.org/10.1002/inf2.12032.

[169] X. Wang, K. Sun, K. Li, X. Li, Y. Gogotsi, Ti3C2T /PEDOT:PSS hybrid materials for room-temperature methanol sensor, Chin. Chem. Lett. 31 (2020) 1018–1021, https://doi.org/10.1016/j.cclet.2019.11.031.

[170] J. Zhou, S.H. Hosseini Shokouh, L. Komsa, L. Rieppo, L. Cui, Z. Lv, K. Kordas, MXene-polymer hybrid for high-performance gas sensor prepared by microwave-assisted in-situ intercalation, Adv. Mater. Technol. (2022) 2101565, https://doi.org/10.1002/admt.202101565.

[171] Y. Tang, Y. Xu, J. Yang, Y. Song, F. Yin, W. Yuan, Stretchable and wearable conductometric VOC sensors based on microstructured MXene/polyurethane core-sheath fibers, Sens. Actuators B Chem. 346 (2021), 130500, https://doi.org/10.1016/j.snb.2021.130500.

[172] N. Li, Y. Jiang, C. Zhou, Y. Xiao, B. Meng, Z. Wang, D. Huang, C. Xing, Z. Peng, High-performance humidity sensor based on urchin-like composite of ti 3c 2 mxene-derived TiO 2 nanowires, ACS Appl. Mater. Interfaces 11 (2019) 38116–38125, https://doi.org/10.1021/acsami.9b12168.

[173] Y. Zhou, Y. Wang, Y. Wang, X. Li, Humidity-enabled ionic conductive trace carbon dioxide sensing of nitrogen-doped Ti 3C 2 T x MXene/polyethyleneimine composite films decorated with reduced graphene oxide nanosheets, Anal. Chem. 92 (2020) 16033–16042, https://doi.org/10.1021/acs.analchem.0c03664.

[174] Y. Song, Y. Xu, Q. Guo, Z. Hua, F. Yin, W. Yuan, MXene-derived TiO 2 nanoparticles intercalating between RGO nanosheets: an assembly for highly sensitive gas detection, ACS Appl. Mater. Interfaces 13 (2021) 39772–39780, https://doi.org/10.1021/acsami.1c12154.

[175] M. Hou, J. Gao, L. Yang, S. Guo, T. Hu, Y. Li, Room temperature gas sensing under UV light irradiation for Ti3C2Tx MXene derived lamellar TiO2-C/g-C3N4 composites, Appl. Surf. Sci. 535 (2021), 147666, https://doi.org/10.1016/j.apsusc.2020.147666.

[176] D. Zhang, Q. Mi, D. Wang, T. Li, MXene/Co3O4 composite based formaldehyde sensor driven by ZnO/MXene nanowire arrays piezoelectric nanogenerator, Sens. Actuators B Chem. 339 (2021), 129923, https://doi.org/10.1016/j.snb.2021.129923.

[177] M. Liu, Z. Wang, P. Song, Z. Yang, Q. Wang, Flexible MXene/rGO/CuO hybrid aerogels for high performance acetone sensing at room temperature, Sens. Actuators B Chem. 340 (2021), 129946, https://doi.org/10.1016/j.snb.2021.129946.

[178] H. Zhi, X. Zhang, F. Wang, P. Wan, L. Feng, Flexible Ti 3C 2 T x MXene/PANI/bacterial cellulose aerogel for e-skins and gas sensing, ACS Appl. Mater. Interfaces 13 (2021) 45987–45994, https://doi.org/10.1021/acsami.1c12991.

[179] D. Zhang, D. Wu, X. Zong, Z. Yang, Enhanced SO2 gas sensing properties of metal organic frameworks-derived titanium dioxide/reduced graphene oxide nanostructure, J. Mater. Sci. Mater. Electron. 30 (2019) 11070–11078, https://doi.org/10.1007/s10854-019-01449-z.

[180] Y. Zhou, Y. Wang, Y. Wang, H. Yu, R. Zhang, J. Li, Z. Zang, X. Li, MXene Ti 3C 2 T x -derived nitrogen-functionalized heterophase TiO 2 homojunctions for room-temperature trace ammonia gas sensing, ACS Appl. Mater. Interfaces 13 (2021) 56485–56497, https://doi.org/10.1021/acsami.1c17429.

[181] S. Sardana, H. Kaur, B. Arora, D.K. Aswal, A. Mahajan, Self-powered monitoring of ammonia using an MXene/TiO 2 /cellulose nanofiber heterojunction-based sensor driven by an electrospun triboelectric nanogenerator, ACS Sens. 7 (2022) 312–321, https://doi.org/10.1021/acssensors.1c02388.

[182] B. Sun, F. Qin, L. Jiang, J. Gao, Z. Liu, J. Wang, Y. Zhang, J. Fan, K. Kan, K. Shi, Room-temperature gas sensors based on three-dimensional Co3O4/Al2O3@Ti3C2T MXene nanocomposite for highly sensitive NO detection, Sens. Actuators B Chem. 368 (2022), 132206, https://doi.org/10.1016/j.snb.2022.132206.

[183] X. Bu, F. Ma, Q. Wu, H. Wu, Y. Yuan, L. Hu, C. Han, X. Wang, W. Liu, X. Li, Metal-organic frameworks-derived Co3O4/Ti3C2Tx Mxene nanocomposites for high performance ethanol sensing, Sens. Actuators B Chem. 369 (2022), 132232, https://doi.org/10.1016/j.snb.2022.132232.

[184] Y. Wang, Y. Zhou, Y. Wang, Humidity activated ionic-conduction formaldehyde sensing of reduced graphene oxide decorated nitrogen-doped MXene/titanium dioxide composite film, Sens. Actuators B Chem. 323 (2020), 128695, https://doi.org/10.1016/j.snb.2020.128695.

[185] J. Wen, Z. Song, J. Ding, F. Wang, H. Li, J. Xu, C. Zhang, MXene-derived TiO2 nanosheets decorated with Ag nanoparticles for highly sensitive detection of ammonia at room temperature, J. Mater. Sci. Technol. 114 (2022) 233–239, https://doi.org/10.1016/j.jmst.2021.12.005.

[186] X. Tian, L. Yao, X. Cui, R. Zhao, T. Chen, X. Xiao, Y. Wang, A two-dimensional Ti 3C 2 T X MXene@TiO 2 /MoS 2 heterostructure with excellent selectivity for the room temperature detection of ammonia, J. Mater. Chem. A 10 (2022) 5505–5519, https://doi.org/10.1039/D1TA10773A.

[187] F. Ranjbar, S. Hajati, M. Ghaedi, K. Dashtian, H. Naderi, J. Toth, Highly selective MXene/V2O5/CuWO4-based ultra-sensitive room temperature ammonia sensor, J. Hazard. Mater. 416 (2021), 126196, https://doi.org/10.1016/j.jhazmat.2021.126196.

[188] D. Huang, Y. Wang, X. Wang, H. Li, X. Tan, Y. Chen, W. Wang, Q. Cheng, M. Yi, G. Han, G. Liu, Rational in situ construction of Fe-modified MXene-derived MOFs as high-performance acetone sensor, Chem. Eng. J. 444 (2022), 136526, https://doi.org/10.1016/j.cej.2022.136526.

[189] M. Liu, P. Song, D. Liang, Y. Ding, Q. Wang, 3D porous Ti3C2Tx MXene/rGO/SnO2 aerogel for formaldehyde detection at room temperature, J. Alloy. Compd. 925 (2022), 166664, https://doi.org/10.1016/j.jallcom.2022.166664.

[190] S. Zhang, P. Song, Y. Zheng, Y. Ding, Q. Wang, MoO2/MoO3/MXene ternary nanocomposites for high-performance ethanol detection at room temperature, J. Alloy. Compd. 925 (2022), 166663, https://doi.org/10.1016/j.jallcom.2022.166663.

[191] M. Liu, R. Sun, Z. Sima, P. Song, Y. Ding, Q. Wang, Au-decorated In2O3 nanospheres/exfoliated Ti3C2Tx MXene nanosheets for highly sensitive formaldehyde gas sensing at room temperature, Appl. Surf. Sci. 605 (2022), 154839, https://doi.org/10.1016/j.apsusc.2022.154839.

[192] A. Rozmysłowska-Wojciechowska, A. Szuplewska, T. Wojciechowski, S. Poźniak, J. Mitrzak, M. Chudy, W. Ziemkowska, L. Chlubny, A. Olszyna, A.M. Jastrzębska, A simple, low-cost and green method for controlling the cytotoxicity of MXenes, Mater. Sci. Eng. C 111 (2020), 110790, https://doi.org/10.1016/j.msec.2020.110790.

[193] D. Pathania, S. Kumar, P. Thakur, V. Chaudhary, A. Kaushik, R.S. Varma, H. Furukawa, M. Sharma, A. Khosla, Essential oil-mediated biocompatible magnesium nanoparticles with enhanced antibacterial, antifungal, and photocatalytic efficacies, Sci. Rep. 12 (2022) 11431, https://doi.org/10.1038/s41598-022-14984-3.

[194] D. Pathania, M. Sharma, P. Thakur, V. Chaudhary, A. Kaushik, H. Furukawa, A. Khosla, Exploring phytochemical composition, photocatalytic, antibacterial, and antifungal efficacies of Au NPs supported by Cymbopogon flexuosus essential oil, Sci. Rep. 12 (2022) 14249, https://doi.org/10.1038/s41598-022-15899-9.

[195] V. Saasa, T. Malwela, M. Beukes, M. Mokgotho, C.-P. Liu, B. Mwakikunga, Sensing technologies for detection of acetone in human breath for diabetes diagnosis and monitoring, Diagnostics 8 (2018) 12, https://doi.org/10.3390/diagnostics8010012.

[196] X. Li, Z. An, Y. Lu, J. Shan, H. Xing, G. Liu, Z. Shi, Y. He, Q. Chen, R.P.S. Han, D. Wang, J. Jiang, F. Zhang, Q. Liu, Room temperature VOCs sensing with termination-modified Ti 3C 2 T x MXene for wearable exhaled breath monitoring, Adv. Mater. Technol. (2021) 2100872, https://doi.org/10.1002/admt.202100872.

[197] V. Chaudhary, Application of nanomaterials as nano-masks, in: Nanotechnological Appl. Virol., Elsevier, 2022, pp. 57–77, https://doi.org/10.1016/B978-0-323-99596-2.00006-6.

[198] S. Sonu, V. Chaudhary, A paradigm of internet-of-nano-things inspired intelligent plant pathogen-diagnostic biosensors, ECS Sens. (2022), https://doi.org/10.1149/2754-2726/ac92ed.

[199] S. Panda, K. Deshmukh, C. Mustansar Hussain, S.K. Khadheer Pasha, 2D MXenes for combatting COVID-19 Pandemic: a perspective on latest developments and innovations, FlatChem 33 (2022), 100377, https://doi.org/10.1016/j.flatc.2022.100377.

[200] J. Zhu, M. Zhu, Q. Shi, F. Wen, L. Liu, B. Dong, A. Haroun, Y. Yang, P. Vachon, X. Guo, T. He, C. Lee, Progress in <scp>TENG</scp> technology—A journey from energy harvesting to nanoenergy and nanosystem, EcoMat 2 (2020), https://doi.org/10.1002/eom2.12058.

[201] Y. Dong, S.S.K. Mallineni, K. Maleski, H. Behlow, V.N. Mochalin, A.M. Rao, Y. Gogotsi, R. Podila, Metallic MXenes: a new family of materials for flexible triboelectric nanogenerators, Nano Energy 44 (2018) 103–110, https://doi.org/10.1016/j.nanoen.2017.11.044.

[202] K. Hassan, N. Stanley, T.T. Tung, P.L. Yap, H. Rastin, L. Yu, D. Losic, Extrusion-printed CNT–graphene sensor array with embedded MXene/PEDOT:PSS heater for enhanced NO 2 sensing at low temperature, Adv. Mater. Interfaces 8 (2021) 2101175, https://doi.org/10.1002/admi.202101175.

[203] M.H. Abbasi Geravand, E. Saljoughi, S.M. Mousavi, S. Kiani, Biodegradable polycaprolactone/MXene nanocomposite nanofiltration membranes for the treatment of dye solutions, J. Taiwan Inst. Chem. Eng. 128 (2021) 124–139, https://doi.org/10.1016/j.jtice.2021.08.048.

[204] W. Zhang, Z. Pan, J. Ma, L. Wei, Z. Chen, J. Wang, Degradable cross-linked collagen Fiber/MXene composite aerogels as a high-performing sensitive pressure sensor, ACS Sustain. Chem. Eng. 10 (2022) 1408–1418, https://doi.org/10.1021/acssuschemeng.1c05757.

Vishal Chaudhary is assistant professor Physics at University of Delhi, India since 2015. He received Ph.D. in Condensed matter Physics from Department of Physics & Astrophysics, DU, New Delhi, India. He has expertise in engineering the physicochemical attributes of nanosystems through optimizing the reaction parameters for gas/vapor monitoring. He is leader of SUMAN Laboratory (SUstainable Materials and Advanced Nanotechnology Lab), New Delhi, India. He has published > 50 papers on architecting controllable nanosystems for environmental remediation, and received SDG service award (2021). He is currently holding editorial role at ECS Sensor Plus and chaired around 100 international events and conferences.

Hafiz Taimoor Ahmed Awan obtained his Bachelor's degree in Applied Physics from the NED University of Engineering & Technology, Pakistan and a Master's degree in Engineering Science (Applied Physics) from Ghulam Ishaq Khan Institute of Engineering Sciences & Technology, Pakistan. During his Master's studies, he worked on developing and characterizing nanomaterials for hybrid energy storage devices. His research interest lies in implementing 2D materials and their heterostructures for batteries, supercapacitors, and emerging energy storage devices.

Mohammad Khalid is a Professor and Head of Graphene & Advanced 2D Materials Research Group at Sunway University, Malaysia. He completed his degree in Chemical Engineering from Visvesvaraya Technological University, India, M.Sc. in Chemical and Environmental Engineering from Universiti Putra Malaysia, and Ph.D. in Engineering from International Islamic University Malaysia. His research interests include advanced nanomaterial synthesis for energy harvesting, storage, and conversion applications. He has over 250 peer-reviewed scientific articles, six edited books, and five patents. He is also a fellow of the Higher Education Academy (FHEA), UK.

Pradeep Bhadola is lecturer of Physics of Complex Systems and Computational Physics at CENTRE FOR THEORETICAL PHYSICS AND NATURAL PHILOSOPHY, Nakhonsawan Studiorum for Advanced Studies" (NAS) Mahidol University, Thailand. He has obtained his education from University of Delhi, India. His research interests are Complex System and Networks, Density functional theory, Computational Physics and Data Science, Application of Statistical Mechanics and Machine Learning to biology, economics and finance and theoretical condensed matter physics. He has published more than 30 research publications in reputed journals and chaired various international conferences.

Prof. R. P. Tandon received his Ph.D. Degree in Physics in 1977 from University of Delhi, India. He worked at National Physical Laboratory during 1977–1998 and headed its Electroceramic Division for more than a decade. He worked as Research Associate at Massachusetts Institute of Technology (MIT, USA) during 1980–1982. In 1996 he was appointed as Scientific Advisor to the Government of Haryana, a dynamic Indian State. Prof. R. P. Tandon joined the Department of Physics and Astrophysics at the University of Delhi in 1998 as a full professor. Prof. Tandon took the charge as Head of the Department on November 16, 2010 for the 3 years term. He has several international collaborations, and has been visiting scientist to the University of Leeds, UK, University of Quebec, Guelph, University of Toronto and Seoul National University, South Korea etc. He is member of several national and international scientific bodies. He has been a founder member of the Asian Meeting on Ferroelectricity and currently its Board Member from India. His research interest includes ceramics, polymers, solar cells and glasses and has published about 190 research papers in these areas and supervised 25 students for their doctoral degree.

Ajit Khosla is a distinguished professor in the School of Advanced Materials and Nanotechnology at the Xidian University, and fellow of Royal Society of Chemistry, United Kingdom. He is the author of over 180 publications in refereed journals, 4 books and 5 US patents. He is Founding Editor-in-Chief of one of Electrochemical Society's first gold open access journals, ECS Sensors Plus. He is also Technical Editor Electrochemical Society's family of journals. He is chair and founder of ICTSGS and 4DMS+SoRo annual conference series. His research program is interdisciplinary in nature, with a focus on micro-nano-fabricated chemical and biological sensors systems.